TROPICAL CYCLONES IN PALEOCLIMATE SIMULATIONS

A Dissertation

by

RYAN ALEXANDER ZAMORA

Submitted to the Office of Graduate and Professional Studies of
Texas A&M University
in partial fulfillment of the requirements for the degree of

DOCTOR OF PHILOSOPHY

Chair of Committee, Robert L. Korty
Committee Members, Courtney Schumacher
Ramalingam Saravanan
Ping Chang
Head of Department, Ping Yang

December 2016

Major Subject: Atmospheric Sciences

ABSTRACT

This research examines tropical cyclones in simulations of climates very different from modern. The tropical cyclones are simulated via two techniques: explicitly tracking TC-like structures in global climate model output, and by downscaling model output to be used in higher resolution models able to resolve tropical cyclones. These techniques are applied to climates such as the Last Glacial Maximum, mid-Holocene, and in a suite of simulations that feature very hot surface temperatures forced by higher global concentrations of CO_2. The simulated tropical cyclone climatologies are compared with the large-scale environmental factors within these climates, in an effort to extend the knowledge of the tropical cyclone response across varying climate conditions.

Explicitly resolved storms within CCSM4 did not relate well to a common set of environmental factors across 20th century and LGM climates, and in addition showed that changes in climate are potentially sensitive to the inclusion of the weakest systems, which are controlled by the choice of threshold detection criteria. Sensitivity tests conducted on these storms showed that altering the surface wind speed threshold an initial disturbance must achieve by as little as 20% significantly alters the overall result (showing a greater number of 20th century or Last Glacial Maximum storms generated depending on this choice).

We show that the storms generated via Emanuel’s downscaled storms technique relates well in each of the climates to a combination of environmental factors important for TC genesis and development, such as genesis potential and ventilation indices. Regional and temporal changes in these large-scale factors well predict changes in tropical cyclone activity between the different climates. In addition, these storms show relationships in intensity and genesis with warming, particularly with the strongest storms generated.

DEDICATION

I dedicate this dissertation to my pregnant wife, Misti, and our growing baby. We can’t wait to meet you.

ACKNOWLEDGEMENTS

I would like to thank my advisor, Dr. Robert Korty, who has been a great mentor throughout my time spent at Texas A&M. Thank you for all of your guidance and help, and for the knowledge you’ve passed on to me that I will continue to use in my future endeavors. I would also like to thank my committee members, Dr. Courtney Schumacher, Dr. Ramalingam Saravanan, and Dr. Ping Chang. Thank you for your teaching, time, and the support you have given all these years.

I also would like to thank my past officemates, and fellow graduate students who have always made the long workdays more manageable and fun. In addition, I cannot understate the amount of help the Department of Atmospheric Sciences faculty and staff has provided. Thank you for all your hard work.

I would like to extend thanks to my friends and family for all of their prayers, love, support, and making every day full of laughs and happiness. I especially would like to give thank my wife, Misti, for her love and always supporting me throughout all of our years at A&M. Though this chapter is closing, I look forward to all the new memories we’ll make. Lastly, I would like to give thanks to my parents for all of their support and encouragement.

NOMENCLATURE

0k	Preindustrial Era
20C	Twentieth Century
CCSM4	Community Climate System Model (version 4)
CMIP	Climate Model Intercomparison Project
CZ02	Camargo and Zebiak (2002) Vortex Tracking Algorithm
GPI	Genesis Potential Index
LGM	Last Glacial Maximum
MH	Mid-Holocene
MPI	Max Planck Institute for Meteorology Model
MRI	Meteorological Research Institute Model
NCAR	National Center for Atmospheric Research
PI	Potential Intensity
PMIP	Paleoclimate Model Intercomparison Project
RH	Relative Humidity
RSST	Relative Sea Surface Temperature
SST	Sea Surface Temperature

TABLE OF CONTENTS

LIST OF FIGURES

LIST OF TABLES

CHAPTER I

INTRODUCTION

The ways tropical cyclones (TCs) respond and adapt to changes in large-scale climate are significant and potentially consequential questions for the coming century. Assessments of historical TC records show increasing TC intensity, particularly in the frequency of the most intense events (Emanuel 2005; Webster et al. 2005; Elsner and Kossin 2008; Kossin et al. 2013), but persistent questions about the accuracy and completeness of these records undermine confidence in these findings (Landsea et al. 2006, 2010; Klotzbach and Landsea 2015). Moreover, Ting et al. (2015) analyzed a suite of computer simulations that isolate the effects of natural and individual anthropogenic forces and found that potential intensity (e.g., Bister and Emanuel 2002; hereafter *PI*), a theoretical upper limit on TC intensity, has been subject to opposing pressures over the last three decades. While increasing levels of carbon dioxide (CO_2) have the effect of increasing *PI*[1], concurrent increases in sulfate aerosols had the opposite effect, offsetting the increase and rendering any trend detection in actual data difficult. Given these difficulties, model projections of future warming have been a major tool for studying aspects of TCs and climate.

Using global climate models (GCMs) to address TC-climate connections presents a number of challenges. Historically, the spatial resolution of these models has been far too coarse to resolve the intense gradients needed to simulate intensity accurately

---

[1] At least in the range of modern values; Emanuel and Sobel (2013) and some results presented in Chapter VII of this thesis show this behavior does not extend indefinitely.

(Camargo and Wing 2016), and automated algorithms that detect and follow model generated cyclones are sensitive to thresholds chosen to identify them (Horn et al. 2014). Although some GCMs now run at 25-km resolution are able to simulate Category 4 and 5 storms (Murakami et al. 2015), the uppermost tail of the intensity distribution has been truncated in regional models with even higher spatial resolution (Knutson et al. 2010). Downscaling GCM fields to regional or other high resolution models has been useful to study how intensity may change with warming (Knutson et al. 2015; Emanuel et al. 2008; Emanuel 2013), but direct simulation requires extensive computation resources, while the Emanuel method uses an artificial seeding method that may affect its prediction of storm frequency.

GCMs have also been used to study how the environments that spawn and sustain TCs change with climate. Since at least the work of Palmén (1948) and Gray (1968), it has been known that some large-scale environmental conditions must be present for storms to form and survive. These include a relatively high sea surface temperature (*SST*), low atmospheric stability, high column relative humidity, and low vertical wind shear over a deep layer of the troposphere. Additional factors such as high low level vorticity have also been identified and may be important locally, although Tippet et al. (2011) argued that climatologically persistent low vorticity might not aid genesis further. Out of these results, a number of tropical cyclone genesis indices have been developed with the intent of packaging the important factors in a way that can diagnose and predict areas conducive to development (e.g. DeMaria et al. 2001; Emanuel and Nolan 2004; Bye and Keay 2008; Bruyère et al. 2012; Waters et al. 2012;

Holland and Bruyère 2014). The difficulties in using this approach (as a stand-alone method) are determining which factors should be used, the discrete weightings of these factors, and extrapolating their response to climates different than our own (where it is impossible to calibrate against observations).

More fundamentally, while some large-scale conditions appear necessary for genesis (e.g., warm ocean surface), they are nevertheless ubiquitous in tropical latitudes. And it is not immediately obvious that higher values of some genesis factors in an already favorable environment raise the prospects of genesis any further (e.g., Tippet et al. 2011, found that away from the latitudes nearest the equator, higher values of absolute vorticity, primarily a function of latitude, did not correlate with enhanced genesis). Moreover, actual genesis often depends on mesoscale features and conditions not necessarily well captured by large-scale analysis. So there are valid reasons to question the utility of such frameworks. Yet despite these concerns, they have proven useful predictors in many contexts such as relating interannual variability to changes in the large-scale environment associated with ENSO (Camargo et al. 2007).

Analyses of simulations prepared for the 3rd Climate Model Intercomparison Project (CMIP3) showed that while environments may become more favorable for stronger storms by the end of this century, the overall number of storms may decline, largely owing to a reduction in the frequency of weak systems (e.g., Emanuel et al. 2008; Knutson et al. 2010). Newer simulations completed for CMIP (CMIP5) have shown some qualitatively similar behavior, but many of the differences between late 20th and 21st century output had smaller amplitudes and only marginal significances (e.g., Knutson et al. 2013). Recent reviews by Sobel et al. (2016), Walsh et al. (2016), and Camargo and Wing (2016) highlight that there is more confidence in how intensity responds to anthropogenic warming than there is how frequency may change. We lack a theory to predict even the order of magnitude of TCs observed, which limits our ability to understand the divergent results between methods. Thus despite the significant progress over the last decade, there is much still to learn, and complementary research avenues have the potential for novel insights.

One such research avenue is the examination of the response of tropical cyclones in past climates (paleotempestology). This is an appealing approach as it allows the examination of TCs in climates vastly different than contemporary. As the global observational record for TCs is limited to the satellite era, proxies for hurricane landfall in sediment cores supplement the amount of data for research. Previous research (Liu and Fearn 1993, 1998; Donnelly 2005) examined sand layers in sediment records taken along barrier islands and proposed that these layers were transported via strong storm surge. While this technique has been validated against historical storms over the past four centuries (Donnelly 2005), its power comes from its ability to identify storms from centuries and millennia past. New techniques using offshore cores have shown the potential to identify events from the more distant past: the early Holocene and late Pleistocene (i.e., Younger Dryas; Toomey et al. 2016).

To complement the geologic record, numerical studies of TCs in past climate simulations are becoming more common (Yan et al. 2016; Korty et al. 2012a, b, 2016; Yoo et al. 2016).In this thesis, we apply examples of each of the methods outlined above to paleoclimate simulations (1) to learn how each method responds to different (and in many instances larger) forcing than examined to date, and (2) to provide new evidence of how various aspects of TCs change across climates. We focus first on equilibrium simulations of the Last Glacial Maximum 21,000 years ago (21ka), but also consider the effects of variable orbital forcing on mid-Holocene simulations 6,000 years ago (6ka), as well as high carbon dioxide simulations (up to 8960 ppm) that produce surface temperatures last seen during Miocene (~20 million years ago; 20Ma) and Eocene epochs (55Ma).

The majority of results presented here stem from simulations produced with the National Center for Atmospheric Research's (NCAR) Community Climate System Model version 4 (CCSM4) and its predecessors (e.g., Community Atmosphere Model version 3; CAM3). We use this family of models despite their well-known flaws in simulating the *SST* and climate of the tropical Atlantic (e.g., Grodsky et al. 2012) that limit production of TCs in that basin (Camargo 2014). Among the advantages it offers for this study are that it has been widely used in many past climate simulations and it benefits from a dedicated set of researchers and model developers that have tested various subroutines and components under conditions even more extreme than we study here (e.g., the radiation code has been tested past 10,000 ppm CO_2; M. Huber, personal communication, 2016). It also saved output at high temporal frequency from paleoclimate runs prepared for model intercomparison projects, which enables directly tracking features in its 6 hourly data. Where able, we apply the same techniques to other major modeling center's simulations using the same past climate forcing to see what differences arise, but a thorough model intercomparison in any one climate lies beyond the scope of work presented here. Far fewer modeling centers contribute simulations to the Paleoclimate Modeling Intercomparison Projects (PMIP; see Braconnot et al. 2012 for more information) than do for the current century, and most of the fields from them are archived only at monthly intervals.

This thesis begins in Chapter II with a presentation and review of the methods we use to investigate TCs in past climate simulations. GCMs produce features with tropical cyclone-like structures (i.e. warm core, convectively driven), which we track using an algorithm developed to identify their defining characteristics (we use the Camargo and Zebiak 2002 algorithm, henceforth CZ02, although there is a long history of many others: e.g., Hodges 1994, 1995; Vitart and Stockdale 2001; Marchok 2002; Bengtsson et al. 2007; Walsh et al. 2007; Tory et al. 2013). The CZ02 algorithm tracks systems when specific model-dependent thermodynamic and kinematic variables exceed user-chosen thresholds. Connecting nearby points that exceed one of these thresholds identifies model-generated tropical cyclone tracks. Should the track last longer than a specified period of time (in most algorithms, a couple of days), it is defined as a tropical cyclone. We explore the sensitivity of results to the thresholds chosen in later chapters. We also review the statistical downscaling method developed by Emanuel (2006), which we employ in later chapters.

Chapters III, IV, and V present results of TCs from simulations of the Last Glacial Maximum (LGM) that featured tropical surface temperatures colder by 2-3°C than the modern world. Ice sheets covered many Northern Hemisphere continents, and atmospheric concentrations of CO_2 were only 185 ppm. Korty et al. (2012a) showed that despite these changes, many of the large-scale environmental conditions necessary for tropical cyclone genesis today were similarly favorable (and in some regions even more favorable) for genesis in the colder climate. The colder ocean temperatures are bound to a colder atmosphere, and the transfer of heat between the two media can occur as efficiently as in the modern world. The changes in environmental parameters shown by Korty et al. (2012a, b) predict responses in the climatology of tropical cyclones, but comparisons with actual model generated storms or downscaled events has yet to be attempted. This is the goal of the work presented in Chapters III and IV (that looks at explicitly simulated systems in CCSM4's LGM and 20th century runs), as well as the results in Chapter V (that present results from Emanuel's downscaling technique of LGM simulations with CCSM4 and other models).

Variations in Earth's orbit change affect the amount of solar radiation seasonally incident on the top of the atmosphere (TOA). During the mid-Holocene (MH), as much as 30 W/m^2 more radiation was received during the Northern Hemisphere summer months than is received today. Korty et al. (2012b) showed that because the atmosphere warmed in response to this seasonal anomaly faster than the ocean surface, lapse rates were stabilized and *PI* was reduced during the early part of modern Northern Hemisphere hurricane season. In Chapter VI, we examine the response of TCs that form in CCSM4's MH simulation and compare them to these environmental changes. We also present how Emanuel's downscaling technique responds to them.

Finally, we explore TCs in simulations with very hot surface conditions (forced with 8x and 32x preindustrial era levels of CO_2). As discussed in Zamora et al. (2016), these cases feature far more extensive coverage of moist neutral lapse rates: both a seasonal expansion and a spatial one to middle and high latitudes. The spreading of TCs to new territory is presented here (see also Korty et al. 2016). Chapter VIII summarizes the main findings of this thesis.

CHAPTER II

DATA AND METHODS

In this chapter, we review the properties of model data and the methods used to assess aspects of TC climatology in past climate simulations. We begin with a review of the model data and then discuss the Camargo and Zebiak (2002) tracking algorithm used to identify and follow TCs that the GCM explicitly generates. We show examples of the structure of systems that this algorithm picks up, as this is important to bear in mind when interpreting output from the algorithm in the results of Chapter III. We conclude this chapter by reviewing the Emanuel downscaling method that we apply to LGM (Chapter V), mid-Holocene (Chapter VI), and high CO_2 climate (Chapter VII) simulations. Large-scale environmental factors are not reviewed here, but rather when first presented in Chapter IV.

Paleoclimate Model Data: Last Glacial Maximum

Braconnot et al. (2007) describes the paleoclimate experimental design for PMIP2 simulations, and the higher spatial resolution PMIP3 experiments are discussed in Braconnot et al. (2012). Briefly, we review the main characteristics of the LGM and experiments here. Orbital values for eccentricity, obliquity, and precession appropriate to 21ka are used (Berger 1978), although LGM values are very similar to modern ones. CO_2 was reduced to 185 ppm, methane to 350 ppbv (from 760 ppbv in preindustrial era climates), and NO_2 to 200 ppbv (from 270 ppbv in preindustrial era); these decreases combined to reduce radiative forcing of the troposphere by -2.8 W/m^2 at LGM

(Braconnot et al. 2007). The ICE-5G ice sheet reconstruction of Peltier (2004) is used for boundary conditions, which includes a 2-3.5 km ice sheet across modern-day central Canada and ~2 km thick ice on Greenland and in Scandinavia (although Siberia had no permanent, thick glacier). The large ice volume results in lower sea levels by about 120 m, exposing continental shelves and making a significant change in the land-sea mask in the vicinity of the maritime continent near Southeast Asia. All experiments were run to equilibrium, and data from at least the last 100 years of output was archived for later analysis (these data are largely saved at monthly means). In the case of CCSM4 (0.94° x 1.25° latitude-longitude resolution and 17 pressure levels), we use an additional 30-year extension of the PMIP3 experiment that saved output from all components of the coupled model at 6 hourly intervals and obtained the data directly from NCAR.

These changes resulted in several important characteristics of the Last Glacial Maximum. Tropical sea surface temperatures were ~2-3°C cooler than in the preindustrial era (Broccoli 2000, Korty et al. 2012a) and even larger changes occur at higher latitudes (as much as 30°C cooler over Northern Hemisphere ice sheets), due to the significantly lower CO_2 concentrations (185 ppm) and presence of extensive ice sheets. Global mean temperatures were between -3.6°C and -5.7°C cooler at LGM across the models included in PMIP2. Korty et al. (2012a) showed that despite these changes, many of the large-scale environmental conditions necessary for tropical cyclone genesis today were similarly favorable (and in some regions even more favorable) for genesis in the colder climate. The colder ocean temperatures are bound to a colder atmosphere, and the transfer of heat between the two media can occur as efficiently as in the modern world, and regional changes in vertical wind shear can alter favorability locally.

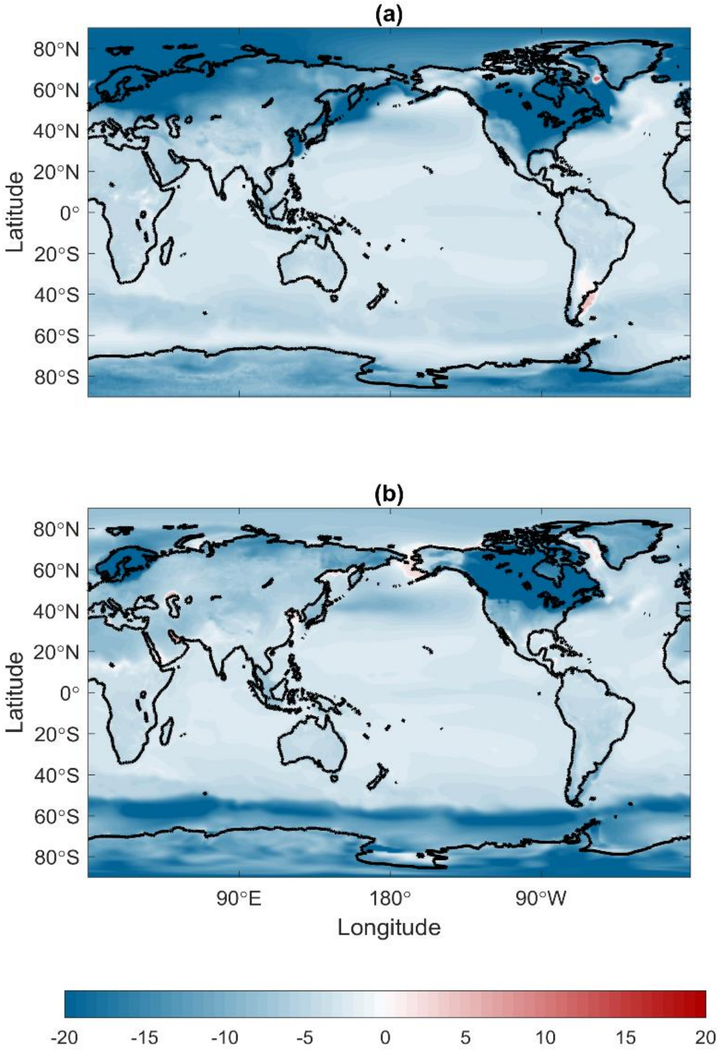

Figure 1 CCSM4 climatologically averaged surface temperature difference between Last Glacial Maximum and 20th century experiments during (a) January and (b) July.

Figure 1 shows difference in surface temperature between CCSM4's Last Glacial Maximum and 20th century climate simulations in January and July. These plots show the 2-3°C drop in LGM temperatures relative to our current climate, and a much larger disparity at higher latitudes (particularly in the extension of the Northern Hemisphere ice sheet over the continental United States. and Europe). Note that the color range in **Figure 1** truncates at -20°C, while departures of continental temperatures at high latitudes are much larger (as large as -55°C in January and -36°C in July). Comparing the seasonal extremes, we see a shift in the largest temperature differences that follow the hemisphere experiencing winter.

We use the 6 hourly data from CCSM4 for vortex tracking, and use it along with the Max Planck Institute for Meteorology Model (MPI) and Meteorological Research Institute Model (MRI) for the Emanuel downscaling method presented in Chapter V. The MPI model was described by Stevens et al., (2013) and Giorgetta et al. (2013), and the current version of MRI is described in Yukimoto, et al. (2012), although additional details describing earlier versions are described in Kurihara et al. (2005), Kitoh (2004), and Yukimoto et al. (2006). Both of these models feature slightly coarser horizontal resolutions than used in CCSM4, and include 26 years of data available for the 20th century control (1980-2005), and 30 years available for each paleoclimate experiment. The MPI model has a 1.86° x 1.88° latitude-longitude horizontal resolution, and includes 25 vertical pressure levels. MRI has a 1.12° x 1.13° horizontal resolution and includes 23 vertical pressure levels.

Paleoclimate Model Data: Mid-Holocene

The major difference between the mid-Holocene and preindustrial era is the orbital configuration that lead to a more than 25 W/m^2 increase in the seasonal cycle of Northern Hemisphere incoming solar radiation and a decrease in the Southern Hemisphere cycle (Berger 1978; Braconnot et al. 2007). Earth made its closest approach to the Sun during mid-September 6ka (it is in early January in modern times). This leads to an increase in top-of-the-atmosphere (TOA) radiation during the Northern Hemisphere TC season, and a decrease during the Southern Hemisphere season.

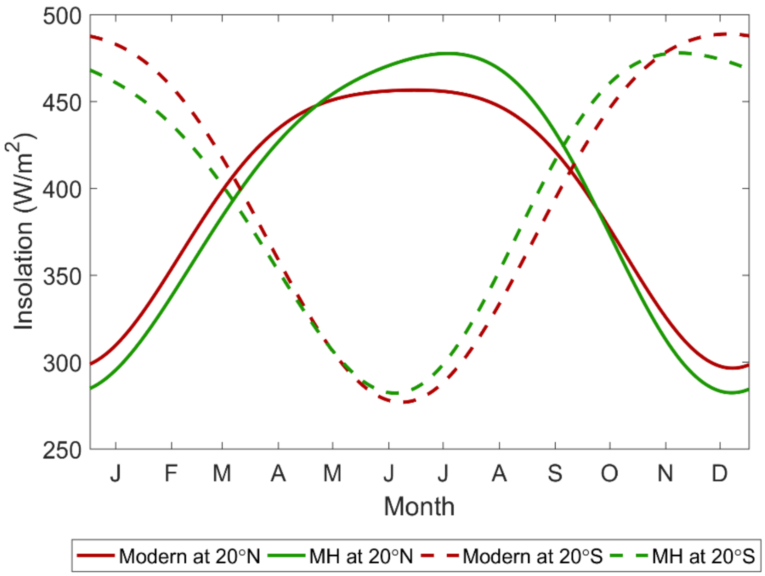

Figure 2 Insolation cycle at 20° latitude during modern (red) and mid-Holocene (green).

Figure 2 shows the annual change in the amount of TOA solar radiation received at 20°S and 20°N for modern and mid-Holocene CCSM4 simulations. The plot shows the relative shift in mid-Holocene insolation received towards later in the tropical cyclone season along the 20°N band, and earlier in the tropical cyclone season at 20°S. In addition to the seasonal shift in TOA solar radiation, the mid-Holocene featured a larger range of values at 20°N and a smaller range of values at 20°S relative to the 20th century.

In addition to the models examined using Emanuel's downscaled storms technique in LGM simulations (CCSM4, MPI, and MRI), for the mid-Holocene we also use the Hadley Global Environment Model 2 (HadGEM2), which does not currently have output for a 6-hourly LGM experiment. HadGEM2 (Bellouin et al. 2007; Collins et al. 2011; Martin et al. 2011) has 26 years of available data for 20th century simulations (1980-2005) and 17 years available for the mid-Holocene. HadGEM2 has a 1.25° x 1.88° latitude-longitude horizontal resolution at 23 pressure levels.

Control Climate Model Data: 20th Century

Although the preindustrial era is usually taken to be the control climate for LGM and mid-Holocene experiments, we use the corresponding CMIP5 member from the late 20th century historical run (1980-2005) to compare against. We do this primarily because there are no global observations of TCs from the preindustrial era, so comparing any model simulation with observations is only possible with 20th century runs. Additionally, unlike earlier generations of PMIP, PMIP3 used the same model versions, routines and resolutions as the CMIP5 control cases (Taylor et al. 2012), which removes several barriers to comparing them. Although the preindustrial era cases would facilitate some direct comparisons (CO_2 at mid-Holocene is the same as preindustrial era, while it is 80-

90 ppm higher in the late 20th century), we choose to sacrifice this in order to compare the 20th century climatology of TCs with observations.

Hot Climate Model Data: High CO_2 Experiments

We also examined how the Emanuel downscaling technique responds to climate changes resulting from very large increases in carbon dioxide. We downscale three simulations of NCAR's Community Atmospheric Model version 3 (CAM3) at T42 horizontal resolution (~2.5° latitude-longitude spacing)[2] coupled to a slab ocean model. Details of the experiments we use are described in Williams et al. (2009), Sherwood and Huber (2010), Caballero and Huber (2010, 2013), Zamora et al. (2016) and Korty et al. (2016), but the relevant features are introduced here.

Three experiments using modern-day geography and aerosol forcing differ only in their levels of CO_2. The control case (M-Ctrl) has 1990-levels of CO_2 (355 ppm); another (M-3) is run to equilibrium with three doublings of preindustrial era levels (2240 ppm); the hottest case (M-5) is run to equilibrium with five doublings of preindustrial era levels (8960 ppm). These feature progressively hotter surface conditions and are far larger departures from the modern day climate than have been examined in tropical cyclone-climate studies before. Zamora et al. (2016) assessed changes in middle and high latitude lapse rates in these three simulations, finding that lapse rates neutral to

---

[2] This resolution is marginal for using most detection algorithms to identify explicitly simulated events, so we limit our consideration to results of the downscaling method, which does not require the global model to have high resolution.

moist convection become increasingly common in the extratropics in the hotter simulations. As we show in Chapter VII, these conditions permit tropical cyclones to expand to new territory; these results are also reported in Korty et al. (2016).

Camargo and Zebiak Vortex Tracking Algorithm

To identify and track TCs in the LGM, Mid-Holocene, and 20th century experiments with CCSM4, we have adopted the Camargo and Zebiak (2002) algorithm (henceforth CZ02), which will be briefly summarized below (for a more comprehensive overview, see Camargo and Zebiak 2002, Camargo et al. 2005). First, the algorithm searches for regions that exceed thresholds of ~3.5 x 10^{-5} s^{-1} absolute value relative vorticity, ~1.5°C positive vertically integrated temperature anomaly, and ~11 m/s surface wind speed (these are all model dependent thresholds, but the values included here are those used with CCSM4 and will be further explored in the Chapter III). Next, a matrix of grid boxes[3] centered on the region where the thresholds were exceeded is defined, and is used to search for anomalies at the following the time step (6 hours later in our dataset). The algorithm again searches the matrix for a relative vorticity anomaly that exceeds the threshold. Should a point in the matrix where the threshold is exceeded be found be found again, the process is repeated and the points are linked as a segment of a tropical cyclone track. In addition to the vorticity threshold, other thresholds must be met such as the surface wind speed, temperature anomaly at four pressure levels (850,

---

[3] The size of the matrix is resolution-dependent, but is intended to be wide enough to compare the TC core temperature with its environment. In T42 resolution, Camargo and Zebiak (2002) used a 7 x 7 grid box.

700, 500, and 300 hPa), and surface pressure. The temperature anomaly must be positive at each of the pressure levels and be greater at 300 hPa when compared to 850 hPa, while the mean wind speed should be larger at 850 hPa than at 300 hPa, and the sea level pressure minima is centered within the box. The algorithm continues to iterate until one of these criteria is not met, and the storm track is then designated as complete. Upon completion of detection of all storms during the time period, an assessment of possible duplicate or piecewise storms is made. Once the tropical cyclone climatology has been created duplicate storms are removed (those that contain similar track data yet were found to start from different initial disturbances). This evaluation makes the algorithm more accurate by removing bogus tropical cyclones.

Model resolution affects the number of features that tracking algorithms have been able to identify and follow, with coarser runs generally yielding fewer storms than found in nature. Each run of CCSM4 considered here has common resolution of T85 (about ~1° by 1°) and produces fewer storms in its 20th century run than observed in nature (Camargo 2014); we compare with the period between 1981-2005 when about 80 storms year^{-1} were observed globally. Here we present an example of one of the storms from CCSM4's 20th century run to illustrate the TC-like structure that GCMs of this resolution produce.

Figure 3 shows a typical storm generated by the CZ02 algortihm for a variety of environmental variables: sea-level pressure, 850 hPa vorticity, 300 hPa temperature, and surface wind speed. This particular storm is generated from a CCSM4 20th century experiment, and is taken at the point it reaches its storm lifetime maximum intensity (the

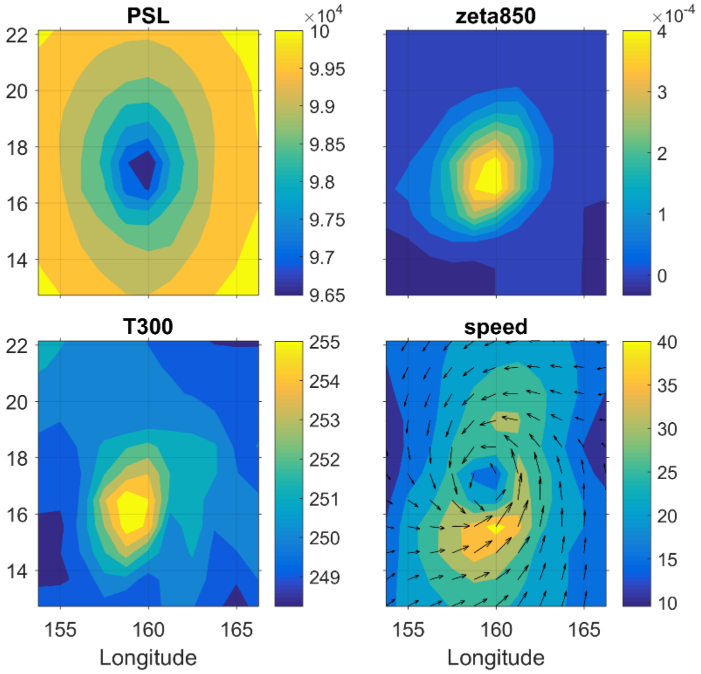

Figure 3 Example of a storm detected by the CZ02 algorithm showing (a) sea-level pressure, (b) 850 hPa vorticity, (c) 300 hPa temperature structure, and (d) surface wind speed.

specific climatology of these storms will be further explored in the following Chapter). This tropical cyclone has a local minima in sea-level pressure (though this value along with variables determining intensity such as wind speed is sensitive to the coarse resolution) coincident with a low level relative vorticity maxima. In addition there is a warm temperature anomaly aloft near the center of the storm and the surface wind field shows a clear cyclonic circulation. The sizes of individual storms vary, but many are larger than found in nature (likely a result of the coarseness of the horizontal resolution). It should be noted that while this specific storm is representative of a Category 1 storm in the dataset, a number of weaker storms show similar structures, yet less organized. In operational tropical cyclone forecasting, a closed circulation is necessary to be seen in order to classify a disturbance as a tropical depression.

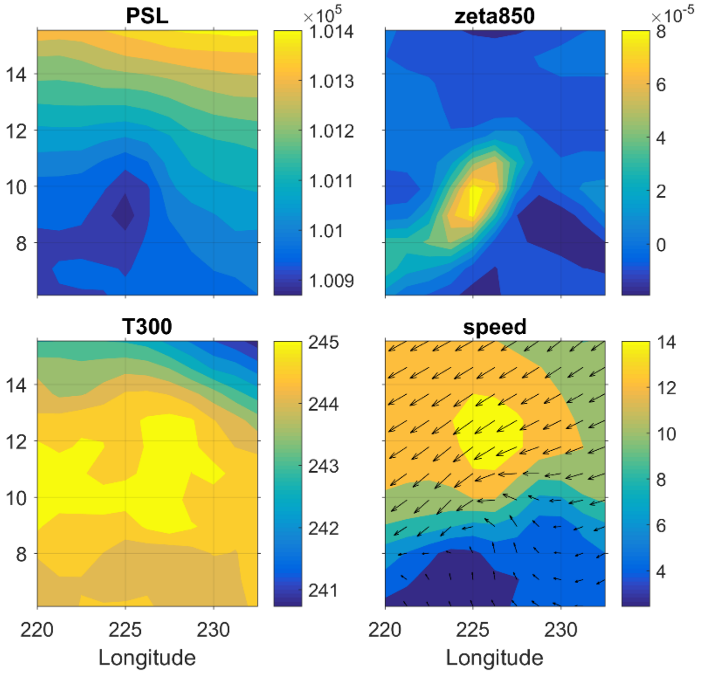

Figure 4 Example of an atypical storm detected by the CZ02 algorithm displaying local (a) sea-level pressure, (b) 850 hPa vorticity, (c) 300 hPa temperature structure, and (d) surface wind speed.

However, a number of storms (~15% of 20th century storms generated out of a single year, when visually examined) lack a clearly closed surface cyclonic wind field, yet still pass the objective definitions used by the CZ02 algorithm. The number of these more questionable features is sensitive to choices in vorticity and other thresholds used in the algorithm, and more restrictive values can eliminate a number of weak systems. We explore this sensitivity in the next chapter. **Figure 4** is similar to **Figure 3** but for one of the ~15% of systems tracked that nevertheless lacks a clearly cyclonic circulation. While the criteria for the vortex tracking algorithm are met (positive temperature anomaly, strong relative vorticity, and minima sea level pressure relative to nearby grid points), this storm in particular lacks a closed circulation at the surface. The wind pattern shown in **Figure 4d** resembles that of an open tropical wave rather than a closed tropical cyclone. The direction of surface wind is easterly on its equatorial side, where as a Northern Hemisphere tropical cyclone with a closed circulation would feature westerly winds in this region. In the operational forecasting of tropical cyclones (such as done by the National Hurricane Center), a tropical disturbance requires a closed circulation before it is classified as a tropical cyclone. While stronger modeled storms do not demonstrate the disorganization in TC structure seen in **Figure 4**, a few weak storms do, which highlights that some additional objective definition for the surface wind field may improve the quality of tropical cyclone detection algorithms.

Emanuel Downscaling Method

In Chapters V and VI, we apply the downscaling method developed by Emanuel (2006; also see Emanuel et al. 2008) to the PMIP3 models described earlier. In Chapter VII, we apply it to experiments with CAM3 that feature very high levels of CO_2. The technique is described further in Emanuel (2006, 2013) and Korty et al. (2016), but we review the procedure here.

Emanuel (2006) developed a downscaling method that places a large number of weak vortices (their initial surface velocity is ~10 m/s), randomly distributed in space and time across all oceans in the output of a global climate model. These vortices are advected by statistics drawn from the 850 and 250 hPa wind at each location and a beta drift that induces a poleward bias to the tracks. Along each path, the axisymmetric coupled hurricane model CHIPS (Emanuel et al. 2004) is run, and if the initial vortex grows in the environment through which it passes, it becomes a storm added to the database. The vast majority of these initial seeds fail to develop, however, as most are embedded in thermodynamically unsuitable environments, subject to strong vertical wind shear, or fail to develop due to internal inabilities to maintain a saturated column in the presence of dry air. The total number of seeds necessary to generate a pre-selected number of successful cases is used to calibrate the results and define an annual frequency. We generate ~5,000 events for each model in the PMIP3 set, and ~10,000 events for each simulation using the high CO_2 CAM3 experiments described in Chapter VII. This affords us a large enough dataset to examine changes in frequency, intensity,

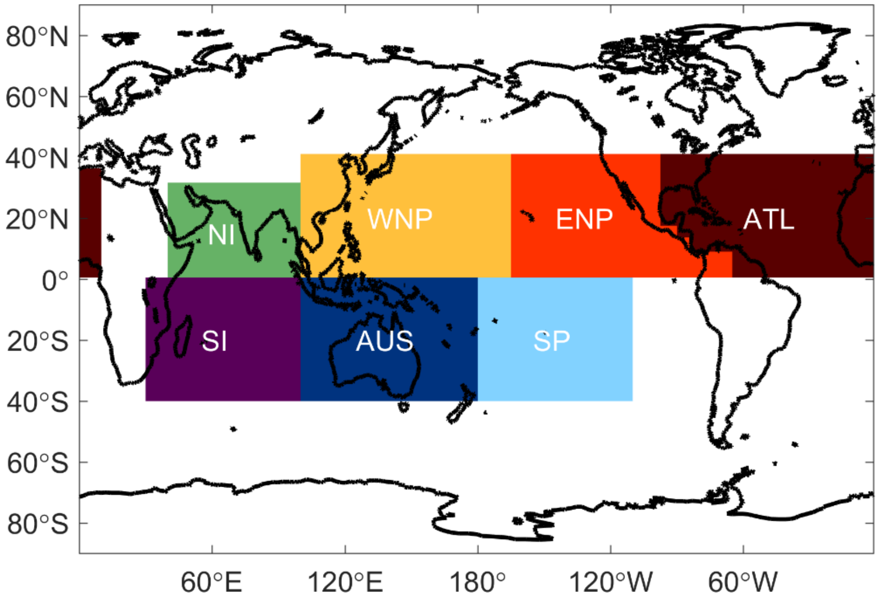

Figure 5 Map of ocean basins (adapted from Camargo et al. 2007). Identified as NI = North Indian, WNP = Western North Pacific, ENP = Eastern North Pacific, ATL = Atlantic, SI = South Indian, AUS = Australian, and SP = South Pacific.

lifetime, and geographic distribution across climates. Additional detail is provided in Chapter VII.

Finally, throughout this thesis we will refer to some aspects of activity by basin. **Figure 5** shows the definitions of the various basins along with their abbreviations that we use in later chapters; these follow the conventions adopted by Camargo et al. (2007).

CHAPTER III

LAST GLACIAL MAXIMUM – EXPLICITLY TRACKED STORMS

Studies of climate change and tropical cyclones have employed several techniques that can be broadly grouped into three categories: (1) explicitly tracking warm-core vortices simulated directly by global climate models (e.g., Camargo 2013); (2) investigations of how the large-scale environmental conditions necessary for tropical cyclones evolve in other climates (e.g., Vecchi and Soden 2007; Camargo et al. 2007; Korty et al. 2012); (3) dynamical or statistical downscaling of global climate model output to higher resolution models capable of better resolving tropical cyclones structure and intensity (e.g., Emanuel 2013; Knutson et al. 2015). In this Chapter, we apply the first of these methods to the Last Glacial Maximum (henceforth LGM) simulation of CCSM4, taking its 20th century simulation as a control case. (Although preindustrial era simulations are often used as a control for paleoclimate studies, as we noted in the last Chapter, the 20th century is chosen here as it is the only period for which global records of tropical cyclones exist.) The chapters that follow will apply the other methods to the LGM simulations.

We begin this chapter by presenting statistics on the tracks identified in both the LGM and 20th century experiments using the Camargo and Zebiak (2002) algorithm that was reviewed in Chapter II, followed by a study of the sensitivity of the algorithm to modifications in the assumptions used to define and follow these systems. We conclude with an analysis of the latitudes at which storms form in both climates.

Climatology of Vortices

The tracks of TCs found by the CZ02 algorithm are shown in **Figure 6** along with those from the historical record (1981-2005) of the IBTrACS datasets (Knapp et al. 2010). We limit the historical record to years beginning with 1981 owing to limited global data in earlier decades (Schrek et al. 2014). Comparing the explicitly generated

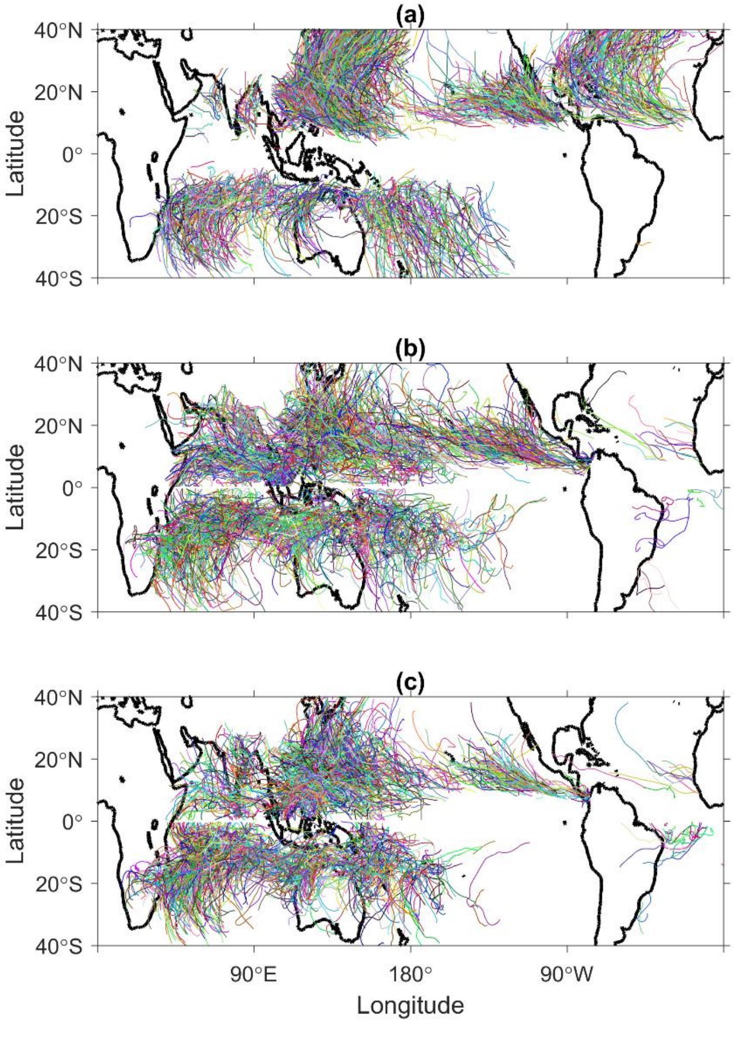

Figure 6 Tropical cyclone tracks for (a) historical storms 1981-2005 (IBTrACS dataset), and generated using the CZ02 algorithm for (b) 20th century and (c) Last Glacial Maximum experiments.

features in CCSM4's 20th century simulation (**Figure 6b**) to those of the historical record (**Figure 6a**) reveals that TCs are generated in many of the same places seen in the observed climatology, with the notable exception of the Atlantic Ocean where CCSM4 continues a long-standing bias of generating too few storms. This bias is due to anomalously colder Atlantic sea surface temperatures, possibly caused by a mean sea level pressure bias in the region in the atmospheric component of the model (Grodsky et al. 2012), and has been a persistent feature in many of CCSM4's predecessors. The 20th century simulated tracks (**Figure 6b**) also have a higher amount of storms than the historical record in the Indian and north central Pacific oceans, and simulated storms track much nearer to the equator than seen in observations. While limited in number, CCSM4 produces a few storms in the South Atlantic, where they are largely absent in the historical record (a single event occurred in 2004). CCSM4 produces storms in largely the same places in the LGM simulation as it does in its 20th century run.

As there are 2,012 tracks in the historical record, 2,009 in the 20th century simulation of CCSM4, and 1,586 tracks CCSM4's LGM simulations, track densities are a useful way to compare changes and better see the differences. To form the total track densities, a 5° latitude by 5° longitude grid is defined, and each 6 hourly position of every storm adds 0.25 to the grid cell in which it located at the time. Iterating this over all the time steps for the simulation and then normalizing by number of years yields a track density (in units of number of storm days per year for each box). The resultant track density for the tracks plotted in **Figure 6** is shown in **Figure 7**.

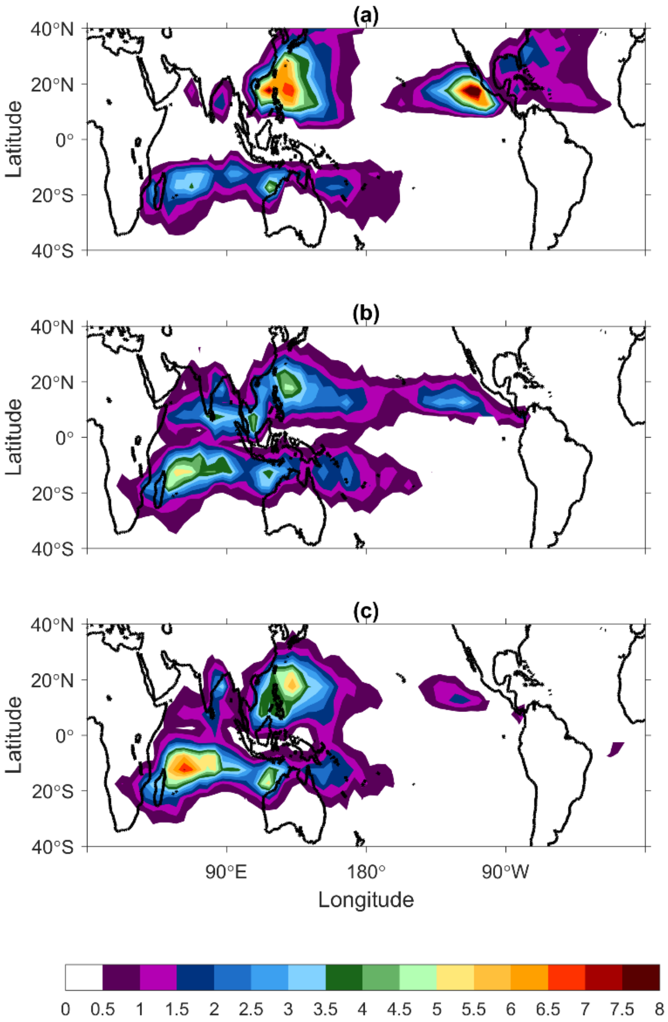

Figure 7 Annually averaged tropical cyclone track density for (a) historical storms 1981-2005 (IBTrACS dataset), and generated using the CZ02 algorithm for (b) 20th century and (c) Last Glacial Maximum experiments. Values shown are in number of storm days per year for each 5° x 5° box.

One noticeable difference is that the poleward termini for the Northern Hemisphere simulated tracks occur at latitudes farther south than in historical TCs, and there are significantly higher track densities near the equator in CCSM4 than in observations. TCs formed in the Indian Ocean favor the southern region of the basin for LGM storms and the northern region for 20th century storms. Likewise, Pacific TCs favor the western region of the basin during the LGM, while having a much larger 20th century track density in other regions (especially in the east Pacific). TCs in the Atlantic Ocean are too few to yield significant track density in both climates.

	Historical (1981-2005)	**20th century**	**LGM**
Tropical mean SST	--	**26.44°C**	23.54°C
Global mean SST	--	**11.02°C**	6.09°C
Number of TD	--	**20.91**	13.77
Number of TS	37.80	31.86	**33.39**
Number of H1	18.52	3.60	**3.68**
Number of H2	10.16	**0.91**	0.26
Number of Major Storms	14.00	**0.11**	0.06
Total number of Tropical Cyclones	--	**57.40**	51.16
Number of TS+	80.48	36.49	**37.39**

Table 1 Average number of historical (1981-2005) and CCSM4 20th century and LGM sea surface temperatures *SST* and storm counts by intensity. Bold fonts indicates the larger of the two climates' value. Values for storm counts are in number of storm per year. Historical record originates from a global best track dataset (IBTrACS).

Table 1 shows general statistics of the storms, including a breakdown of the number of storms by TC classification. Comparing the statistics of observed systems to those simulated in the 20th century experiment, we note that the model produces fewer events than nature and that its intensity distribution is shifted to weaker events that are abruptly truncated by the model's coarse resolution. (Less than one storm each year reaches a peak intensity that exceeds category 1 status.) In fact, 36% of the 20th century features identified by the algorithm have maximum surface winds that never reach tropical storm force. These deficiencies limit the utility of explicitly resolved features in models of this resolution to studying changes in the climatology that are related to frequency, genesis, and geographic distribution, but we will see below that even some of those properties can be sensitive to definitions of what constitutes a system.

Overall, while having fewer storms generated (-10%) in the Last Glacial Maximum, there are a greater number of storms that reach tropical storm (TS) intensity and higher. Omitting the number of tropical depressions (TDs) in each climate yields a higher genesis count (+2%) for LGM storms (however this change is not a statistically significant difference). Given the sensitivity to the treatment of tropical depressions, in later parts of this chapter I consider how my analysis might differ if the dataset were restricted to only the subset of events that feature tropical storm force winds at some point in a storm's lifetime.

Figure 8 plots the distribution of the zonally averaged genesis density by latitude and month that exceed 0.1 events per 1° latitude area per year. The range of months of tropical cyclone genesis is shifted in the Northern Hemisphere (NH) simulations from that of observed storms. Observed NH storms start ~mid-May and end in December, while 20th century storms begin in mid-June and end at the end of January. Furthermore, the poleward extent of the latitude at which NH storms form in the 20th century

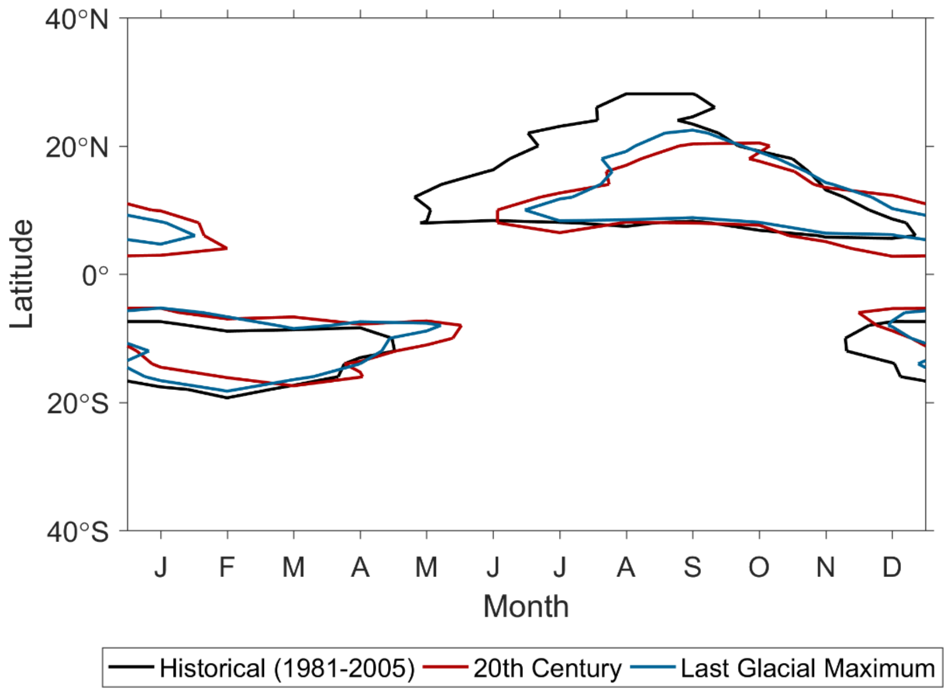

Figure 8 Annually averaged cycle of genesis density by latitude and month that exceed 0.1 events per 1 degree latitude area per year for historical (black), 20th century (red), and Last Glacial Maximum (blue) experiments.

simulations lies ~8° latitude equatorward of observations during the peak months of the season. The Southern Hemisphere (SH) distribution shows greater similarity between simulation and observations, although the end of the season extends into mid-May (mid-April in observed storms). Simulated events also form at latitudes nearer to the equator than in nature in both hemispheres of the model.

Comparing the distribution of genesis in the simulations of the LGM and 20th century storms shows their distributions to be similar, though the genesis period shortens slightly (~1 or 2 weeks) in LGM (primarily during the NH season). This contraction of season length in the colder LGM simulation is consistent with the expansion of the genesis period that Dwyer et al. (2015) reported in anthropogenic climate change studies. One surprising difference is the slight poleward expansion of genesis during the

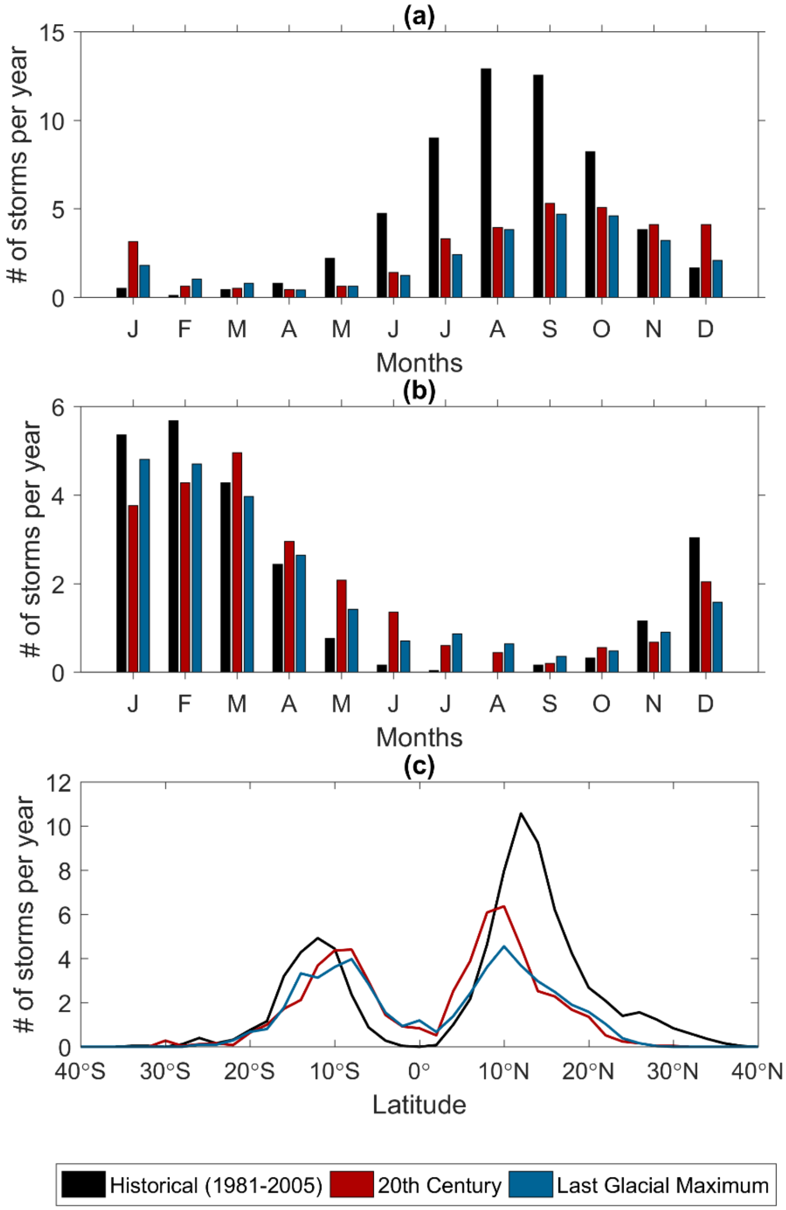

Figure 9 Annually averaged number of storms by month for (a) Northern and (b) Southern Hemispheres. (c) Annually averaged number of storms by latitude. Historical storms (1981-2005) are shown in black. Explicitly resolved 20th century storms are shown in red, while LGM storms are shown in blue.

peak of the each hemisphere's season in the LGM.

Figure 9a and b shows the average number of tropical cyclones per month for 20th century (red), and LGM (blue) as output by the CZ02 algorithm for Northern and Southern Hemispheres, respectively. The number of systems simulated by the global model is significantly lower during the Northern Hemisphere season compared to observations (Shaevitz et al. 2014). (This is partly owing to the inability to simulate events in the Atlantic; we discuss the events confined to the Eastern Hemisphere below.) The peak is smaller and occurs later in the model than in nature, and there are more events simulated during the winter (December to February) than occur in nature. The model's Southern Hemisphere produces about the correct number of events but is likewise shifted to a later peak (March, compared to January-February in observations) with more fall and winter activity (April to September) than observed. It is also of note that there are some months when counts of SH LGM storms are higher than in the 20th century. The total number of model-detected storms in the LGM is reduced in the Northern Hemisphere when compared to the 20th century, however, the distribution of the annual cycle is comparable.

Figure 9c shows the distribution of storm genesis by latitude and reveals a model bias for generating too many storms near the equator and too few poleward of 10 degrees latitude. The number of Northern Hemisphere storms is particularly underestimated at latitudes poleward of 10 degrees, but a large part of this error arises from CCSM4's lack of activity in the Western Hemisphere (the Atlantic, as noted earlier, but to a lesser extent the eastern North Pacific too). Restricting the domain to the Eastern Hemisphere,

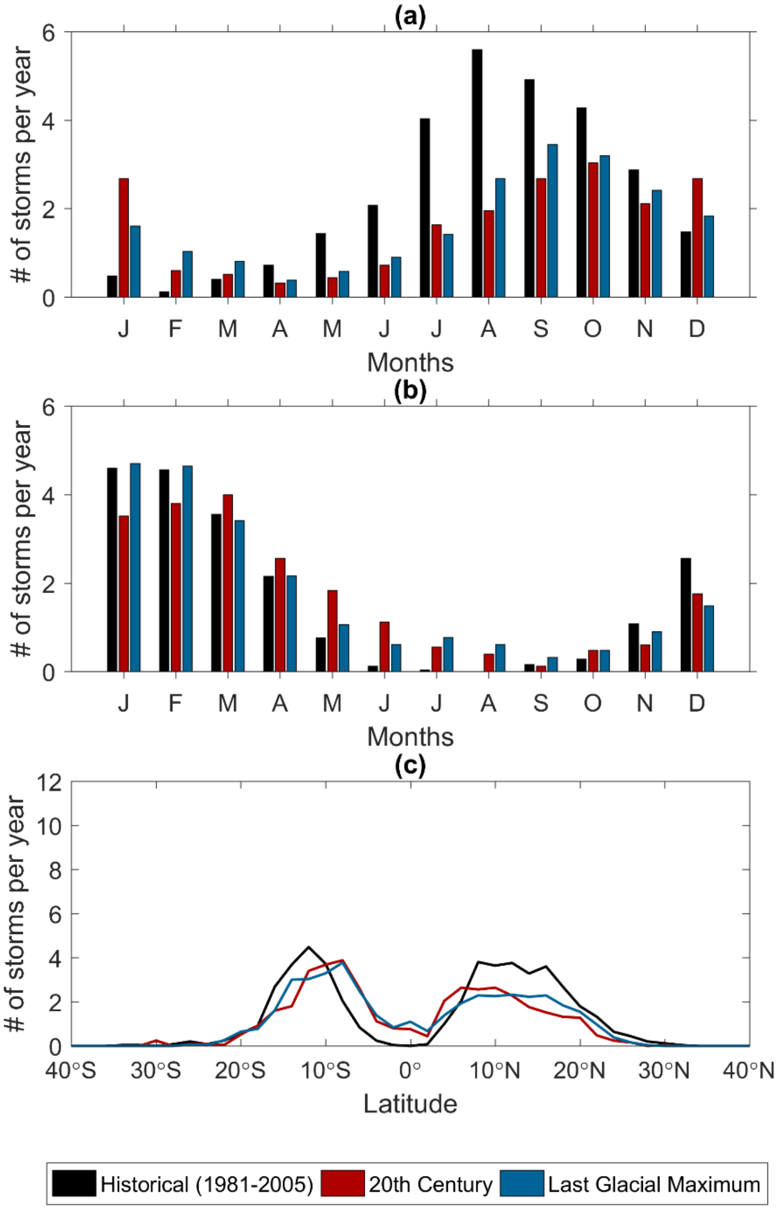

Figure 10 As in Figure 4, but for Eastern Hemisphere events only.

the total counts are much more similar (**Figure 10**), although the bias of producing too many events near the equator remains. The seasonal cycle of modeled storms in the northeastern quadrant (i.e., Eastern Hemisphere north of the equator) shows much weaker amplitude than observed in nature: counts are smaller during the peak months of the season and larger counts during offseason. The cycle of events south of the equator in the Eastern Hemisphere is similar to those observed but lingers into autumn and winter. (There is little difference between this and **Figure 9** showing global SH---because few events occur east of the International Dateline in the Southern Hemisphere at all.)

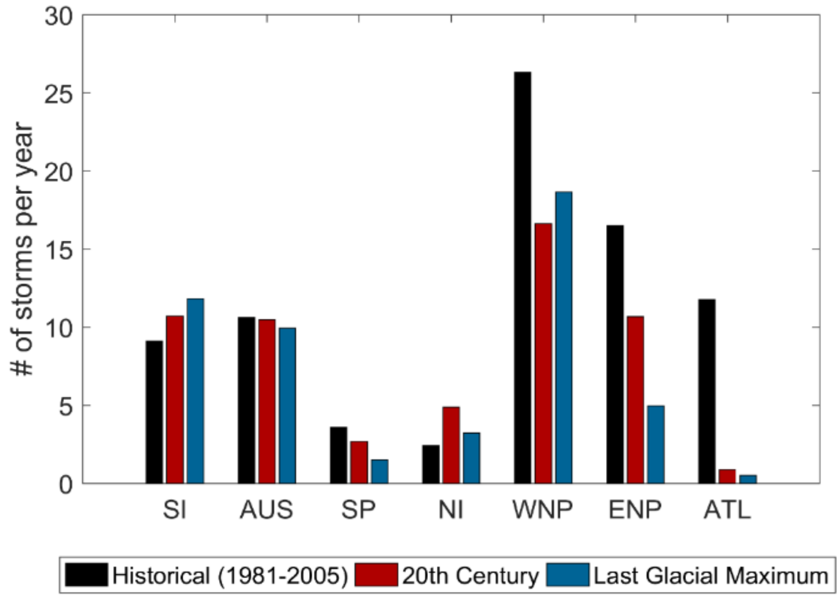

Figure 11 Annually averaged number of storms by basin for historical (black), 20th century (red), and Last Glacial Maximum (blue) experiments.

Figure 11 shows the distribution of the genesis of storms by basin. In addition to a deficiency in generating Atlantic storms as discussed above, the CZ02 algorithm also fails to predict the number of storms in both the western north and eastern north Pacific and over predicts activity in the Indian basins. Both the global and the sum of northern hemisphere storm counts show a statistically significant difference between the two experiments, but only show significance in South Pacific, North Indian, and eastern North Pacific basins. The sensitivity of these counts to the thresholds chosen will be explored in the next section of this chapter.

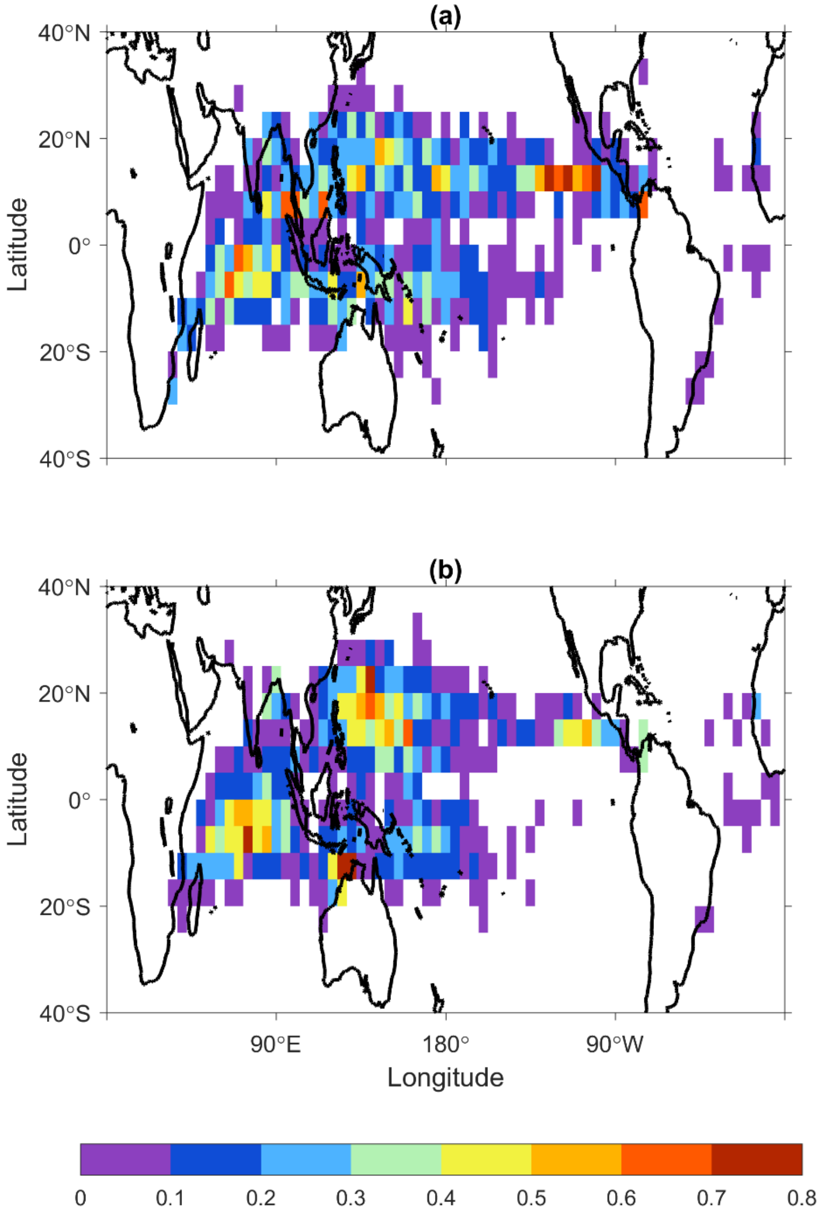

Figure 12 Annually averaged tropical cyclone genesis density (binned by 5° x 5° grid boxes) for (a) 20th century and (b) LGM storms.

Figure 12 shows the tropical cyclone genesis density for the vortices explicitly simulated in the (a) 20th century and (b) LGM. This data was interpolated into 5° longitude by 5° latitude grid boxes (as was done for track density in **Figure 7**). Even considering the larger number of total storms in the 20th century simulation, there are some regions (130°E – 170°E, 5°N – 30°N; 60°E – 90°E, 15°S – 10°N) where there is a larger density of LGM storms generated. This can be more clearly seen in **Figure 13**,

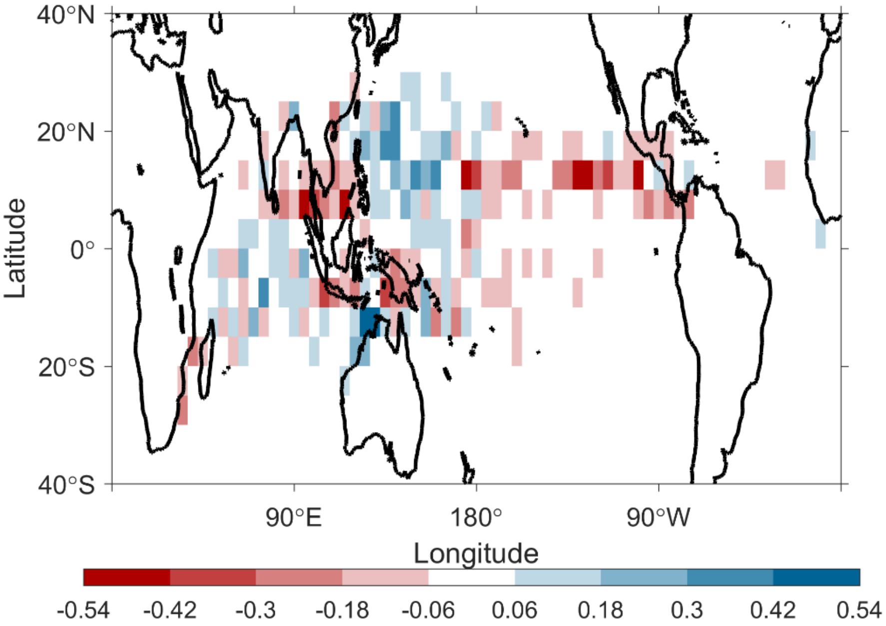

Figure 13 Annually averaged tropical cyclone genesis density difference between LGM and 20th century shown in **Figure 12**. Positive (blue) values indicate regions of higher genesis density in LGM experiments, while negative (red) values indicate regions of higher 20th century genesis density.

which plots the difference between them (LGM-20th century). Conversely, the central to eastern North Pacific region has a significantly higher 20th century genesis density.

Although this coarse resolution model does not resolve the intensity distribution of actual events (see earlier discussion and **Table 1**), the model has sufficient resolution to simulate marginal hurricane intensity (H1). While this dataset cannot reproduce the values observed in nature owing to its resolution, it may nevertheless be useful to see if the locations of the most severe wind speeds resolvable change or shift between the

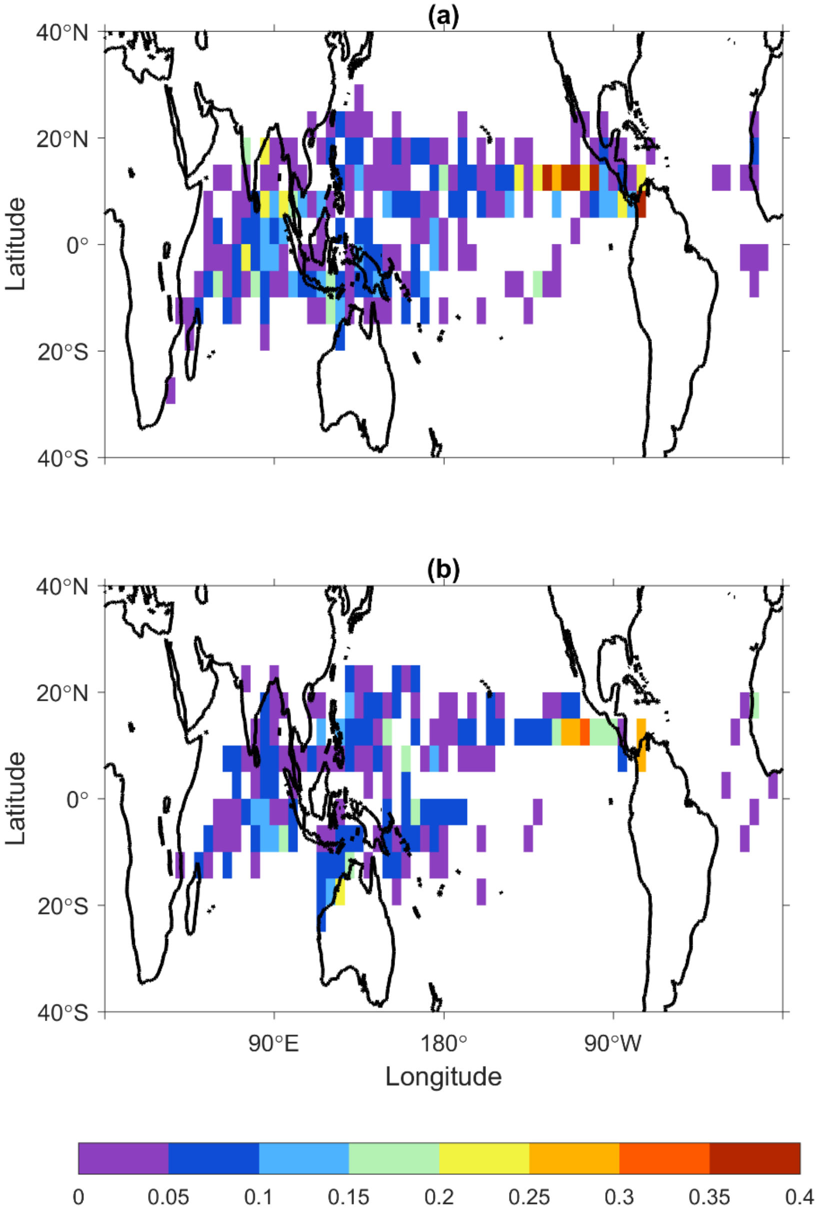

Figure 14 Annually averaged tropical depressions genesis density (binned by 5° x 5° grid boxes) for (a) 20th century and (b) LGM storms.

models' two climate states, and to compare whether the location of the strongest storms in the 20th century run agree qualitatively with those of observations. We defer a more thorough examination of the intensity question to Chapter V, where we consider a downscaling technique that can resolve the full spectrum of possible intensities.

Figure 14 shows the annually averaged genesis density exclusively for tropical depressions (peak intensities ≤ 17 m/s) in 20th century and Last Glacial Maximum climates. These weak storms are generated in similar regions as the storms featuring stronger intensities but show larger genesis frequencies in the Eastern Pacific and Indian Oceans. Examining the difference between these two climates (**Figure 15**) highlights any of the regional differences with climate. The distribution of genesis is generally uniformly distributed for each of the climates, although generally showing larger

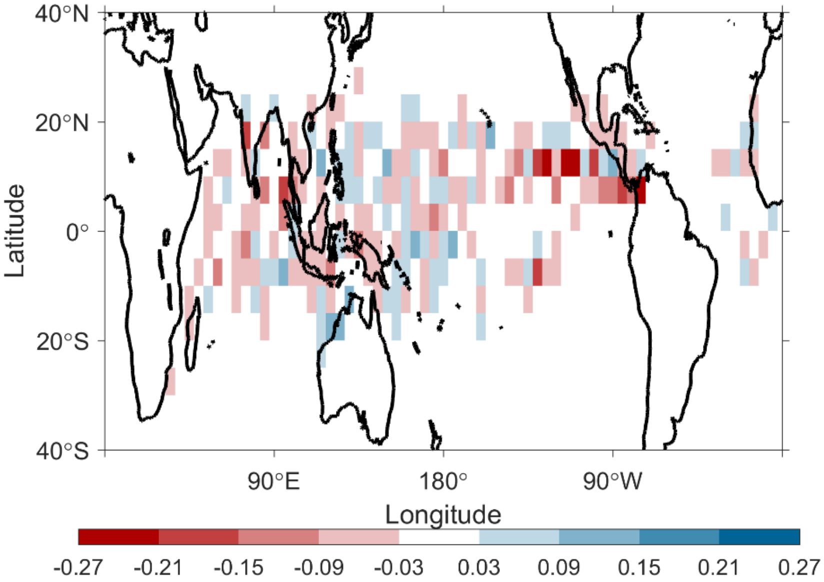

Figure 15 Annually averaged tropical depressions genesis density difference between LGM and 20th century experiments. Positive (blue) values indicate regions of higher genesis density in LGM experiments, while negative (red) values indicate regions of higher 20th century genesis density.

differences in the 20th century as the number of TD for this climate is much larger. The number of storms generated in the Eastern Pacific (specifically near the western coast of Central America) shows the greatest activity in the 20th century.

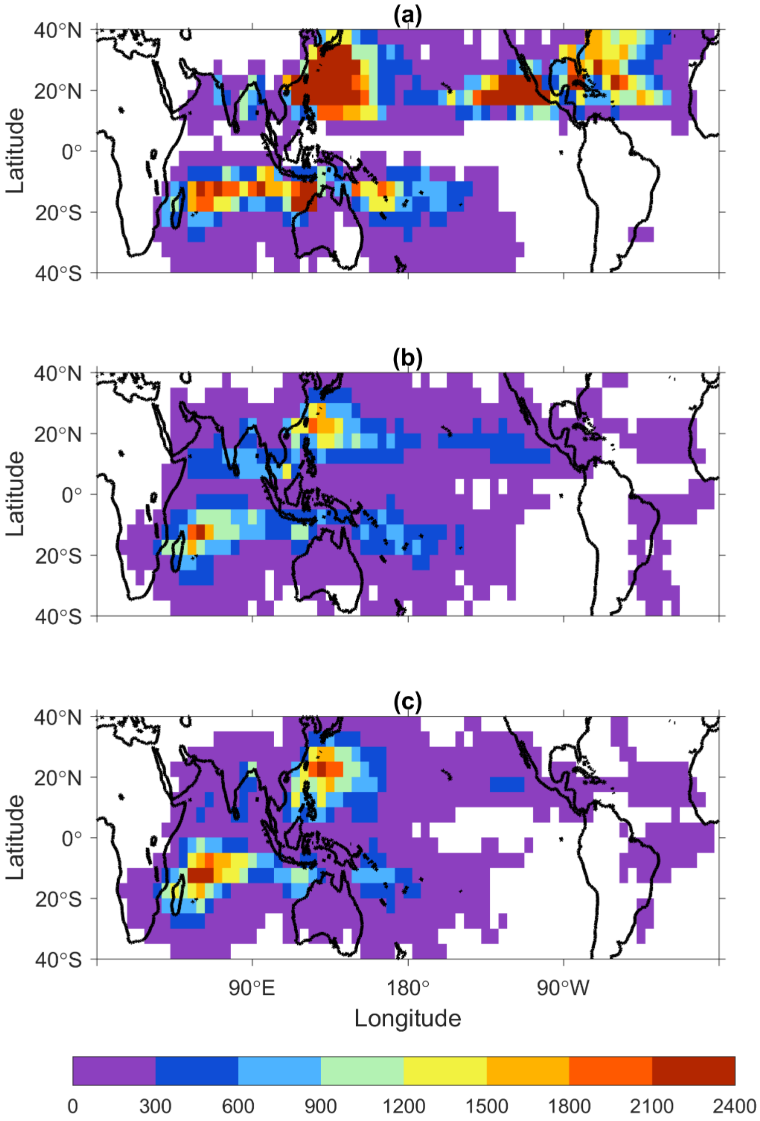

Figure 16 Annually averaged tropical cyclone accumulated cyclone energy *ACE* for (a) historical, and (b) 20th century and (c) LGM simulations. Values shown are in m^2/s^2.

Accumulated cyclone energy (*ACE*; Bell et al. 2000; Camargo and Sobel 2005) is an integrated measure of tropical cyclone activity, and is a function of storm frequency, intensity, and lifetime. It is defined as the integral of the square of the 6-hourly maximum sustained wind speed of all tropical cyclones in a given year (we show the average annual value for each climate here). Actual kinetic energy carried in all tropical cyclones would additionally require integrating the radial wind distribution over the dimensions of every storm, but given the lack of reliable measurements or records of these fields in the historical record, an index based only on the maximum wind speed has been used in the literature (Bell et al. 2000).

Figure 16 shows the tropical cyclone *ACE* density for historical, and 20th century and LGM simulations. The distributions have many similarities between observations and 20th century, albeit with many of the differences shown for genesis density (absence of Atlantic storms and more equatorial activity). Because *ACE* is dependent on intensity, lifetime, and storm count, the value of *ACE* is significantly higher for historical storms, however the globally integrated value for *ACE* is on the same order for historical ($4.83*10^5$ m^2/s^2), simulated 20th century ($1.72*10^5$ m^2/s^2), and LGM storms ($1.60*10^5$ m^2/s^2).

Figure 17 shows the annually averaged difference between 20th century and LGM *ACE* density. Given the limitations coarse resolution models impose on resolving storm intensity, alternate ways of investigating the intensity distribution have been used on GCM data. While increasing resolution permits some examination of the surface wind speed (e.g., Camargo et al. 2014), the low level relative vorticity in the core of the

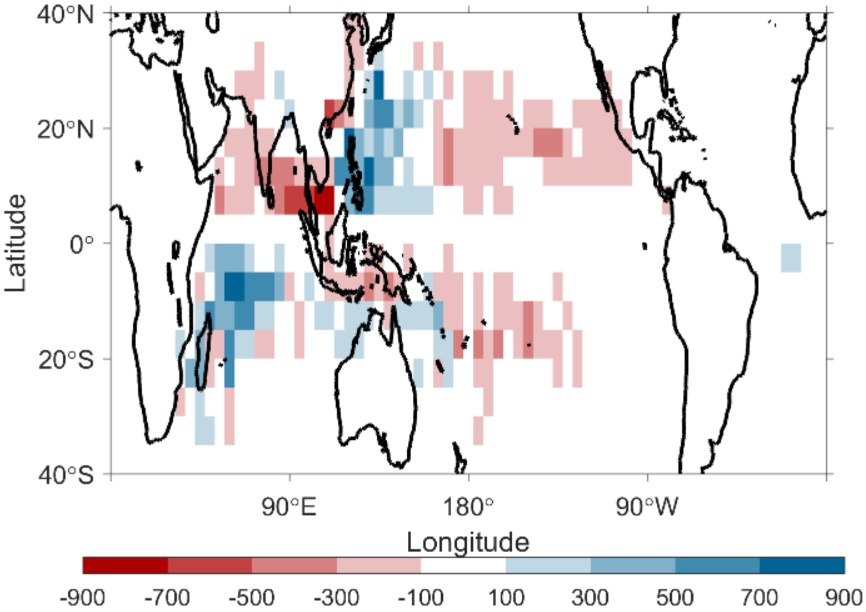

Figure 17 Annually averaged tropical cyclone *ACE* difference between LGM and 20th century storms. Positive (blue) values indicate regions of higher *ACE* density in LGM experiments, while negative (red) values indicate regions of higher 20th century *ACE* density.

storm and minimum surface pressure of the storm have long been used to classify storm intensity in low resolution models (Bengtsson et al. 1982; Lau 1991; Vitart et al. 1997). Values are limited by the resolution of the model, as the area that feature the strongest pressure gradients in the storm is small (typically on the order of tens of kilometers). Furthermore, owing to the vastly different climate properties of the LGM, sea levels were lower (and, therefore, sea level pressures higher) than in the modern world (namely, ice sheets covered much of the LGM, lowering global sea level by more than 100 m). One way to compare systems in the two climates despite this difference is to examine the pressure relative to its average value over the oceans of the tropics (here

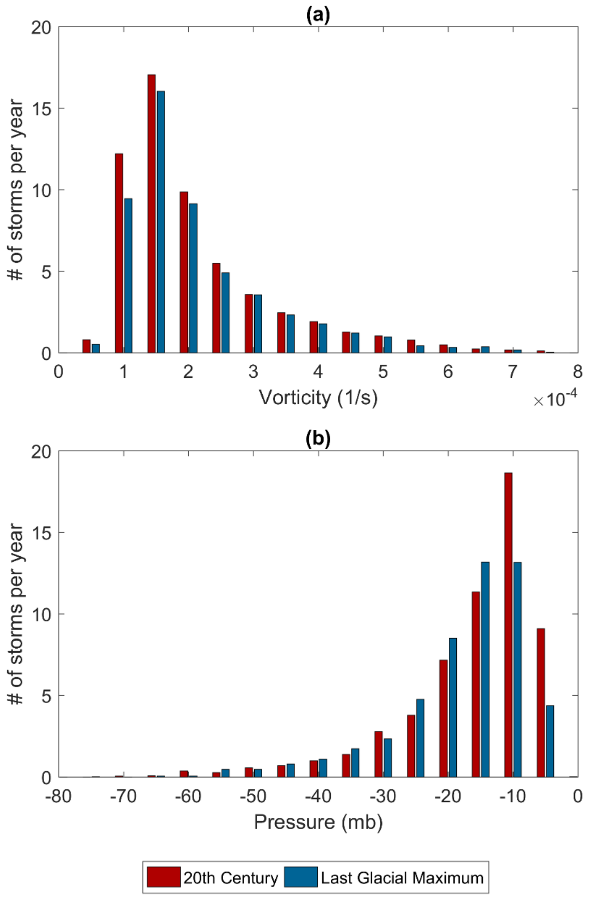

Figure 18 Annually averaged tropical cyclone intensity distribution depicted by (a) 850 hPa relative vorticity and (b) surface pressure depression for 20th century (red) and Last Glacial Maximum (blue) storms.

taken to be ocean regions within the 30°S – 30°N latitude band), a value known as the sea level pressure depression (SLP_{storm} - SLP_{trop_avg}).

Figure 18 shows the tropical cyclone intensity distribution represented by (a) storm lifetime maximum 850 hPa relative vorticity and (b) the storm lifetime minimum sea level pressure depression. Low values of maximum vorticity, representing weak storms, are the most frequent, with higher values becoming increasingly less frequent. The distributions between 20th century and LGM have similar structures, albeit with higher frequencies for 20th century storms due to their higher annual counts. Similarly, minimum sea level pressure depression has similar distributions in both the 20th century and LGM, with the majority of events featuring depressions of ~20 hPa (by comparison, the strongest storms in nature may feature surface pressures near 900 hPa, more than 100 hPa lower than mean tropical sea level pressures; minimal hurricanes typically have pressures of ~990 hPa or lower, a depression of ~20 hPa from the environment). Normalizing this data (not shown) by the number of storms for each climate (rather than the number of years) yields a distribution that favors the weakest storms (lower value for

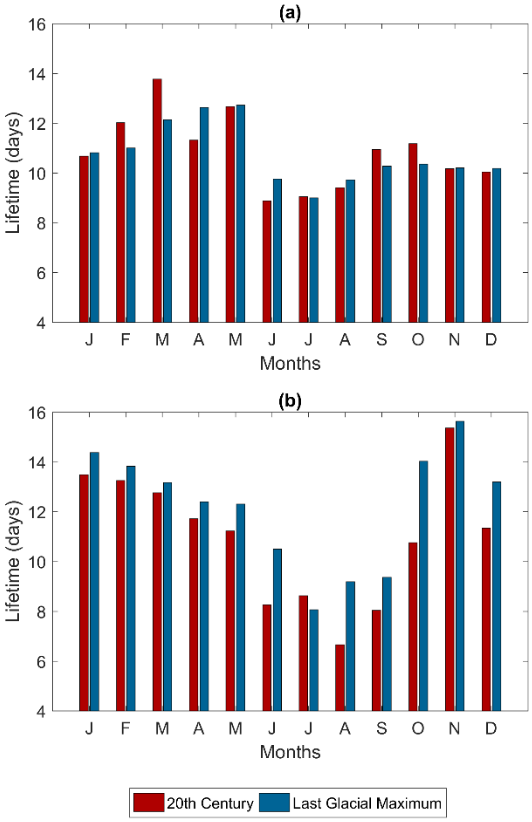

Figure 19 Monthly averaged tropical cyclone mean lifetime climatology for (a) Northern and (b) Southern Hemisphere 20th century (red) and Last Glacial Maximum (blue) storms.

vorticity and surface pressure depression within the first couple bars) in the 20th century, then favoring the LGM (for the next couple bars), and then the differences between the two become negligible. This is consistent with the distribution of TC type (**Table 1**) which shows a larger number of weak storms in 20th century.

Figure 19 shows the climatology of average storm lifetime by month for all 20th century and LGM storms. LGM storm lifetimes by month are generally longer, especially in the Southern Hemisphere and lifetimes of Southern Hemisphere storms in both experiments are longer (1.72 in 20th century and 2.72 days in LGM). In addition, Northern hemisphere storms have a smaller variation of lifetimes by month. However, excluding tropical depressions (not shown) from this dataset, favors longer 20th century storm lifetimes. Changes in the globally averaged lifetime values show a statistically significant change between the two experiments, favoring the LGM. When examining the differences between the two experiments by category, LGM tropical depressions have a statistically significant longer lifetime, while the same is true for 20th century tropical storms.

Sensitivity Tests

Given the fact that many of the systems identified in the previous section are weak, and that Horn et al. (2014) showed that different tracking algorithms can produce very different track sets, we explore sensitivity to the assumptions and parameters used to identify and track systems in this section. While all of the detection routines employed by global modeling centers search for some common characteristics, including anomalously cyclonic low-level vorticity and positive temperature anomalies in the middle and upper troposphere, many differ in the thresholds used to identify and follow systems and in the altitude at which data are examined (Horn et al. 2014). Sensitivity to the thresholds within a single algorithm is explored in this section.

Here we run sensitivity tests on the Camargo and Zebiak (2002) vortex tracking algorithm by varying the thresholds that must be met in order to classify an initial vortex as a tropical cyclone. These thresholds are usually calculated within the algorithm itself, using the standard deviations of vorticity, surface wind speed, and temperature within the model to define them, but the algorithm can be modified to enforce user-prescribed values. Even in the standard approach of calculating thresholds from variances has been employed in different ways in the literature, some defining basin-dependent thresholds based on regional variability (Camargo and Zebiak 2002), with others applying a single, globally defined threshold (Vitart and Stockdale 2001). Our standard dataset presented in the previous section follows the latter method here, but a consequence is that it yielded few events in some basins.

Yet another consideration is in the way such thresholds are applied to other climates. For climate change studies of the next century, the most common approach has been to apply the thresholds defined in the control (late twentieth century) climate simulation to the future simulation, but there has been discussion about using the variances from the differing climates to define their own climate-specific thresholds (S. Camargo, personal communication 2015). As the LGM features a climate whose means and variances are farther removed from modern control states, we feel the issue requires further examination here than is customary in anthropogenic studies.

As we saw in **Table 1**, while the number of storms generated in CCSM4 was larger in the 20th century when compared to the Last Glacial Maximum, a large number of these storms were classified only as reaching tropical depression intensity. Moreover, excluding tropical depressions in the total count of storms yields a higher number of LGM storms than found in 20th century. Altering the thresholds used in determining initial vortices will most influence the number of these weak storms, and thus our goal is to examine the breadth of their sensitivity to the tropical cyclone statistics.

Thresholds	σ_{temp}	σ_{vort}	σ_{speed}
20th century	1.6204 K	3.8493E-5 s^{-1}	11.4820 m/s
Last Glacial Maximum	1.6268 K	4.1898E-5 s^{-1}	11.9882 m/s

Table 2 Thresholds for vertically integrated temperature anomaly, vorticity, and surface wind speed as determined by 20th century and LGM CCSM4 experiments.

Table 2 shows the values of the thresholds as generated by the individual datasets. Larger values of a threshold are more restrictive, while smaller values are more relaxed. Each of the LGM generated thresholds are larger than the 20th century values, but with differences < 10%. These thresholds are generated from the mean values of the threshold variable in the basins as determined from **Figure 5.**

We first examine the effects of establishing climate-specific thresholds used in the vortex tracking algorithm by comparing two sets of tracks generated using alternate methodologies: (1) we follow the usual convention of establishing thresholds for the control (20th century) climate and apply these thresholds to both 20th century and LGM climates and (2) generate tracks for each climate using thresholds determined by their respective variances.

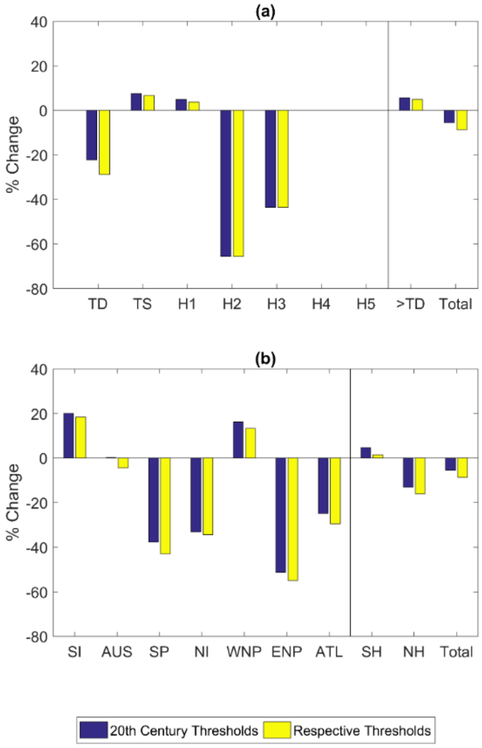

Figure 20 Percentage change of number of storms generated in LGM and 20C simulations by (a) category and (b) basin for tracks using thresholds generated from the 20th century (blue), and respective (yellow) datasets. The respective dataset uses 20C generated thresholds for 20C, and LGM generated thresholds for LGM.

The results of these changes are shown in **Figure 20**. Each bar shows the percent change in the number of storms between LGM and 20th century (20C) by (a) intensity and (b) basin for the two configurations described above. Changes are calculated relative to the 20th century value (i.e., values shown are given by 100*[LGM-20C]/20C).

While the total number of storms generated changes depending on the threshold used, each configuration yields a larger number of 20th century storms than in the Last Glacial Maximum. This is due to fact that the LGM thresholds are more constrictive than their 20C counterparts, which yields a larger positive percent change predominantly from a larger decrease in the number of 20C storms (although the number of LGM storms also decreases). Using Welch's *t*-test, we test the significance of the differences in these changes by basin and intensity. For either configuration of thresholds, the changes in Australian, western North Pacific, and Atlantic basins (where few storms exist) cannot be determined as significant. The data shows that while the absolute value changes, in no case does the sign of the difference between LGM and 20C reverse, leading us to conclude that the results are not sensitive to switching LGM thresholds to values set by the LGM climate.

Also of note, if the datasets exclude systems whose strongest surface winds never reach tropical storm strength (excluding all tropical depressions; bars denoted by '>TD'), there is a larger number of storms generated in LGM than those found in 20C. Many of the 20C storms (a much larger number than in LGM) are very weak systems with peak wind speeds equivalent to tropical depressions. This shows the results are sensitive to the treatment of the weakest systems, which we explore next by varying the magnitude of perturbations in vorticity, temperature, and wind speed that a system must pass to be detected and classified by the algorithm.

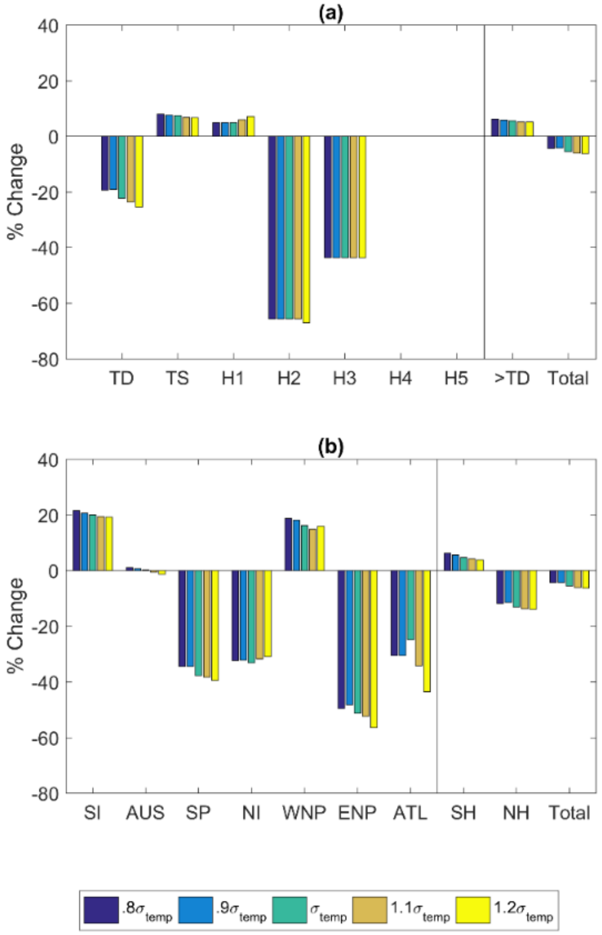

Figure 21 Temperature anomaly threshold sensitivity test. Percentage change of number of storms generated in LGM and 20C simulations by (a) icategory and (b) basin. The middle bar of every group (teal), is using the control case threshold, while the other bars use a threshold multiplied by a factor (shown in the legend).

We now test the sensitivity of the thresholds by varying each in 10% increments. **Figure 21** shows this analysis for changing the magnitude of the vertically integrated local temperature anomaly (using three pressure levels: 700, 500 and 300 hPa) threshold while keeping all other thresholds constant.

Figure 21a show data for tropical depressions (TD), tropical storms (TS), and hurricane categories 1-5 (H1-H5), TS&H, and total counts. The control case (using the 20th century values as in **Table 2**) is the middle bar of each set, with 10% deviations from this displayed adjacent to it. As noted, due to the resolution of the model very few major hurricanes (in fact only H3 category storms) are generated. As the temperature anomaly threshold becomes more restrictive, this favors a slightly larger difference in

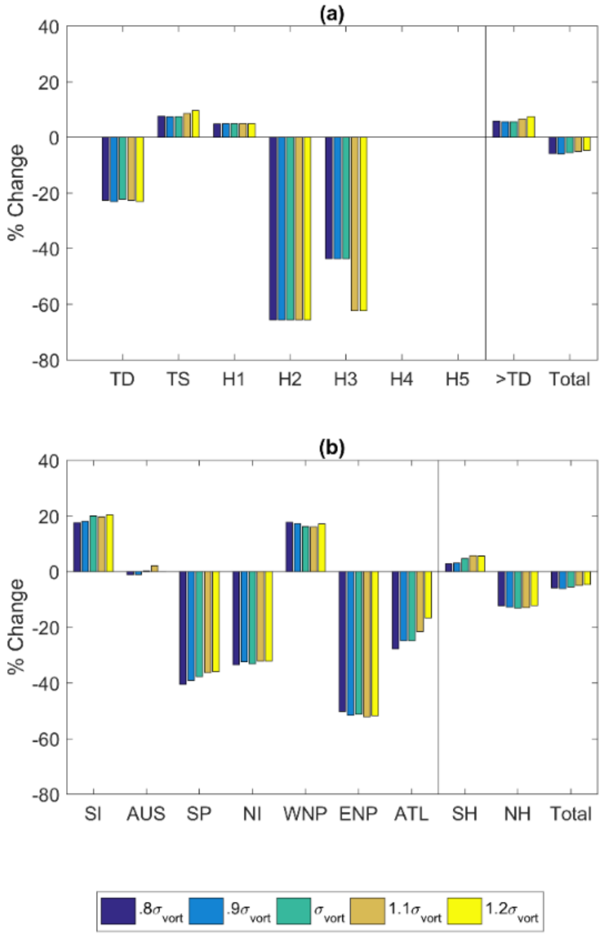

Figure 22 850 hPa relative vorticity threshold sensitivity test. Percentage change of number of storms generated in LGM and 20C simulations by (a) category and (b) basin. The middle bar of every group (teal), is using the control case threshold, while the other bars use a threshold multiplied by a factor (shown in the legend).

favor of 20C storms, particularly for TDs and TSs (at increases higher than control favors a slight increase in LGM H1 storms). In terms of basins (**Figure 21b**), the all except the Northern Indian Ocean show proportionally fewer storms at LGM, pushing the difference between LGM and 20C in a more negative direction, which is reflected in the total counts as well. The changes by category cannot be determined to be statistically significant, however the significance of many of the changes by basin follow those found in the control case.

Figure 22 is similar to **Figure 21** but shows sensitivity to the vorticity threshold. Making the threshold more restrictive produces small changes overall, however at its highest values creates a larger number of LGM TS and 20C H3 storms (the actual count is still rather small which yields a large percentage change). The basin changes generally favor a trend towards more positive change, however the number of storms ultimately still favors 20th century storms. Similarly to what we found for the sensitivity tests for the σ_{temp} threshold, the significance of the changes by basin follow those found in the control case.

Figure 23 is similar to the previous figures but shows sensitivity to the surface wind speed threshold. This is the minimum surface wind that must be met for a system to be classified and added to the dataset, and as noted earlier are typically ~11.48 m/s. These experiments show important sensitivity that differs from the ones examined above. As the threshold becomes more restrictive, the total number of storms generated between the two climates becomes similar ($1.1\sigma_{speed}$), and then reverses sign yielding a

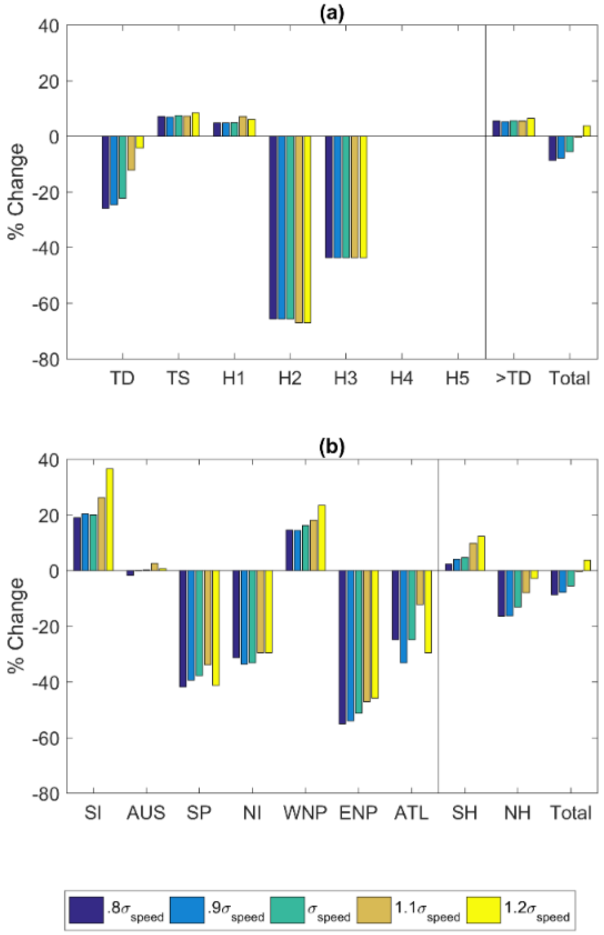

Figure 23 Surface wind speed threshold sensitivity test. Percentage change of number of storms generated in LGM and 20C simulations by (a) category and (b) basin. The middle bar of every group (teal), is using the control case threshold, while the other bars use a threshold multiplied by a factor (shown in the legend).

larger number of LGM storms overall (1.2σ_{speed}). This is an important sensitivity, as we find that increasing the wind speed threshold by only 20% alters the sign of the change in count with climate. This change arises owing to the larger number of 20C storms whose peak intensity is that of tropical depressions, and as fewer of these events are included in the dataset, the surviving subset of stronger systems are more numerous at

LGM. As discussed previously, using a more restrictive threshold for surface wind speed significantly decreases the number of weak storms. This trend is found in a majority of

Threshold	**Total σ(20C)**	**TD+ σ(20C)**	**Total σ(respective)**	**TD+ σ(respective)**
Control	0.14	0.33	**0.02**	0.46
$.8\sigma_{vort}$	0.12	0.40	**0.02**	0.49
$.9\sigma_{vort}$	0.11	0.36	**0.01**	0.55
$1.1\sigma_{vort}$	0.18	0.28	**0.02**	0.42
$1.2\sigma_{vort}$	0.22	0.22	**0.03**	0.37
$.8\sigma_{speed}$	**0.02**	0.33	**0.01**	0.33
$.9\sigma_{speed}$	**0.04**	0.33	**0.01**	0.36
$1.1\sigma_{speed}$	0.94	0.37	0.20	0.50
$1.2\sigma_{speed}$	0.41	0.21	0.35	0.41
$.8\sigma_{temp}$	0.25	0.29	**0.04**	0.42
$.9\sigma_{temp}$	0.26	0.30	**0.04**	0.42
$1.1\sigma_{temp}$	0.12	0.40	**0.02**	0.52
$1.2\sigma_{temp}$	0.12	0.42	**0.03**	0.53

Table 3 P-values generated from Welch's *t*-test using 20th century experiment thresholds (columns 1 and 2) and respective experiment thresholds (columns 3 and 4) for sensitivity tests. These tests were run for total counts and excluding tropical depressions. Bold values indicate statistically significant differences between the 20th century and LGM counts.

the basins, in both hemispheres, and in the global count. Additionally, we found the effects of using LGM defined thresholds for the LGM does not change the overall results.

In **Table 3** we again apply Welch's *t*-test to determine the statistical significance of the changes in counts for the various threshold testing runs generated using 20C thresholds for both simulations (columns 1 and 2) and the models respective thresholds in each (columns 3 and 4). Only two of the track sets (.8σ_{speed} and .9σ_{speed}) show a statistically significant difference in the total number of storms for the ~30 year period when applying the 20C threshold to both climates. Both of these sets produce more 20th century than LGM storms. However, when using each climate's respective thresholds, all but two of the sets (1.1σ_{speed} and 1.2σ_{speed}) produce statistically significant changes in the total counts between the two climates. Because the LGM generated thresholds are more restrictive than the 20C, the counts and the means of those counts decrease throughout the LGM, shifting the mean to being statistically significant for a majority of the runs. None of the sets that exclude tropical depressions can be designated as statistically different as the other. It should be noted that regardless of thresholds chosen, the number of 20C storms is greater than in LGM when examining total counts, while the opposite is true when excluding tropical depressions (a relatively greater number of LGM storms generated when looking at storms TS strength and greater). This being with one exception discussed previously (the 1.2σ_{speed} case that generated a larger number of total storms in LGM when using 20C thresholds)

These tests were run in order to emphasize that there is not a single universally agreed upon threshold for detection (Horn et al. 2014), and that even the sign of the change with climate can be reversed depending on user choices in the algorithm design. There is some arbitrariness in the definition of what defines a tropical cyclone within the model itself. The weakest events generated our quite sensitive to the choice of thresholds, and can change the climatology. Here we presented a scenario where the choice of thresholds yielded a change in the dominant simulation in respect to number of storms; while most show fewer storms at LGM, it is a plausible scenario. When vortex tracking algorithms were introduced (Manabe et al. 1970; Bengtsson et al. 1982), general circulation models were so coarse that even TS strength storms were not expected to be resolved. The goal however, was to search for systems that could possibly be a tropical storm. A number of models have high enough resolutions to explicitly resolve hurricane strength winds (Walsh et al. 2015), however their limitations become more apparent in lower resolution models.

We summarize the major findings of this section as follows:

1. Results are sensitive to the handling of weak systems
2. More weak events were detected in 20C than in LGM using the standard thresholds.
3. Making the σ_{speed} threshold tighter can reverse the sign of the LGM-20C difference by altering it as little as 20%.
4. Increasing σ_{temp} does the opposite, making it harder for LGM systems to pass.

The second point is particularly surprising in light of results from CMIP3 and CMIP5, that found more storms in 20C than in the warmer climate change experiments, and the handling of weak systems appears to be a major part of the difference (Emanuel et al. 2010). Here we also find a decrease in count at the LGM relative to 20C, with changes in the weakest storms being responsible for all of the difference. This raises a curious result, at least for CCSM4: there are more storms explicitly generated and tracked in 20C than in either the colder LGM or in the warmer anthropogenic experiments. We have also shown that there is sensitivity to threshold values in the detection algorithm in changes in storm count.

Latitude of Lifetime Maximum Intensity

In this final section of this chapter, we examine whether the location at which storms reach their highest intensity changes with climate. Kossin et al. (2014, 2016) have reported that the latitude at which storms reach their lifetime maximum intensity (Φ_{LMI}) has increased over the last several decades, and they note its consistency with other measures of a widening of the tropics. Korty et al. (2016) identified a significant poleward expansion of downscaled TCs in simulations of the much hotter Eocene-like climates, and here we test whether there is a consistent contraction in the explicitly simulated sets at LGM.

Tropical cyclones occur in regions of high potential intensity (*PI*), which are found where deep convection is possible. This condition is generally found throughout the tropics (Xu and Emanuel 1989), but abruptly terminates in the subtropics where the trade inversion is found. *PI* drops to a substantially lower value at the latitude of the trade inversion, and remains low in middle and higher latitudes. High values of *PI* can be found only at places and times that convection can reach the upper troposphere (Korty et al. 2012a). Kossin et al. (2014, 2016) has documented poleward shifts in the position of peak intensity for tropical storms in both observations and in projections of the coming century. This shift occurs concurrently with poleward expansions of other aspects of the tropics with warming, including the Hadley circulation (Hu and Fu 2007; Seidel and Randel 2007; Seidel et al. 2008; Adam et al. 2014) and subtropical dry zones (Mbengue and Schneider 2013). Korty and Emanuel (2007) and Zamora et al. (2016) also showed that convectively neutral lapse rates become common at higher latitudes of significantly warmer climate simulations.

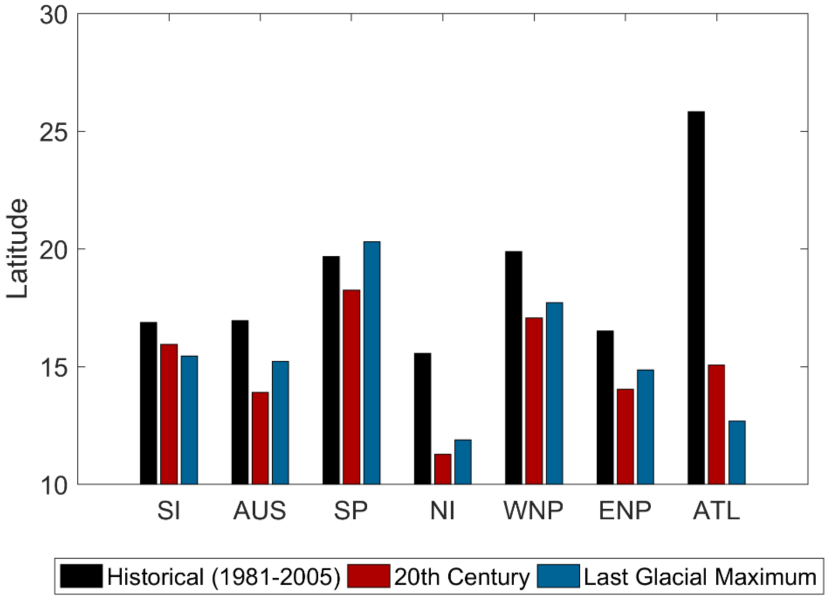

Figure 24 Average latitude of lifetime maximum intensity Φ_{LMI} by basin for historical (black), 20th century (red), and Last Glacial Maximum (blue) storms.

Here we examine whether the colder LGM simulation shows an equatorial contraction in the latitude of peak intensity consistent with the expansion that Kossin et al. (2014, 2016) found in warming climates. **Figure 24** shows the average latitude of lifetime maximum intensity by basin. Many of the changes in Φ_{LMI} are small and have large interannual variance, rendering most differences statistically insignificant. Differences in Φ_{LMI} are statistically significant only in the Australian basin and in summing all Northern Hemisphere storms, but in both cases the Φ_{LMI} is higher at LGM than in 20th century. (All significance tests are performed using Welch's *t*-test.) We note

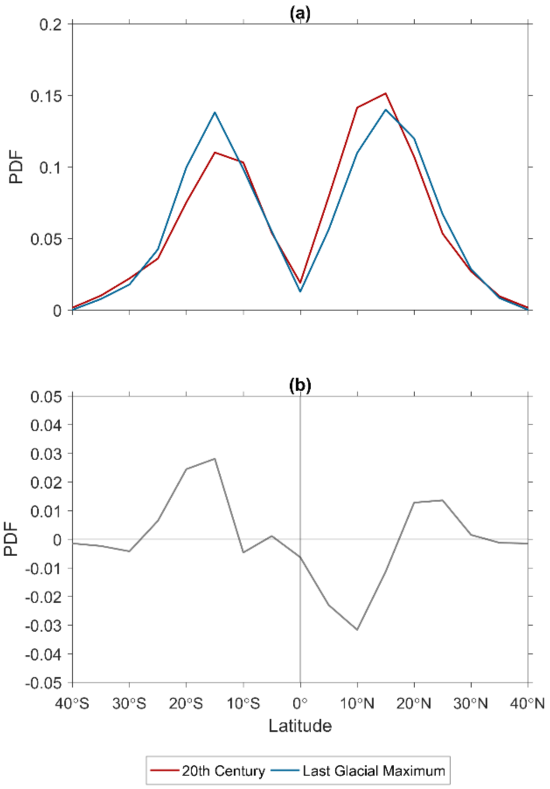

Figure 25 (a) Probability distribution by latitude of Φ_{LMI} in 20th century (red) and Last Glacial Maximum (blue) experiments. (b) LGM-20C difference of the probability distribution of Φ_{LMI} shown in (a).

that while many of the basin differences are insignificant, Φ_{LMI} in the LGM is nevertheless more often found poleward of the 20th century distribution.

Figure 25a shows the probability distribution function (PDF) of Φ_{LMI} for 20th century and LGM experiments. The data are interpolated into 5° equally spaced bins to eliminate noise. The two experiments have similar distributions of Φ_{LMI}, with the most frequent latitude of storms reaching max intensity occurring ~15° in both hemispheres. **Figure 25b** shows the differences between the two curves in **Figure 25a**: there is a small poleward shift in LGM Φ_{LMI} in both hemispheres. A greater number of LGM storms reach their maximum intensity in the 30°S-10°S band, and less equatorward and poleward of this region. Likewise, more 20th century storms are favored to reach max intensity near the equator, while favoring LGM storms at latitudes greater than ~15°N. This response is not consistent with the shift reported in Kossin et al. (2016), but the differences here are largely insignificant. We will revisit this issue in Chapter V when examining results of the Emanuel downscaling method on the LGM simulations.

In the next Chapter, we explore how the large-scale environmental factors differed at LGM, and compare them with the properties of the tropical cyclone climatology reported here.

CHAPTER IV

LAST GLACIAL MAXIMUM – ENVIRONMENTAL CONDITIONS

In the last Chapter, we examined the climatology of TCs in CCSM4's 20th century and LGM experiments. We found that while the global frequency was lower at LGM, this decrease came primarily from a decrease in the number of weak systems tracked (e.g., see **Figure 18**), and that the change was reversed if the detection algorithm's thresholds were tightened (i.e., there were more LGM than 20th century events using tighter surface wind criteria for detection). Cumulative metrics like *ACE* that depend on frequency and intensity showed that the LGM featured less activity in the eastern North Pacific, South Pacific, and northern Indian Oceans, but more activity in the western North Pacific and southern Indian Ocean (e.g., see **Figure 17**). In this Chapter, we examine how environmental conditions necessary for TCs changed between the two climates in CCSM4, and compare the spatial changes to the explicitly resolved systems discussed in Chapter III.

Sea Surface Temperature and Potential Intensity

Early composites of global observations showed that TCs routinely form only in regions of the warm with *SST* > 26°C (Gray 1968). The development of *PI* theory in the 1980s showed that TCs were possible only in regions where thermodynamic soundings support deep convection, which is coincident with the region of highest *SSTs*, but that the actual *SST* correlated with such a boundary would differ in other climates (Emanuel 1987). Indeed Korty et al. (2012a) confirmed that regions of LGM simulations with *SST*

> 24°C featured ranges of *PI* similar to those found over warmer waters in the 20th century.

Figure 26 shows the storm season mean (which we define as July-October for the Northern Hemisphere and January-April in the Southern Hemisphere) sea surface temperature (*SST*) for 20th century and Last Glacial Maximum simulations, respectively; genesis locations of vortices are overlaid (gray shaded circles). While temperatures are lower globally (~3°C cooler in the tropics and ~5°C cooler in the global average), the

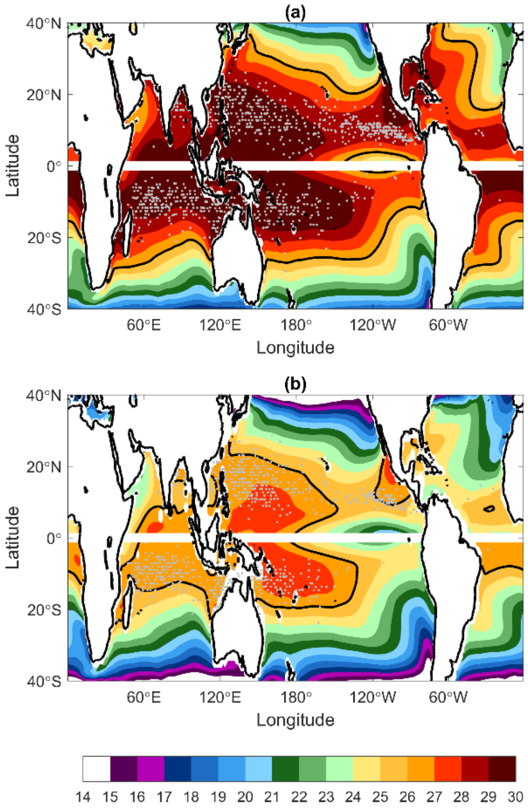

Figure 26 Storm season mean (July-October in the Northern Hemisphere and January-April in the Southern Hemisphere) sea surface temperature *SST* for (a) 20th century and (b) Last Glacial Maximum. Values shown are in °C. Shaded circles (gray) denote genesis locations. Black contour denotes the 26°C isotherm.

gradient of temperature within the tropics is very similar between the two climates. Average tropical *SSTs* (taken from the 30°S – 30°N band) are 26.31°C and 23.40°C in 20th century and LGM climates, respectively. Note that storms are produced in largely the same areas even though $SST < 26$°C through the eastern North Pacific at LGM, confirming that the absolute value of *SST* does not control the model's ability to produce TCs. Storms remain possible here because the vertical temperature profiles that support deep convection, and potential intensity remains high.

Potential intensity (*PI*) is the thermodynamic upper bound on the intensity of tropical cyclones. To put it more simply, it is the speed limit for a tropical cyclones maximum surface wind speed. Tropical cyclones require a flux of enthalpy k (heat) from the ocean to the atmosphere, and a marine boundary layer heated by this heat transfer becomes buoyant against the environmental sounding and can rise via convection to the upper troposphere. Potential intensity is high in regions where convection can carry a heated boundary layer parcel to the tropopause (or even lower stratosphere) and low in regions where the sounding caps the ascent at shallow altitudes. The level of neutral buoyancy (*LNB*; the altitude at which a heated parcel becomes neutrally buoyant) of a parcel, therefore, is an important factor. The difference between the sea surface temperature and temperature at the *LNB* where outflow convection occurs (T_o) directly affects the value of *PI*:

$$PI = \sqrt{\frac{C_k}{C_d}\frac{SST - T_o}{T_o}(k_0^* - k)} \qquad \textbf{(1)}$$

Here C_k and C_d are the exchange coefficients for enthalpy and drag, respectively (the value of its ratio is ~1; see Bister and Emanuel 1998), k_0^* is the saturation enthalpy of the sea surface, and k is the atmospheric boundary layer enthalpy. Potential intensity is highest in regions where thermal soundings permit deep convection, which in our contemporary climate lies within regions generally equatorward of the position of the 26ºC isotherm. It is particularly important to note that the limiting factor for *PI* is most often the depth of the convective layer established by the sounding, not the underlying *SST*; thus, in different climates (such as the LGM), the correlation between *SST*

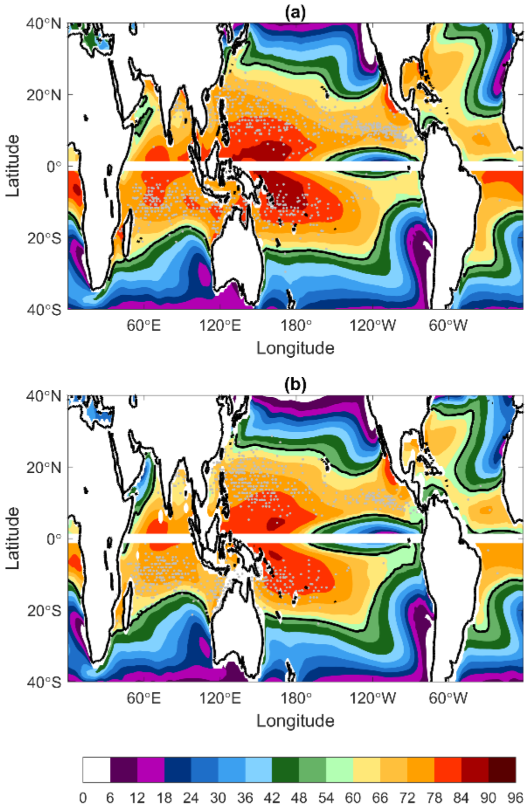

Figure 27 Storm season mean (July-October in the Northern Hemisphere and January-April in the Southern Hemisphere) potential intensity *PI*. Values shown are in m/s. Black line denotes the 55 m/s contour.

thresholds and high potential intensity occur at different values than in the modern world (see Korty et al. 2012a for further discussion).

Figure 27 shows the storm season mean potential intensity with genesis positions superimposed. The distribution of *PI* is much more similar between the two simulations than the *SST* shown in **Figure 26**, although the highest values of *PI* cover larger areas in 20th century simulation, and the low values are larger in middle latitudes of the 20th century than in LGM. Regions with climatologically high values of *PI* (> 55 m/s, which is correlated with *LNB* levels in the upper troposphere; see Korty et al. 2012b) are highly correlated with the genesis of individual storms in both climates. The largest values of *PI* are found in the western Pacific, while *PI* is much lower in the Atlantic basin when compared to those commonly found in the Pacific Ocean. The low *PI* values in the Atlantic are due to the cold *SST* bias in this basin, and is consistent with the significantly decrease in genesis of simulated storms. (A regional *SST* anomaly can produce a large *PI* anomaly if the temperatures aloft show smaller deviations. This is the rationale behind Vecchi and Soden's (2007) use of "relative *SST*" as a proxy for *PI*.)

Figure 28 shows the difference (LGM-20th century) in storm season mean *PI* values shown in **Figure 27**, with contours of storm season mean *SST* differences (LGM-20th century) overlaid. In this and subsequent difference plots, we adopt a uniform color scheme in which the warm colors (red, orange, and yellow) indicate regions that have more favorable values for TCs in the 20th century, while the cooler green, blue and purple colors indicate more favorable values for TCs in the LGM experiment. This plot shows that *PI* is larger in the 20th century experiment throughout much of the world, but

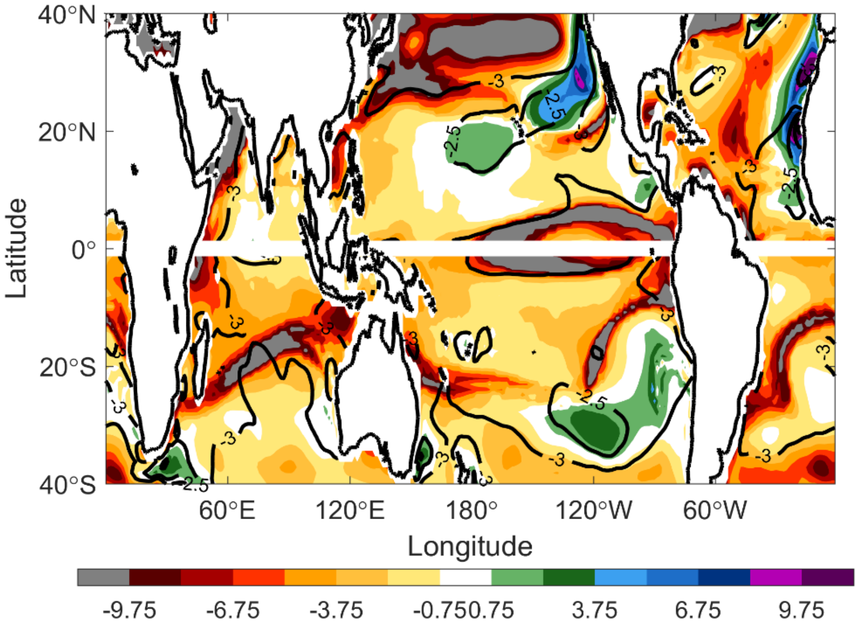

Figure 28 Difference in *PI* shown in **Figure 27**. Black contour indicates LGM-20C difference in 4-month storm season mean *SST*.

that parts of the central North Pacific show no change or more favorable values at LGM. Other regions with higher *PI* at LGM include the area off the western coast of the United States and of central South America, but these regions spawn few if any tropical cyclones in either climate, as despite the increase at LGM the values here are far below 55 m/s in each (see **Figure 27**).

An interesting aspect of **Figure 28** is the relationship between the degree of cooling and change in *PI*. Note that while all *SSTs* are 2-3°C cooler at LGM, regions that cooled more than the average of 2.9°C have the largest decreases in *PI* at LGM, while those that cooled less (such as the central North Pacific) saw *PI* rise. This shows that while the entire atmosphere and ocean surface cooled at LGM, where *SSTs* are relatively warmer at LGM (meaning surface cools less than average), *PI* is larger. This point was made by Korty et al. (2012a) and is similar to the arguments made by Vecchi and Soden (2007).

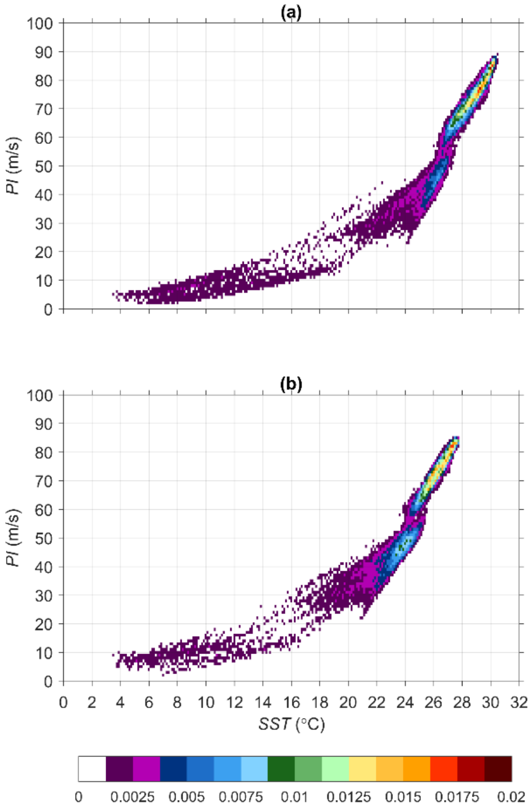

Figure 29 Normalized histograms of sea surface temperature and potential intensity for (a) 20th century and (b) Last Glacial Maximum experiments. Data is divided into 0.125°C (*SST*) and 1 m/s (*PI*) bins.

To further illustrate the point that the colder *SSTs* at LGM can still support large values of *PI*, **Figure 29** shows the joint distribution of *SST* and *PI* for 20th century and LGM experiments. The plot shows that to first order the range of *PI* values is similar in the two climates, but that the transition to large *PI* values occurs over colder temperatures at LGM than in 20th century. On closer inspection, the highest values of *PI* are slightly larger in 20th century than in LGM, which is consistent with the small increases in *PI* reported with warming from elevated CO_2 (Wing et al. 2015).

Lastly, we consider one other useful way to view the relationship between *SST* values and TC activity. Vecchi and Soden (2007), Swanson (2008), Vecchi et al. (2008), and Ramsay and Sobel (2011) have shown that locally warmer *SSTs* (relative to the tropical mean value) are strongly correlated with TC activity and high *PI*. Here we calculate relative sea surface temperature (*RSST*) by taking the difference between local *SST* and its monthly averaged value between the 30°S – 30°N band. Thus positive values

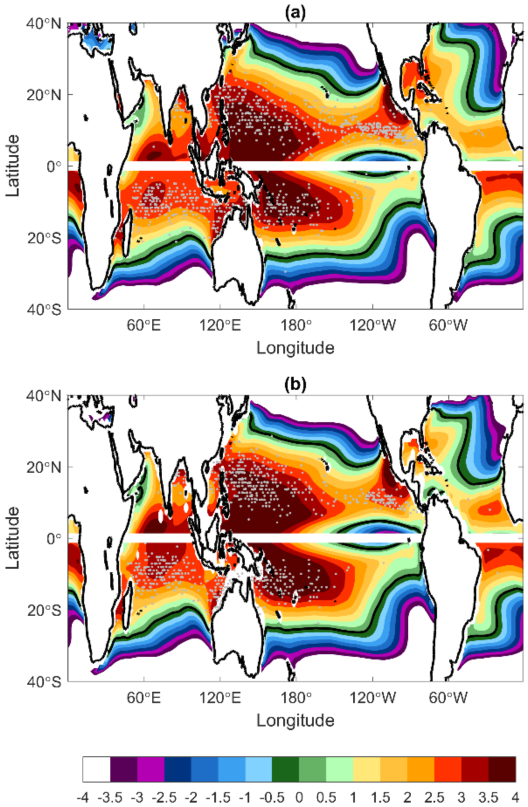

Figure 30 Storm season mean (July-October in the Northern Hemisphere and January-April in the Southern Hemisphere) relative sea surface temperature *RSST*. Values shown are in °C. Black contour denotes the contour where the storm season mean *SST* equals the tropical average *SST*.

of *RSST* indicate regions of anomalously warm tropical waters, while negative values show locally cooler conditions.

Figure 30 shows the storm season mean of *RSST* for 20th century and LGM experiments. The locations of storm genesis are concentrated where RSST is largest (2°C or more above tropical mean). **Figure 31** shows the difference in *RSST* between the LGM and 20th century experiments shown in **Figure 30**, along with a solid black contour outlining regions where the difference is 0. Overlaid on the figure are circles (o) to denote regions where the track density is higher at LGM, or crosses (x) to denote regions where the track density is larger in the 20th century. The size of the marker scales with the magnitude of the difference. *RSST* is larger at the LGM in many of the basins,

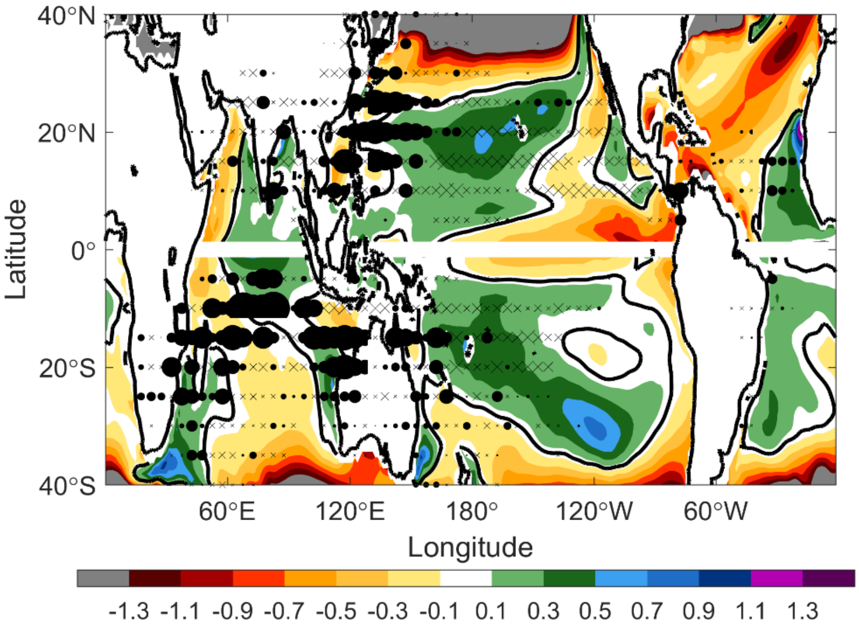

Figure 31 Difference in storm season mean *RSST* shown in **Figure 30**. Markers show the difference in track density normalized by year. The size of the marker scales with difference between LGM (o) and 20th century (x). The black contour marks the line of no change between the two climates.

especially between 60°E – 120°W. The Atlantic basin has larger *RSST* values in the 20th century, but track density in both climates was low in this basin. While **Figure 30** shows that TCs form only where *RSST* is largest in each climate, in general there is not a strong relationship between the smaller increases or decreases in its magnitude and changes in track density.

To summarize, *PI* at LGM is similar to its 20th century throughout the tropics, despite the universally colder temperatures. TCs formed in similar areas of both climates, and are co-located with regions offering the warmest water in their respective climate (highest *RSST*). Small changes in the magnitude of *RSST*, however, do not appear related to any differences in track density between the two climates.

Tropospheric Humidity and Moisture Content

Low-level convergence and high tropospheric humidity were among the characteristics that Gray (1968) identified in regions of TC genesis. Numerical experiments performed by Nolan and Rappin (2008) and Rappin et al. (2010) showed that the time needed for a TC to form was longer in warmer climates, as saturating a column through moist convection required stronger fluxes of moisture from the sea surface. While these increased in intensity with warming, their growth was approximately linear with temperature, while saturation deficits in the troposphere rose exponentially with the Clausius-Claperyon relation as relative humidity (*RH*) was approximately constant. In this section we look at differences in *RH* between CCSM4's LGM and 20th century climate, but also consider the thermodynamic resistance parameter that is a function of both moisture and temperature that Nolan and Rappin (2008) found to be relevant to storm formation times. This ratio of moist entropy deficits to surface fluxes of enthalpy is an important non-dimensional parameter (χ) and is defined:

$$\chi = \frac{s_m^* - s_m}{s_0^* - s_b} \qquad (2)$$

where *s* is moist entropy, the asterisk denotes values at saturation, and the subscripts *b*, *m*, and *0* are evaluated at the boundary layer, mid-troposphere, and surface, respectively. The moist entropy, *s*, as calculated following Emanuel (1994); it is defined:

$$s = c_p ln(T) - R_d ln(P) + \frac{L_v q}{T} - R_v q ln(H) \qquad (3)$$

where c_p is the heat capacity at constant pressure, *T* is temperature in kelvin, R_d is the gas constant for dry air, *P* is pressure in pascals, L_v is the specific latent heat of vaporization, *q* is specific humidity, R_v is the gas constant for water vapor, and *H* is the relative humidity. Entropy, or relatedly equivalent potential temperature, of a parcel determines its stability with respect to moist convection. Importantly, this quantity is a function not only of the actual humidity of a parcel, but its temperature (and pressure) too.

The numerator of **(2)** is the saturation deficit of the middle troposphere, which we evaluate using 600 hPa data. The denominator is proportional to the strength of the surface fluxes from the ocean to the atmosphere. Thus **(2)** gives a measure of the ratio of how much entropy is required to saturate the troposphere relative to the strength of the fluxes that supply it. In climates that differ from our own, this parameter is especially useful, as changes in moist entropy deficits are affected by temperature changes as well as changes to humidity. Simply put, χ is a measure of the moisture supply (denominator; strength of surface fluxes) and demand (numerator; saturation deficit). Thus, large values of χ are indicative of dry columns of mid-tropospheric air. The ratio between saturation deficit and strength of surface fluxes gives χ the property of being scaled with temperature. In cooler climates (such as the Last Glacial Maximum), the strength of the surface fluxes decrease, accompanied with a larger decrease in the saturation deficit in the numerator. If *RH* remains constant between climates, increasing the temperature will yield higher values of χ.

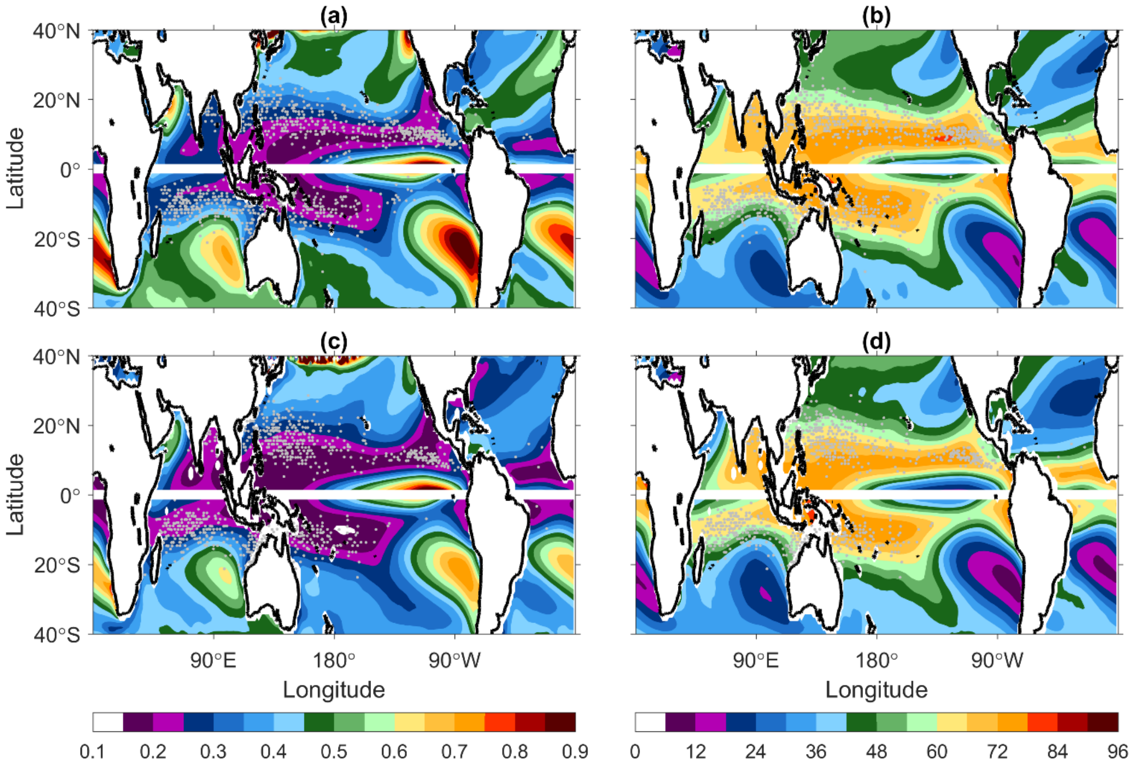

Figure 32 Storm season mean (July-October in the Northern Hemisphere and January-April in the Southern Hemisphere) thermodynamic resistance parameter χ for (a) 20th century and (c) LGM simulations. Values shown are unitless. (b, d) As in (a, c) but for relative humidity at 600 hPa RH_{600}. Values shown are in percent. Shaded circles (gray) denote storm season genesis locations.

Figure 32 shows the storm season mean of χ (left) and *RH* at 600 hPa (right) for 20th century and Last Glacial Maximum simulations, respectively. Generally, genesis occurs within regions with low values of χ (< 0.4) and high values of RH_{600} (> 50%). **Figure 33** shows the difference in storm season mean χ and RH_{600} between LGM and 20th century experiments shown in **Figure 32**. The two environmental variables generally show opposite trends: lower values of χ in the LGM experiment, but higher values of RH_{600} in the 20th century. As mentioned previously, values of χ are closely linked with temperature, and will generally yield lower values in cooler climates (if *RH* remains constant). The few areas that show relatively lower values of χ in the 20th century do not coincide with any appreciable genesis or track density. Similarly, while

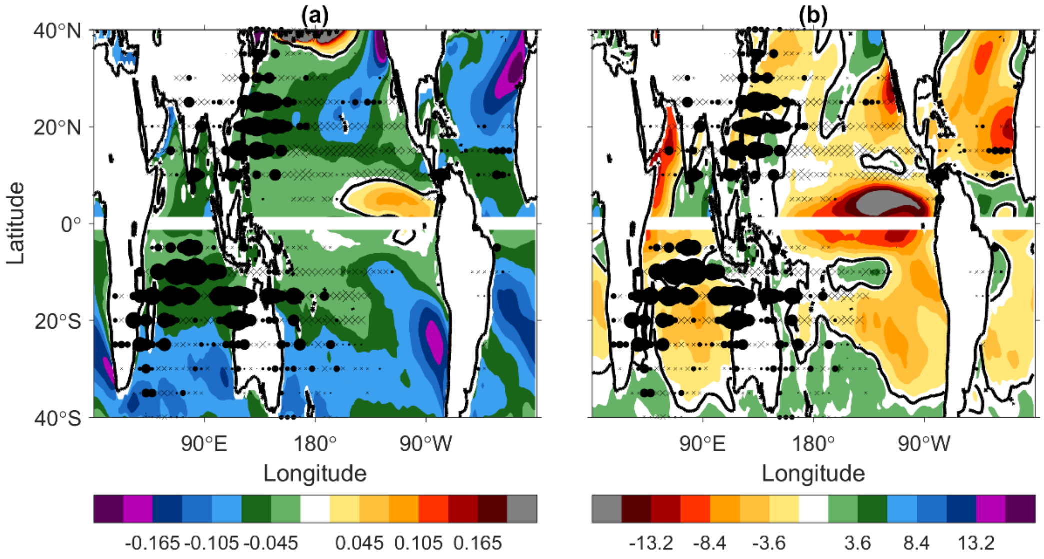

Figure 33 (a) Difference in storm season mean thermodynamic resistance parameter χ. (b) Difference in storm season mean relative humidity at 600 hPa RH_{600}. Markers show the difference in storm season track density normalized by year. The size of the marker scales with difference between LGM (o) and 20th century (x). The black contour marks the line of no change between the two

RH_{600} is generally favored in the 20th century, there exist many regions where values are higher in the LGM (particularly in the Southern Hemisphere extratropics, but also in the North Indian ocean, a tongue of lower values in the central/eastern North Pacific, and an area ~10°S in the central Southern Pacific).

Vertical Wind Shear

Large magnitudes of vertical wind shear discourage TC development and intensification partly because of their detrimental kinematic effects (DeMaria 1996) and also because it mixes environmental air into the storm's core (Tang and Emanuel 2010). Compared with the saturated air within the core of a TC, the ambient environmental air surrounding the storm is drier. Thus, in the presence of shear, dry air can be entrained into the mid-levels of a TC's core, requiring still stronger fluxes of moisture from the ocean to supply sufficient moisture to overcome the newly larger deficit. However, it is important to note that in particular limited cases, certain wind shear arrangements can actually be beneficial to development. Nieto Ferreira and Schubert (1999) showed that when a tropical upper tropospheric trough exists to the east of a tropical cyclone, the upper level divergence necessary for storm strengthening can be enhanced (Ferreira and Schubert 1999). Here we consider large-scale measures of tropospheric wind shear, which is nearly always detrimental to development, and follow the common practice in the literature of examining the magnitude of a deep layer (850-250 hPa here) vertical wind shear vector.

While wind shear can have a relatively high sensitivity to regional and temporal variations in individual storms, climatological averaged values in the tropics are generally smaller in magnitude than at higher latitudes, where horizontal temperature gradients are larger. In the absence of vertical wind shear, the gestation period in numerical simulations shortened as the surface warms and surface fluxes increased (Nolan et al. 2007). But with any non-zero vertical wind shear present, the opposite occurred (developing TCs took longer to moisten the troposphere in the warmer climates; Nolan and Rappin 2008; Rappin et al. 2010). This has been argued as one of

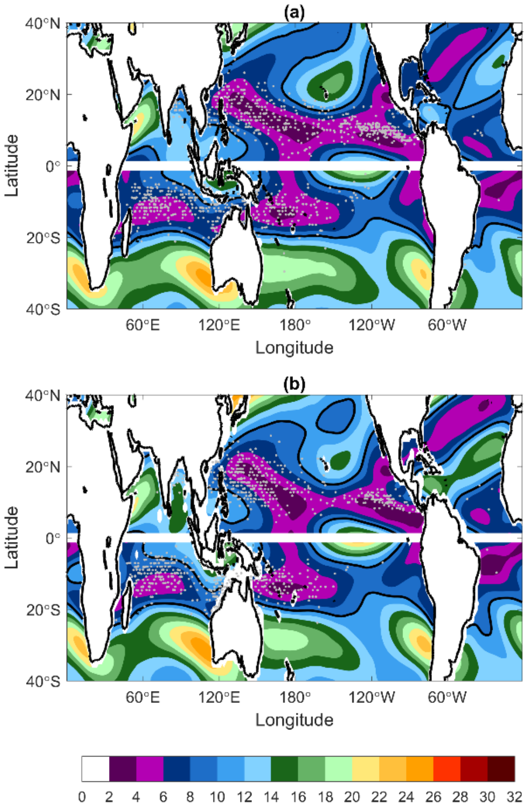

Figure 34 Storm season mean (July-October in the Northern Hemisphere and January-April in the Southern Hemisphere) vertical wind shear V_{shear}. Values shown are in m/s. Black contour denotes the 10 m/s isoline (somewhat arbitrarily chosen to separate regions of high/low shear).

the driving forces behind lower genesis rates in simulations of future warming (e.g., Emanuel et al. 2008).

Here we take the magnitude of the vertical wind shear (V_{shear}) as the vector difference between 850 and 250 hPa winds. **Figure 34** shows the storm season averaged vertical wind shear for 20th century and Last Glacial Maximum simulation. Regions of low wind shear in the 20th century are located throughout much of the Pacific Ocean within the 5°N – 15°N latitude band, with regions of high V_{shear} in the Indian Ocean and just west of North and South America. The distribution of LGM V_{shear} is comparable to that in 20th century, while having regionally higher or lower amplitudes.

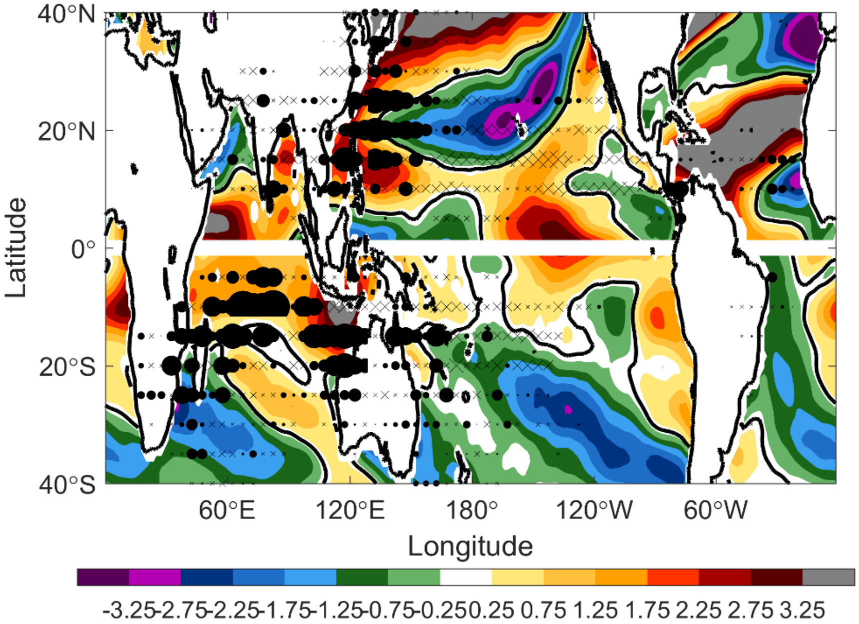

Figure 35 Difference in V_{shear} shown in **Figure 34**. Markers show the difference in track density normalized by year. The size of the marker scales with difference between LGM (o) and 20th century (x). The black contour marks the line of no change between the two climates. Values shown are in m/s.

Figure 35 shows the difference in wind shear between the two climates with track density difference markers as in **Figure 31**. The color scheme is flipped from the previous figure, so that the colors have consistent meaning: bluer (cooler) ones indicate regions of lower, more favorable shear at LGM, while red (warmer) ones indicate more favorable conditions (lower shear) in the 20th century. There are regional differences between the two climates, namely showing more favorable wind shear in the central Pacific during the LGM. However, many of the differences in track density do not directly relate to the local changes in vertical wind shear. Many of the regions in the Indian Ocean, where LGM track density is much larger than in 20th century, occur in the presence of stronger vertical wind shear.

Ventilation Index

Of course the environmental conditions examined in the last section do not operate in isolation, and an increase in vertical wind shear might be offset by an increase in atmospheric humidity levels. In an effort to represent the combined effects that these parameters have, Tang and Emanuel (2010, 2012) showed that a non-dimensional parameter called the ventilation index (Λ) that combines the thermodynamic properties of PI and χ with measures of wind shear successfully predicted changes in TC activity (Tang and Emanuel 2012a,b; Tang and Camargo 2014). This index is the same parameter that Nolan and Rappin (2008) and Rappin et al. (2010) identified as useful in describing the time needed for a TC to organize.

Higher values of the ventilation index indicate regions containing either high vertical wind shear, a shortage of ambient tropospheric moisture, low potential intensity, or some combination of all three. It is a metric that assesses the effects of the influx of dry air into a disturbance on the genesis and development into a tropical cyclone. Larger values of Λ increase the difficulty and length of time an initial vortex takes in developing into a tropical storm (if it is even able to). The parameter is defined by:

$$\boldsymbol{\Lambda} = \frac{\boldsymbol{V_{shear}\chi}}{\boldsymbol{PI}} \tag{4}$$

where individual variables are as defined in earlier section. Similar to the discussion of χ, this ratio can easily be explained as a ratio of the supply and demand of a tropical cyclone. Substituting the definition of χ from **(2)**, the numerator of **(4)** describes the flux of dry air entrainment by shear, while the denominator is related to the strength of the surface fluxes that supply the fuel for a storm (Tang and Emanuel 2012). Thus **(4)** is a normalized measure of vertical wind shear that incorporates important measures of the thermodynamic environment that occur concurrently but may evolve independently from the shear.

Figure 36 shows the logarithm of ventilation index. (We plot the value $\log_{10}\Lambda$ over the range of values from -2 to 0, as the actual values of **(4)** are generally too small to see clearly.) Regions where $\log_{10}\Lambda$ is most negative indicate regions most favorable for TCs, as these occur when V_{shear} is low, PI is high, and χ is small. There appears to be correspondence of the most favorable regions with genesis locations. The black contour line denotes the regions where the ratio of denominator of **(4)** to its numerator is 10%,

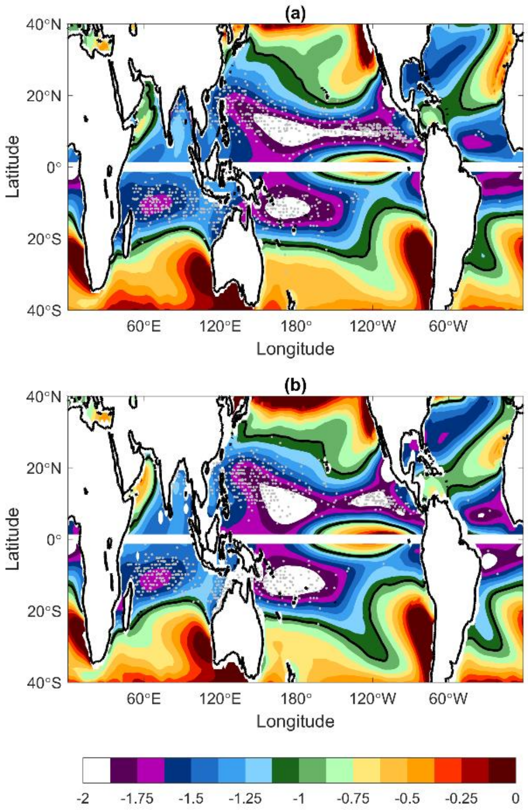

Figure 36 Storm season mean (July-October in the Northern Hemisphere and January-April in the Southern Hemisphere) logarithm of ventilation index $\log_{10}\Lambda$. Black contour denotes the -1 isoline (where the ratio of “anti-fuel” to “fuel” terms is 10%).

while the most negative values of $\log_{10}\Lambda$ indicate regions where the ratio of the terms is 1%. Each of the basins where the simulated storms generate (and where we expect genesis to occur in current climate) feature low values of Λ, although higher (less favorable) values are found in the North Indian Ocean when compared to the other basins. In addition, regions with the most favorable values of Λ are where genesis occurs, with the exception of the Atlantic basin near the United States (for reasons related to the cold Atlantic bias mentioned previously), and near the equator (where storms do not form).

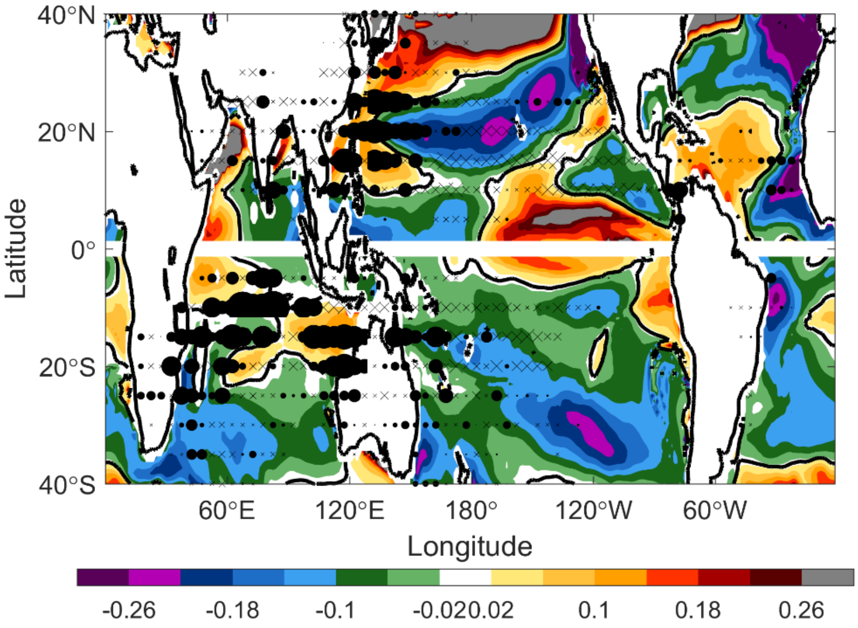

Figure 37 Difference in $\log_{10}\Lambda$ shown in **Figure 36**. Markers show the difference in track density normalized by year. The size of the marker scales with difference between LGM (o) and 20th century (x). The black contour marks the line of no change between the two climates.

Figure 37 shows the difference between storm season mean ventilation index (LGM-20th century) with differences in track density overlaid as before (circles show higher track density at LGM; crosses denote higher track density in 20th century). While *PI* was nearly everywhere (except central North Pacific) slightly lower at the LGM (**Figure 31**), and V_{shear} was in many places larger, these are offset by the colder temperatures that reduce the amount of water needed to reach saturation. Comparing **Figure 37** with **Figure 35** (showing differences in shear alone), the region of lower (more favorable) ventilation index is larger and covers wide swaths of the Pacific and Indian Oceans.

In much of the eastern North Pacific and Atlantic, conditions are less favorable at LGM, and there is generally less TC track density here and to the west. Moving west, conditions are more favorable at the LGM (lower V_{shear}, *SSTs* that are in a relative sense milder, and lower saturation deficits) across the central Pacific extending into the eastern portion of the western North Pacific basin. Track densities are higher on the western side of this area, possibly indicating an increase in storm activity that began under more favorable conditions to its east (Yoo et al. 2016).

In the Southern Hemisphere, conditions are in most places more favorable in the LGM. This can be explained by the χ term, which was significantly lower in LGM experiments (**Figure 32**), while the *PI* and V_{shear} terms featured generally a similar range of values (albeit with some regional differences). Further, there is some correspondence between the difference in track density with the difference in $\log_{10}\Lambda$ in the Southern Hemisphere in parts of the South Indian and Southwestern Pacific.

This Chapter has largely focused on qualitative comparisons of spatial changes in environmental factors and the TC climatology. We turn in the next Chapter to a downscaling method to simulate storms from global climate data. This will permit us to look at many questions that the vortices cannot (changes in intensity and their associated metrics of *ACE* and power dissipation).

CHAPTER V

LAST GLACIAL MAXIMUM – STATISTICALLY DOWNSCALED STORMS

In this Chapter, we apply a downscaling method developed by Emanuel et al. (2006, 2008) to the output of several global climate model's LGM and 20th century simulations. This method, which was reviewed in Chapter II, embeds random "seeds" in the tropospheric flow of GCMs. Along the tracks, which are determined by a beta-advection model using statistics of GCM's 850 and 250 hPa winds, the computationally efficient Coupled Hurricane Intensity Prediction System model (CHIPS; Emanuel et al. 2004) is run for each seed. The vast majority of these fail, but the seeds that intensify form a part of the event sets examined here. This method is continued until a preselected number of events (200 per year for each simulation are used here) are reached. The greater the number of seeds it takes to get 200 successful cases, the lower the annual frequency. We establish a separate calibration factor for each GCM so that all results in this chapter are normalized to produce an average of 80 events per year in the 20th century.

The advantage of this method is that it is computationally efficient at generating a very large number of events while also resolving the full range of possible intensities. The hurricane model is a later generation of the code first used by Rotunno and Emanuel (1987). It capitalizes on the computational efficiency of angular momentum coordinates, which give high resolution in the vicinity of the eyewall without resolving details in the periphery less important to the storm's intensity. The version used here incorporates the thermodynamic effects of wind shear through dry air entrainment into the storm's core (Tang and Emanuel 2010) and ocean mixing (Emanuel et al. 2004).

We complement the results of the previous chapters by applying this method to the same CCSM4 experiments, but also apply the method to the output of the LGM and 20th century simulations from MPI and MRI global models as well. (While we could examine vortices in Chapter III only for data saved at 6 hourly intervals or more, this method can be applied to the more commonly saved monthly means and variances, without need for data from each individual time step.) Our interest in these runs is not only on how the frequency, location, and times that storms form change, but also how the intensity distributions vary as well. We begin this chapter by examining the frequency and intensity changes in each of the three models, and continue with an assessment of how differences in the TC climatology relates to the changes in environmental factors.

Tropical Cyclone Frequency and Intensity Distribution

Table 4 and **Figure 38** show the frequency of TCs for each model in both its 20th century (control) and LGM climate simulations. The total number of cyclones is partitioned into the six intensity categories of the Saffir-Simpson Hurricane Wind Scale, with each storm's category determined by the maximum wind speed achieved at any point in the cyclone's lifespan. As noted above, the total number of cyclones in each model's 20th century experiment has been normalized to be 80 storms per year, the average number observed in the historical record from 1981-2005 (Shaevitz et al. 2014).

	CCSM4 20C	**CCSM4 LGM**	**MPI 20C**	**MPI LGM**	**MRI 20C**	**MRI LGM**
Tropical mean *SST* (°C)	26.44	23.54	25.35	22.92	25.53	22.91
Global mean *SST* (°C)	11.02	6.09	11.40	8.33	10.33	5.80
Annual Frequency	80.00	63.71 **(-20%)**	80.00	65.54 **(-18%)**	80.00	82.97 **(+4%)**
Number of TS	40.70	32.32 **(-21%)**	41.83	36.49 **(-13%)**	31.40	32.72 **(+4%)**
Number of H1	12.42	11.49 **(-8%)**	15.02	14.22 **(-5%)**	13.09	14.95 **(+14%)**
Number of H2	7.85	6.49 **(-17%)**	7.61	6.16 **(-19%)**	8.22	10.15 **(+23%)**
Number of H3	6.78	4.90 **(-28%)**	5.92	3.82 **(-35%)**	7.65	7.66 **(±0%)**
Number of H4	7.32	5.13 **(-30%)**	6.50	3.55 **(-45%)**	10.17	8.96 **(-12%)**
Number of H5	4.93	3.39 **(-31%)**	3.13	1.29 **(-59%)**	9.47	8.53 **(-10%)**
Global *PDI* (10^6 m^3/s^3)	12.39	9.53 **(-23%)**	10.50	7.08 **(-33%)**	18.96	18.61 **(-2%)**

Table 4 Downscaled Storms. Average number of 20th century and LGM sea surface temperatures *SST*, storm counts by intensity, and global power dissipation index *PDI*. Colored values indicate percentage change between 20th century and LGM storm counts. Blue colors indicate larger number of LGM generated storms, while red colors indicate larger number of 20th century generated storms.

We draw attention to two main points in the data in **Table 4**. First, all models

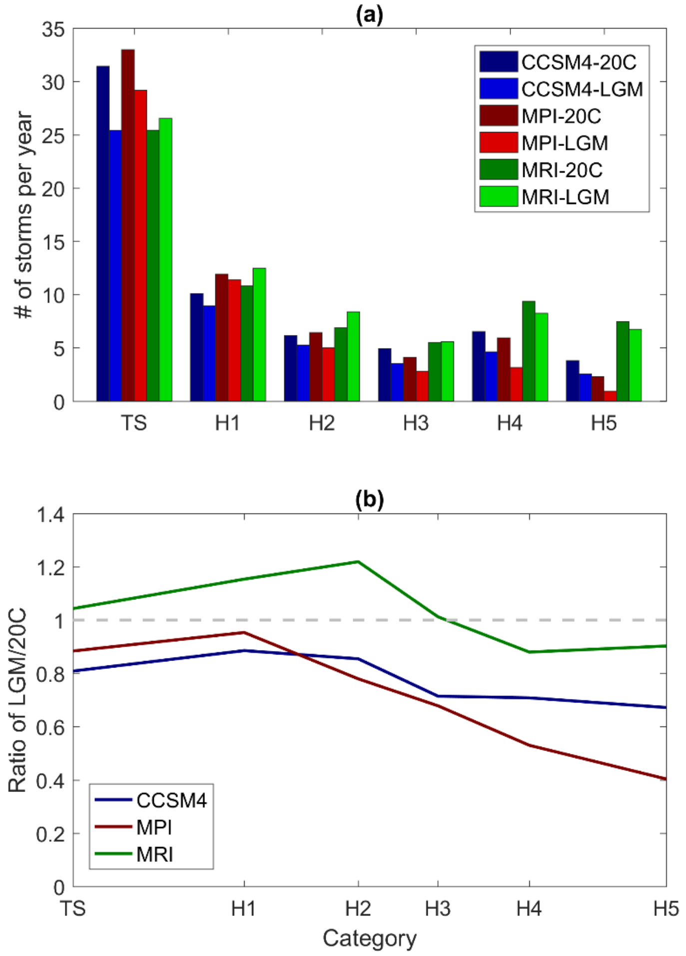

Figure 38 (a) Average number of storms per year by category for 20th century and LGM experiments for CCSM4 (blue), MPI (red), and MRI (green). Brighter colors indicate the LGM simulation for each model. (b) Ratio of Last Glacial Maximum to 20th century average number of storms per year by category.

yield fewer of the most severe events (H4, H5) in the colder LGM. This behavior is consistent with results from numerous studies and many different methods that show that the number of the most intense events increases with warming in projections of the 21st century (Walsh et al. 2016; Camargo and Wing 2016; Sobel et al. 2016). Second, the total number of cyclones is lower at LGM in CCSM4 and MPI, but MRI's LGM simulation supports more storms than its 20th century experiment does. The response of the total number of cyclones differs between models because of the number of weaker storms rises in MRI (it supports more TS, H1, and H2 storms at LGM than in the 20th

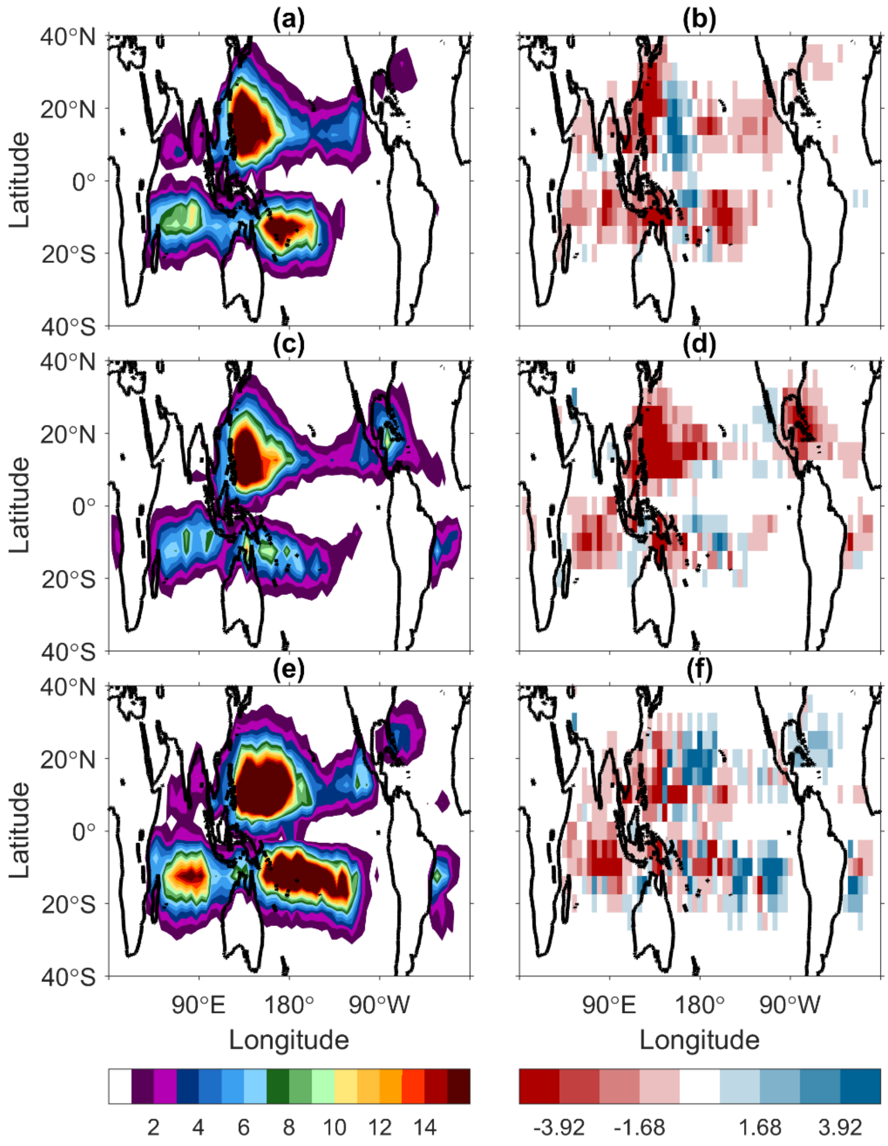

Figure 39 PDI densities for 20th century storms generated using Emanuel's downscaled storms technique for (a) CCSM4, (c) MPI, and (e) MRI models in 20th century simulations. (d-f) Difference (LGM-20C) in PDI density for the models in (a, c, e). Values are in 10^5 m^3/s^3 per 5° x 5° grid box.

century), while CCSM4 and MPI have fewer in all categories. We note that in contrast to the response of explicitly resolved systems (such as those presented in Chapter III), the Emanuel downscaling method has generally produced more storms in warmer climates (Emanuel et al. 2008, 2013; Fedorov et al. 2010), and so the decline in two of these three models is consistent with its behavior in downscaling simulations of warmer periods. We also note that the inconsistent changes in the total number of cyclones with climate have often been associated with different responses in the number of weak systems (Emanuel et al. 2010). This is true here too, both with the explicitly tracked systems in Chapter III, and the different downscaling response between MRI and the other models.

The decline in the number of the strongest events is important, as cumulative metrics of TC activity like *ACE* and *PDI* are weighted heavily by strong events. **Figure 39** shows the power dissipation index (defined in Chapter IV) for each model's 20th century run and the difference between *PDI* in its LGM simulation and it. Note that all three models produce the most *PDI* in the western North Pacific, with a second substantial source in the Southern Hemisphere from the Indian Ocean across Australia into the Southwest Pacific. The eastern North Pacific and Atlantic in general contribute less. Global power dissipation is lower at LGM in all three models (**Table 4**), but the right panels of **Figure 39** show places in each model that produce locally larger *PDI* at LGM (e.g., part of the western North Pacific in CCSM4, part of the central South Pacific in MPI, and the Atlantic and central Pacific in MRI).

Genesis, Tracks, and Annual Cycle

Figure 40 shows the spatial distribution of genesis density for 20th century simulations of each model (left panels), and the difference at LGM (right panels: red

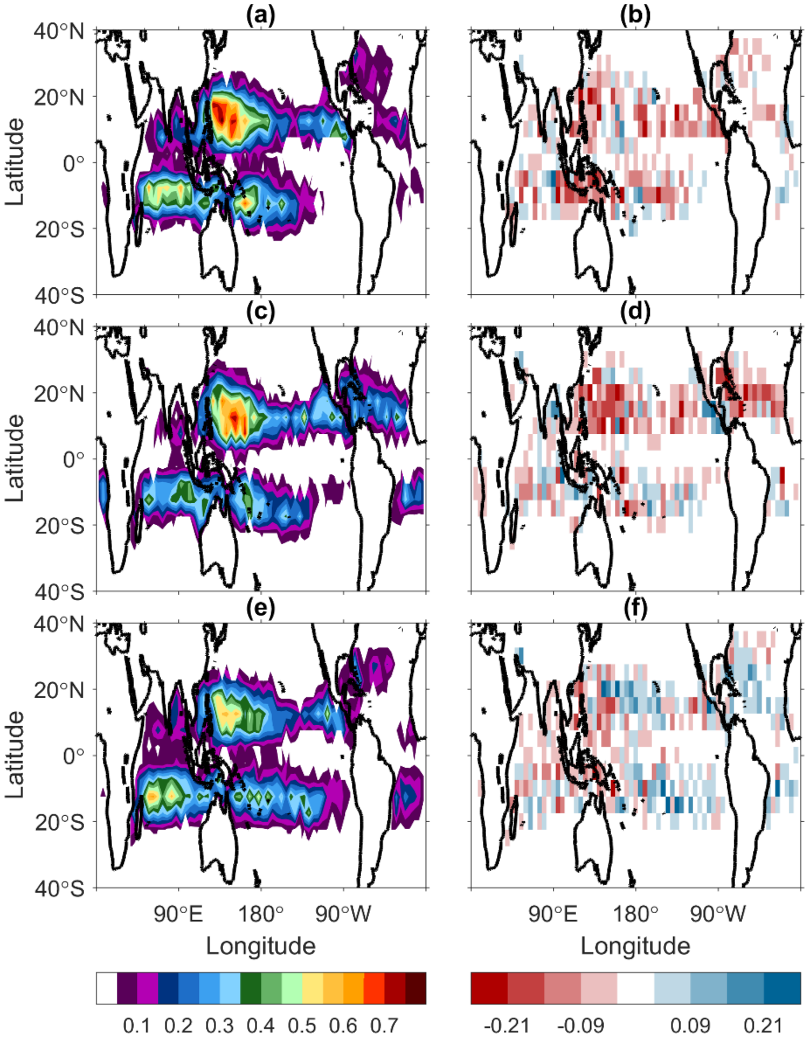

Figure 40 Genesis densities for 20th century storms generated using Emanuel's downscaled storms technique for (a) CCSM4, (c) MPI, and (e) MRI models in 20th century simulations. (d-f) Difference (LGM-20C) in genesis density for the models in (a, c, e). Values are in number of storms per year per 5° x 5° grid box.

colors indicate higher 20th century genesis density and blues indicate higher LGM genesis density at that point). Values were computed by counting the number of events per year for each 5° latitude by 5° longitude box. (Given that all storm counts have been normalized to 80 for the 20th century, the sum of all values in (a), (c), and (e) is 80.)

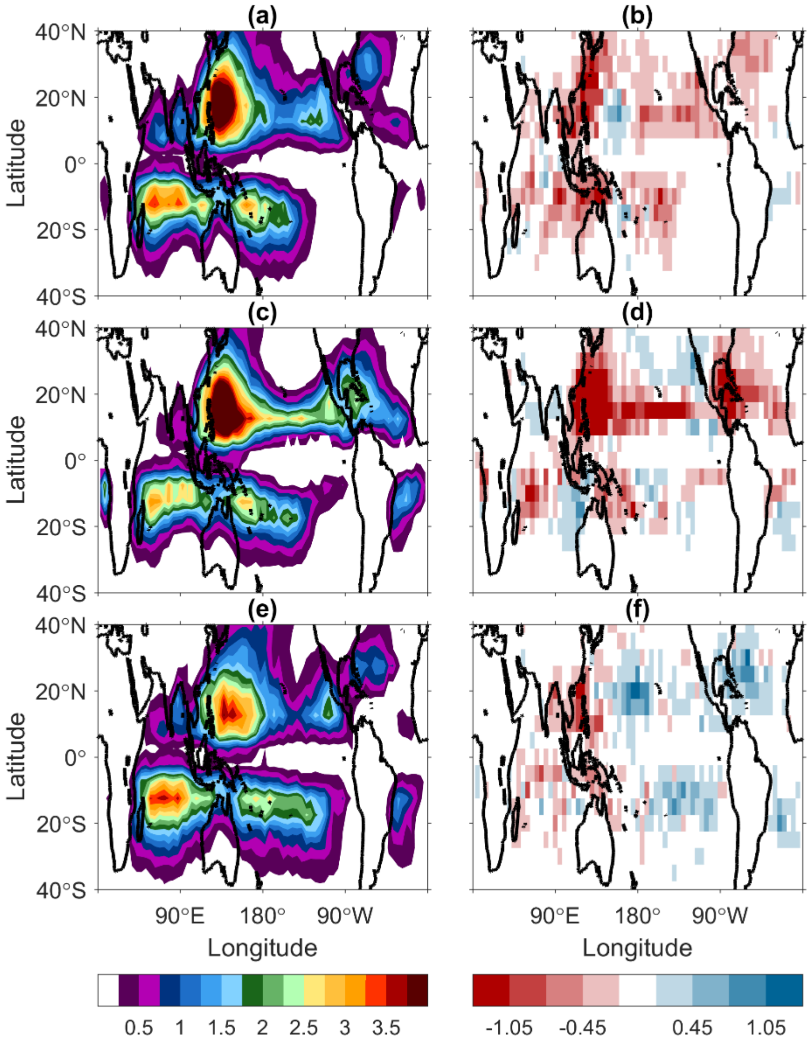

Figure 41 Track densities for 20th century storms generated using Emanuel's downscaled storms technique for (a) CCSM4, (c) MPI, and (e) MRI models in 20th century simulations. (d-f) Difference (LGM-20C) in track density for the models in (a, c, e). Values are in number of storm days per year per 5° x 5° grid box.

Likewise, **Figure 41** shows the track densities in the 20th century (left) and the differences at LGM (right).

The difference among the models in their change in total number of cyclones at LGM reported in Table 4, is apparent from both of these figures: right panels of CCSM4 and MPI are dominated by red, showing more genesis and track density in the 20th

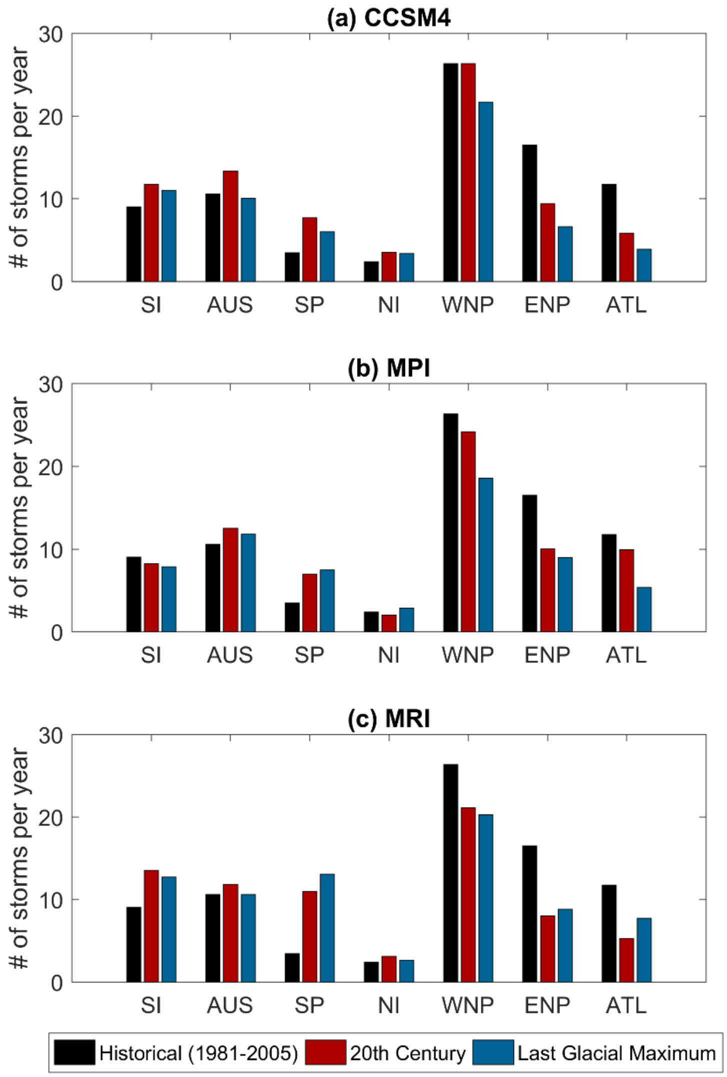

Figure 42 Distribution of genesis by basin for Historical (1981-2005) storms, and downscaled storms from 20th century and Last Glacial Maximum (a) CCSM4, (b) MPI, and (c) MRI models.

century, while much of the Western Hemisphere in MRI is dominated by blue (showing more LGM activity). As with the PDI examined earlier, there are local regions in each model that have higher LGM genesis and track densities. Note that subtropical and middle latitudes of the North Pacific have lower track density at LGM in the CCSM4, but higher track density at LGM in MPI. The Atlantic features higher track density at LGM in MRI, but lower in the other two models.

Figure 42 shows the number of storms by basin for each model's two climate experiments along with the historical record. All three models overestimate the number of Southern Hemisphere storms and underestimate the number of Northern Hemisphere storms (compared to the historical record). In addition, the models tend to produce a larger amount of activity close to the equator than is observed in nature, especially in the Southern Hemisphere. This was also seen in the explicitly resolved cases studied in Chapter III. CCSM4 and MPI feature less activity in nearly every basin at LGM, while MRI shows increases in LGM activity in the eastern North Pacific, Atlantic, and South Pacific. Relationships between these particular model differences and local environmental conditions will be examined in the sections that follow.

Figure 43 shows the distribution of genesis by latitudes in each of the 6 experiments. MRI produces storms farther poleward in the Southern Hemisphere than does CCSM4 or MPI, and CCSM4 has higher genesis densities at deep tropical latitudes than MPI or MRI in both hemispheres. The LGM (dashed) spawns fewer storms on the poleward side of the peak of the distribution in the Northern Hemisphere for CCSM4 and MPI, while MRI activity at LGM spreads farther poleward in both hemispheres. We

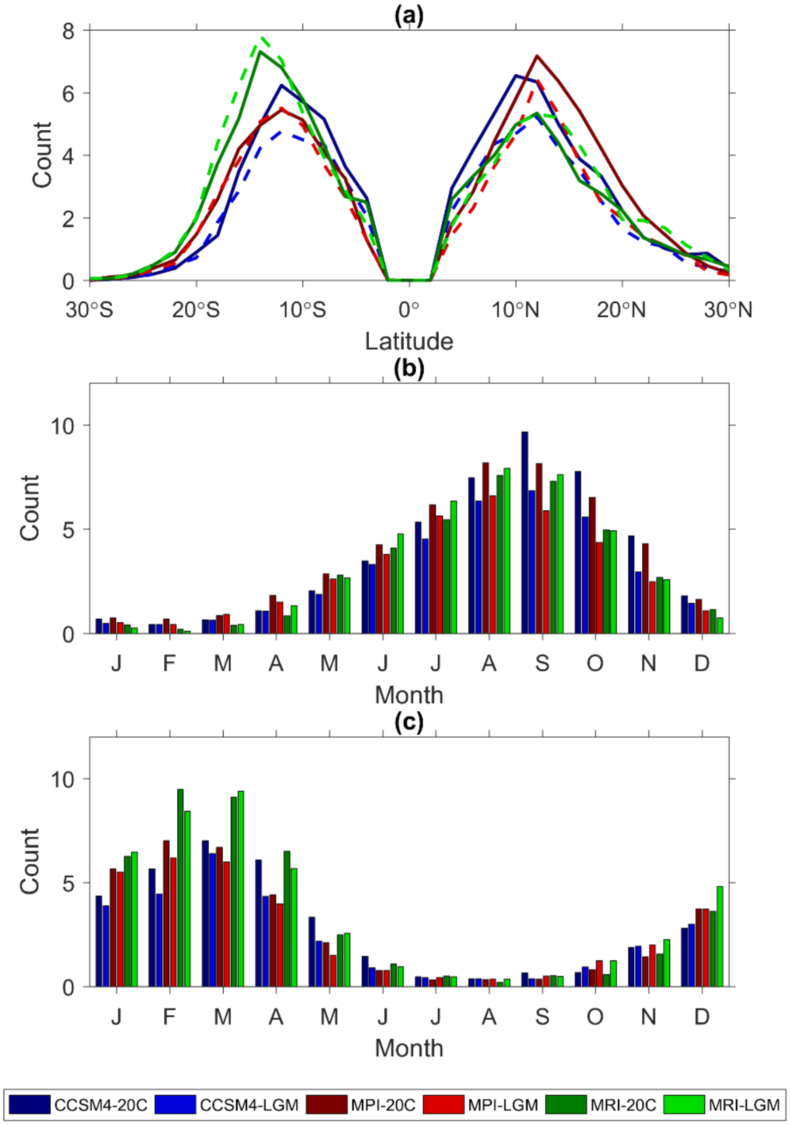

Figure 43 (a) Distribution of genesis by latitude for downscaled storms in CCSM4 (blue), MPI (red), and MRI (green) for 20th century (solid) and Last Glacial Maximum (dashed) simulations. Distribution of genesis by month for (b) Northern and (c) Southern Hemispheres. Brighter colors indicate the LGM simulation for each model.

will return to this issue below when we examine the statistics of the latitude of maximum intensity.

Figure 43b and c show the annual cycle of activity for the Northern and Southern Hemispheres, respectively. July to October in the Northern Hemisphere and January to April in the Southern Hemisphere are the four most active months for each model of both the 20th century and LGM. Given the similarity of the annual cycles in all models and in both climates, we use these months to define the storm seasons for their respective hemisphere. In the next section, we examine how the changes noted here relate to each model's changes in large-scale environmental conditions.

Thermodynamic Environmental Conditions

In the last Chapter we looked at the environmental properties of CCSM4, and in this Chapter we expand this to MPI and MRI. Note that while all three models were forced using the same external parameters (CO_2 reduced to 185 ppm at LGM; the same continental ice sheets; see Chapter II for additional details), they are separate coupled models and their response to these conditions has some regional variations that are important to the response of TCs downscaled here.

Figure 44 shows the highest *SST* achieved in any month of the year for the 20th century of each model (left panels) and the change in *SST* at LGM (red colors again indicate that 20th century values are warmer). Note that cooling is fairly uniform across tropical latitudes of each of the models, but that the degree of cooling is larger in CCSM4 and MRI (approximately -3°C) than in MPI (closer to -2°C). All three models produce qualitatively similar cooling to what proxies of temperatures from the period

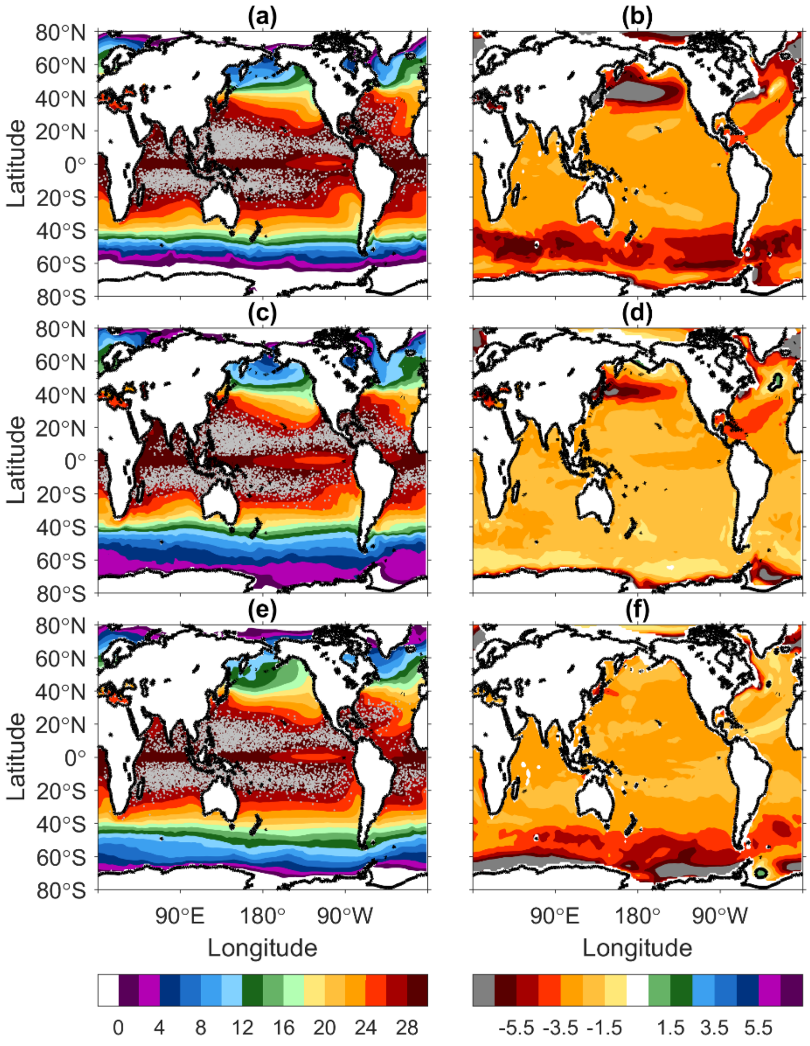

Figure 44 Annual peak sea surface temperature SST in (a) CCSM4, (c) MPI, and (e) MRI 20th century climates overlaid with genesis locations (gray shaded circles). Difference in SST (LGM-20C) for (b) CCSM4, (d) MPI, and (f) MRI models. Black line denotes locations where SST is equal between the two climates. Values shown are in °C.

suggest, but differences in climate sensitivity, ocean circulation strength or other internal model dynamics yield slightly different quantitative values for the same forcing.

Importantly, middle latitudes of the North Pacific LGM show significantly lower peak *SST* in CCSM4 than in either of the other models, showing that the summer northward migration of warm waters is sharply curtailed in LGM. A similar structure but smaller magnitude is present in MPI, while MRI shows no such change. Also relevant is that the Atlantic cools more than the remainder of the tropics in CCSM4 and MPI, but less than the remainder of the tropics in MRI. These responses are likely attributable to

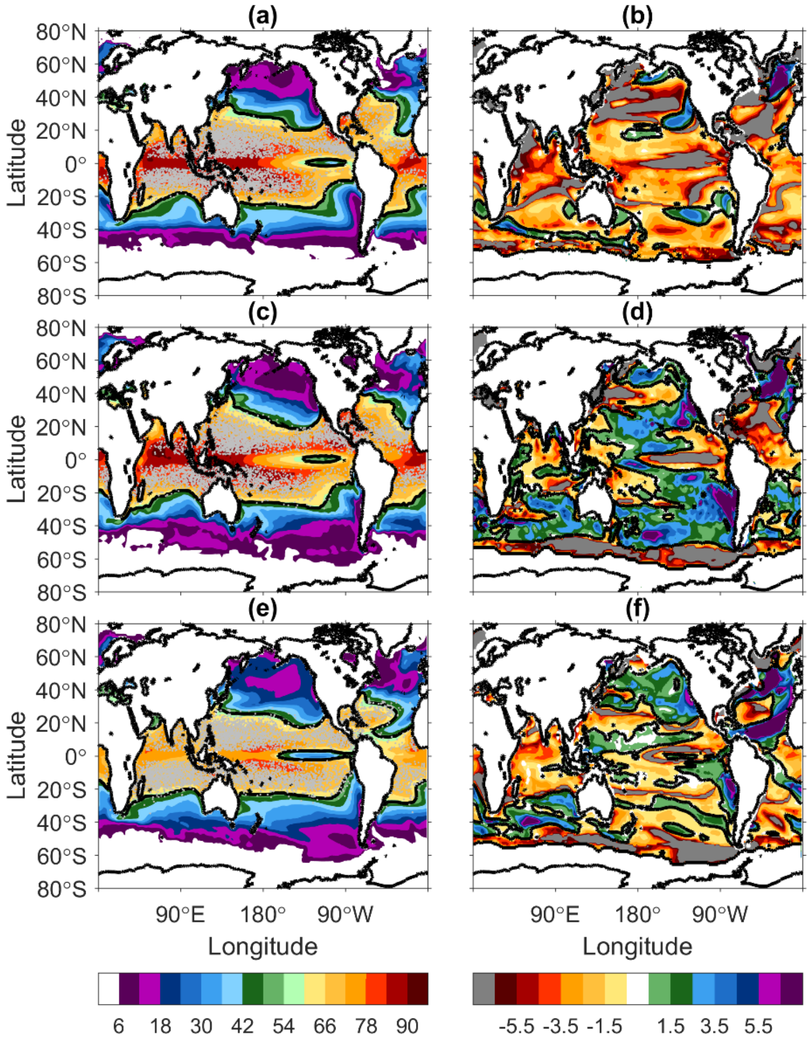

Figure 45 Annual peak potential intensity *PI* in (a) CCSM4, (c) MPI, and (e) MRI 20th century climates overlaid with genesis locations (gray shaded circles). Black line denotes the 55 m/s *PI* contour. Difference in *PI* (LGM-20C) for (b) CCSM4, (d) MPI, and (f) MRI models. Black line denotes locations where *PI* is equal between the two climates. Values shown are in m/s.

model differences in the Atlantic circulation, although an investigation of the origin of these differences lies beyond the scope of this thesis.

We calculated the potential intensity (*PI*) for each of the three models using the Bister and Emanuel (2002) algorithm discussed in the last Chapter. **Figure 45** shows the highest value of *PI* achieved during the year in the 20th century along with the points of origin for the downscaled events (left column). Note that essentially all genesis points fall equatorward of the 55 m/s contour, which Korty et al. (2012a) showed to be correlated with the boundary of the area in which deep tropospheric convection occurs.

Differences at LGM are show in the right panels of **Figure 45**. Despite the universally lower *SSTs* seen in **Figure 44**, there are some regions in each model with locally higher PI values. CCSM4 shows generally lower *PI* at LGM across the tropics, with substantially lower peak values in the Atlantic and subtropics and middle latitudes of the Pacific (consistent with the stronger cooling seen in these locations). MPI shows higher *PI* at LGM across much of the central Pacific, but lower *PI* at LGM in the Atlantic (where conditions cooled more than average) and in the far western North Pacific and Indian Oceans. The region near Australia also shows lower *PI* at LGM in MPI. MRI shows higher *PI* at LGM in much of the tropical Atlantic particularly along the swath from Africa to the Caribbean (as much as 20 m/s higher at LGM) where *SSTs* cooled by the smallest amount (see **Figure 44f**). Much of the tropical North Pacific has similar or slightly higher *PI* at LGM, although it is slightly lower in the Southern Hemisphere and substantially lower in the Indian Ocean.

A few points are worth bearing in mind: in all three models, *PI* remains large in the tropics at LGM (the magnitude of the changes discussed above are generally 1-5 m/s, while peak values are ~70-90 m/s). The spatial changes at LGM show some correspondence to the degree of cooling relative to other locations at the same latitude:

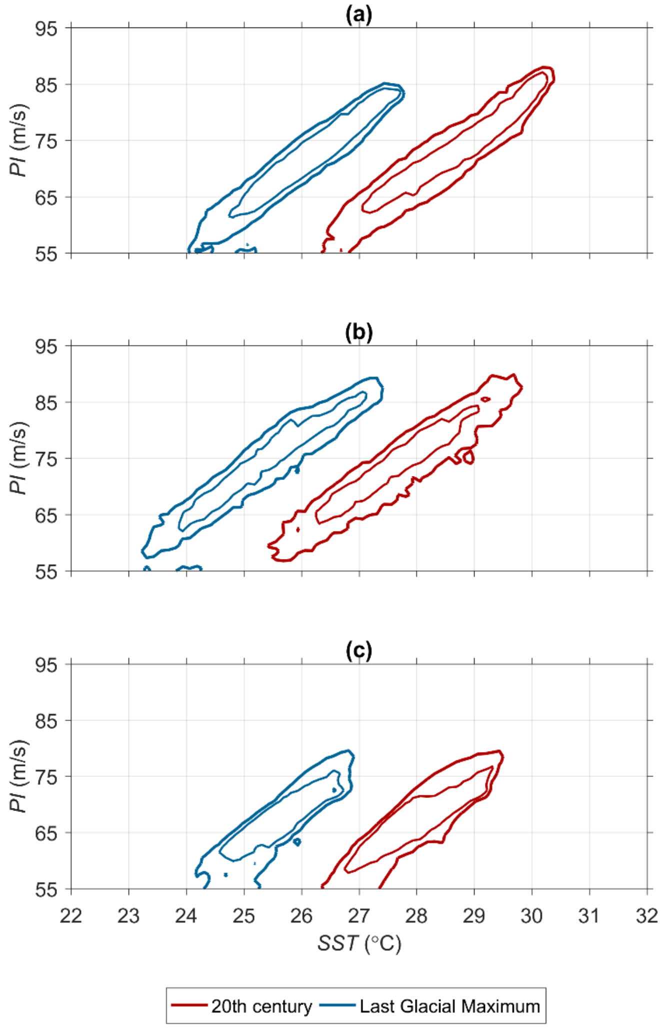

Figure 46 Bivariate joint distribution of potential intensity *PI* and sea surface temperature *SST* for 20th century (red) and Last Glacial Maximum (blue) simulations in (a) CCSM4, (b) MPI, and (c) MRI models. Thick line denotes the 0.0075 contour, while the thinner line denotes the 0.02 contour. Data is binned by 0.125 °C (*SST*) and 1 m/s (*PI*).

where cooling is larger than average, *PI* decreases, but where it was less (e.g., the Atlantic of MRI) *PI* rises despite the lower temperatures. This is consistent with the arguments Vecchi and Soden (2007) about relative *SST* being a first order proxy for PI values, and with the findings of Korty et al. (2012a) in an ensemble of LGM paleoclimate simulations. Because conditions in the tropical middle and upper troposphere are more homogeneous, coupling a locally warmer or cooler surface to it affects the local value of *PI*.

Figure 46 shows the joint distribution of *SST* and *PI* for the two climate experiments for each model. The major result is that similar ranges of *PI* can be found at LGM over colder *SSTs* than in 20th century. In CCSM4, there is also a slight decrease in *PI* values at LGM compared to 20th century, but this is a secondary effect.

Tropospheric Humidity Differences

High levels of tropospheric humidity reduce the time it takes for convection in developing cyclones to saturate the column (e.g., Nolan and Rappin 2008) and lessen the detrimental effects of shear entraining ambient, subsaturated air (Rappin et al. 2010; Tang and Emanuel 2010, 2012). In this section, we look at two measures of mid tropospheric moisture content, and relate changes to the spatial differences in the track densities presented in an earlier section.

Figure 47 shows the storm season mean (here and elsewhere defined as JASO in the Northern Hemisphere and as JFMA in the Southern Hemisphere) relative humidity at 600 hPa in the 20th century climate simulations (left panels) and the change at LGM (right panels). Humidity levels are high throughout the tropics, although MRI has notably higher *RH* values (>80%) than either CCSM4 or MPI across major swaths of the tropics. Changes in each model's storm season mean *RH* are shown in the right panels, with yellow and red colors indicating higher 20th century values (i.e., drier at LGM) and

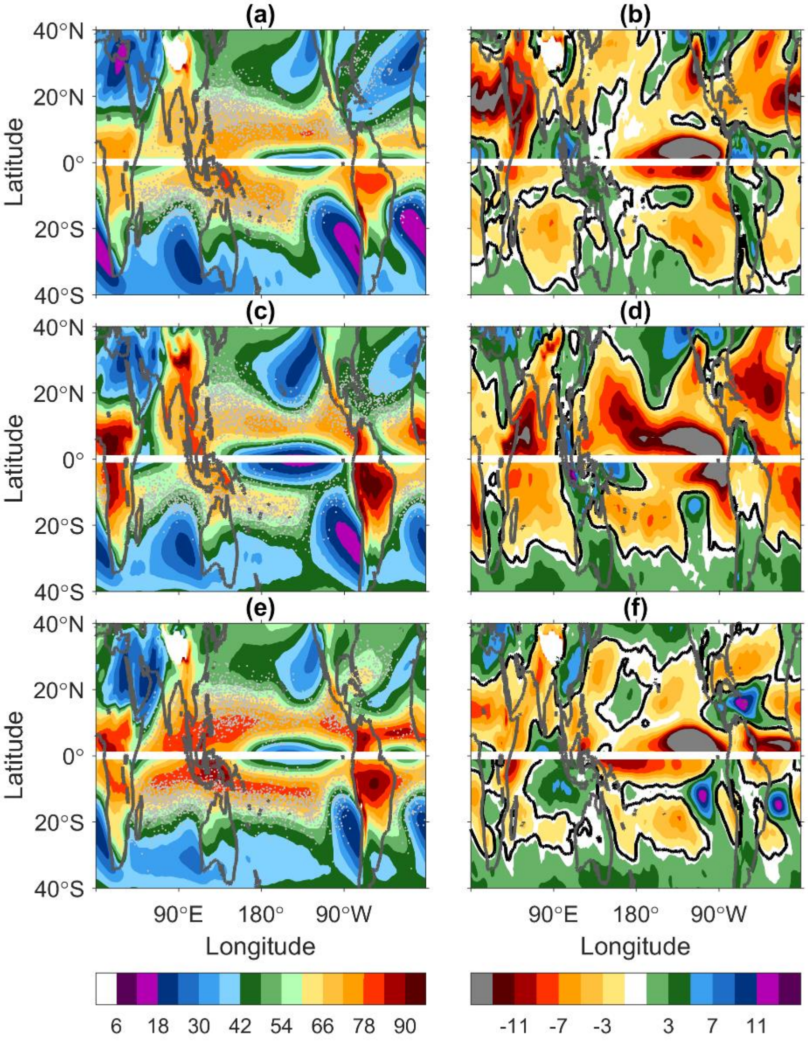

Figure 47 Storm season (July-October in Northern Hemisphere, January-April in Southern Hemisphere) relative humidity *RH* at 600 hPa in (a) CCSM4, (c) MPI, and (e) MRI 20th century climates overlaid with storm season genesis locations (gray shaded circles). Difference in *RH* at 600 hPa (LGM-20C) for (b) CCSM4, (d) MPI, and (f) MRI models. Black line denotes locations where *RH* at 600 hPa is equal between the two climates. Values shown are in percent.

green and blue values showing higher *RH* at LGM. CCSM4 shows generally small differences across the western North Pacific (±3%), but is more commonly drier at LGM in general. MPI shows larger reductions in LGM *RH* in both hemispheres. MRI shows more spatially mixed changes, with generally smaller magnitude changes in the

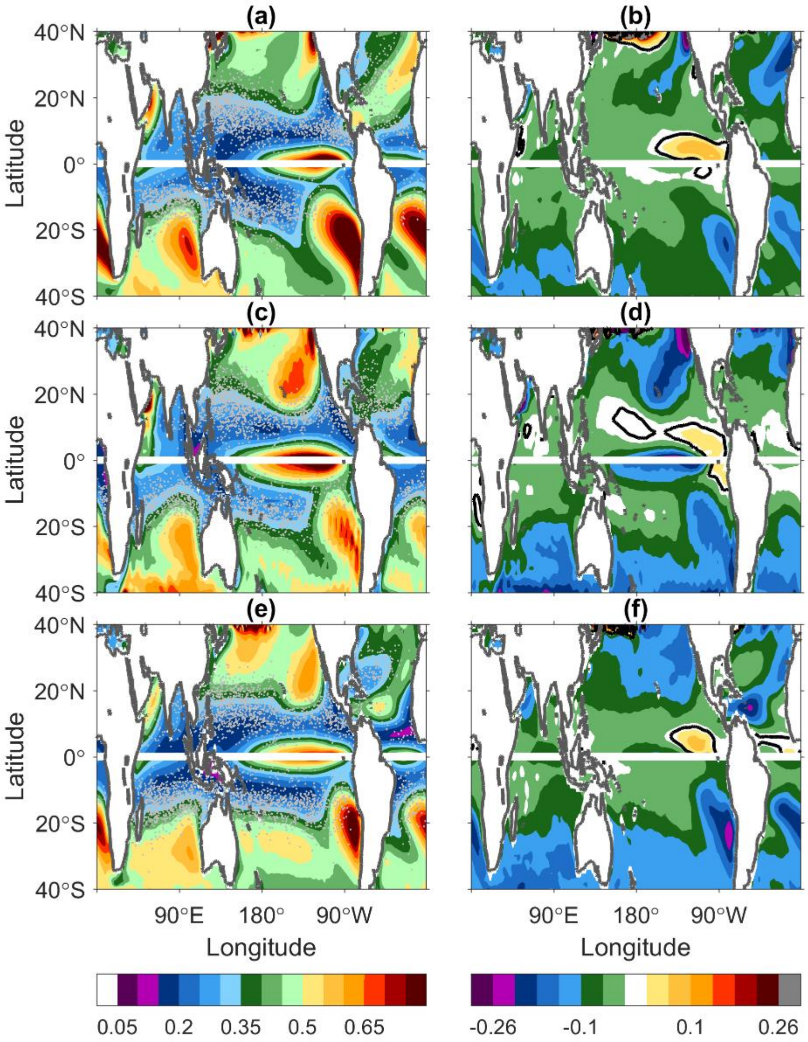

Figure 48 Storm season (July-October in Northern Hemisphere, January-April in Southern Hemisphere) thermodynamic resistance parameter χ in (a) CCSM4, (c) MPI, and (e) MRI 20th century climates overlaid with storm season genesis locations (gray shaded circles). Difference in χ (LGM-20C) for (b) CCSM4, (d) MPI, and (f) MRI models. Black line denotes locations where χ is equal between the two climates. Values shown are unitless.

tropical and subtropical North Pacific, but higher LGM *RH* in much of the tropical North Atlantic and Southern Indian Ocean. *RH* values are also higher at LGM in the central North Pacific.

Differences in relative humidity affect the actual (absolute) saturation deficits in conjunction with changes in temperature. Counterintuitively, colder environments provide a benefit to developing TCs in that the amount of moisture that it takes to moisten a column of tropospheric air is smaller (for fixed *RH*) than in a warmer environment. While the surface fluxes from the ocean that supply the moisture tend to be lower in colder environments too, they change more nearly linearly with temperature than do saturation deficits, which are exponential (Emanuel et al. 2008). The thermodynamic resistance parameter χ introduced in the last Chapter provides a non-dimensional measure of these effects.

Figure 48 shows χ for the storm season means of the 20th century simulations (left panels) and the differences at LGM (right panels; negative values [shown in green and blue] indicate lower LGM resistance, which is more favorable for TC genesis and development). The temperature effect dominates over the changes in *RH* shown in **Figure 47**, as nearly all of the tropics in all models have lower χ at LGM. However, χ is locally larger across much of the tropical North Pacific in MPI, which comes from two sources: conditions did not cool as much in MPI as in other models (see, e.g., *SST* in **Figure 44**) and *RH* is much lower at LGM in MPI than in other models (it is as approximately 10% lower across much of the central tropical North Pacific; see **Figure 47d**).

This drying at LGM in MPI is coincident with the decrease in TC genesis and tracks across much of the central and western Pacific (see **Figure 40d and Figure** 41**d**). Even though *PI* values did not change as much as in CCSM4, and *SSTs* did not cool as much, the drier midlevel conditions leads to an increase in χ at LGM here in MPI.

Vertical Wind Shear

Storm season mean 850-250 hPa wind shears are shown for each model's 20th century simulation in the left panels of **Figure 49**, and the changes at LGM are shown in the right panels (yellows and reds indicate larger shears at LGM). Storm genesis points (superimposed for each of the three models in the left panels) are coincident with regions of the lowest mean shear. At LGM, mean shears are larger in middle latitudes where temperature gradients are strong, approaching the very cold permanent ice sheets, but even through much of the tropics shears are higher in many areas at LGM. This is true in the tropical Atlantic of both CCSM4 and MPI, but MRI has higher shear in the 20th century than the other two models with significant reductions here at LGM. This is another change supporting the divergent Atlantic responses: MRI has more favorable shear at LGM than 20th century in this basin (in addition to higher *PI* at LGM and higher *RH* at LGM). Shear is also lower at LGM in the central Pacific near Hawaii in MRI, where track densities where higher. Shear is also lower in MRI across the band of the South Pacific near 20°S, where genesis, track, and *PDI* densities also increased (**Figure 39f, Figure 40f, and Figure 41f**). Higher LGM shears in MRI in the Indian Ocean and western North Pacific are consistent with the decrease in TC activity in that climate there. Both CCSM4 and MPI featured reduced Atlantic activity at LGM, consistent with the stronger shears in those basins. All three models show increases in shear at LGM in the far western North Pacific, and genesis, track, and PDI densities were all lower here too (right panels of **Figure 39-Figure 41**).

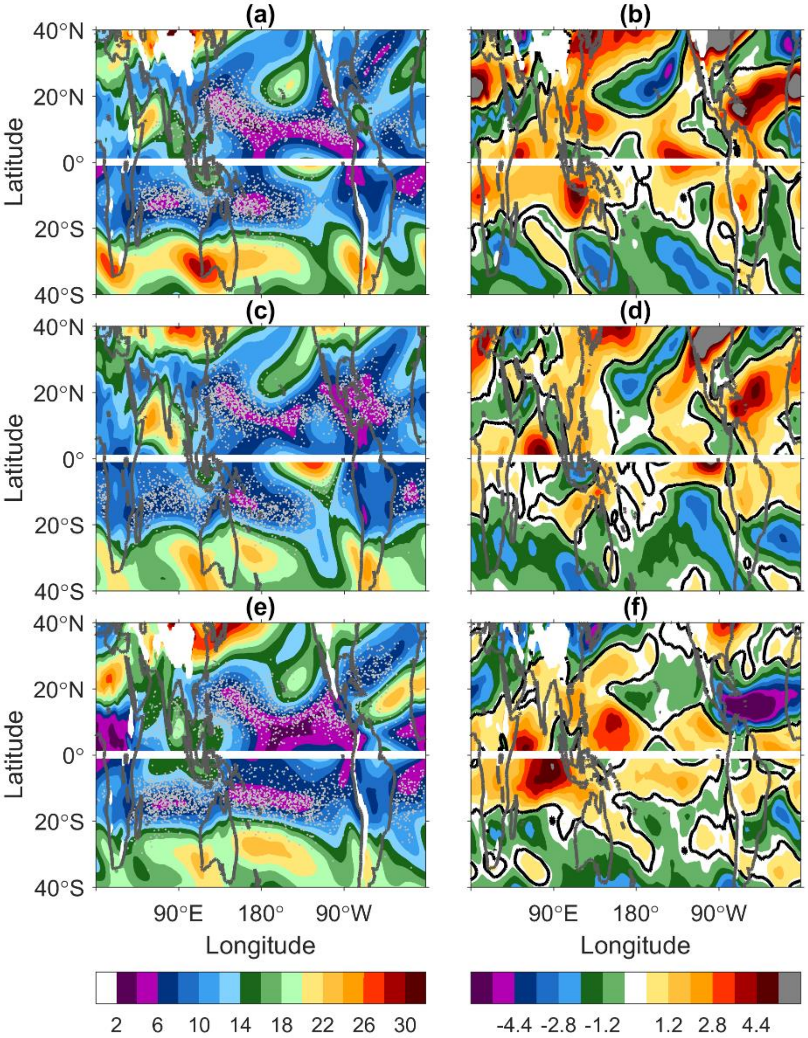

Figure 49 Storm season (July-October in Northern Hemisphere, January-April in Southern Hemisphere) vertical wind shear V_{shear} in (a) CCSM4, (c) MPI, and (e) MRI 20th century climates overlaid with storm season genesis locations (gray shaded circles). Difference in V_{shear} (LGM-20C) for (b) CCSM4, (d) MPI, and (f) MRI models. Black line denotes locations where V_{shear} is equal between the two climates. Values shown are in m/s.

As we noted at the start of this Chapter, fewer storms reach H4 and H5 intensity in all three LGM simulations than in their 20th century counterparts. **Figure 50a** shows the ratio of the average time that it takes to reach a particular intensity in LGM storms to the average time that it takes to achieve the same intensity in 20th century storms. There is little difference in the ratio for weaker intensities, and the ratio in MPI and CCSM4 actually is often <1 for intensities weaker than H2. This indicates that it takes about the

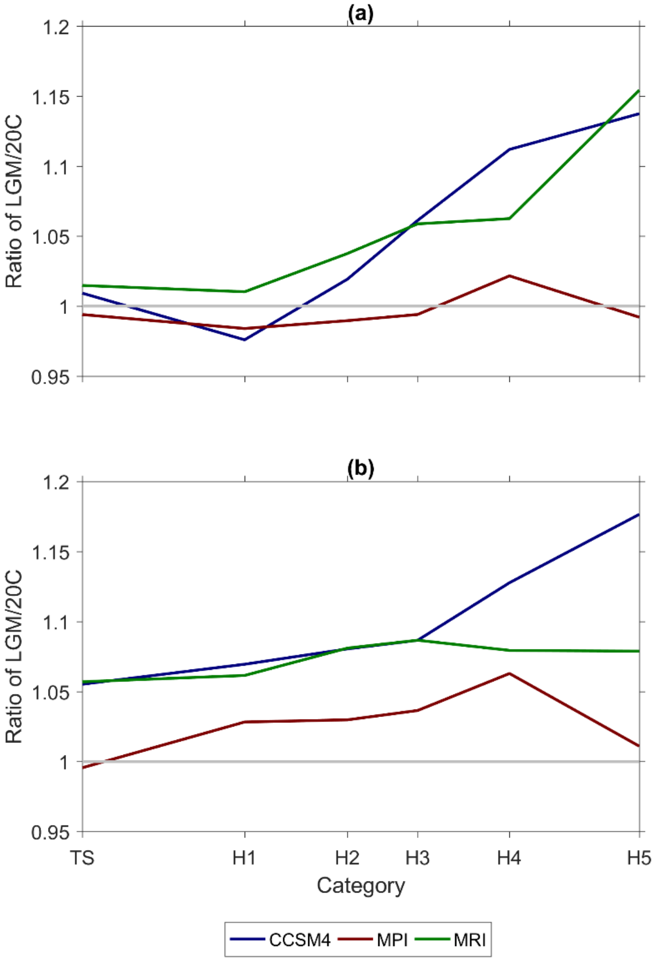

Figure 50 (a) Ratio of the average time storms take to reach tropical storm and hurricane classifications in CCSM4 (blue), MPI (red), and MRI (green). (b) Ratio of average storm V_{shear} during times to reach tropical storm and hurricane classification.

same time for LGM storms (or less time, when <1) to reach these intensities as it does in the 20th century. But it takes 10-15% longer for MPI and CCSM4's smaller number of LGM H4 and H5 storms to achieve these intensities. **Figure 50b** shows the ratio of the average wind shear experienced during the time leading up to these intensities, and they are consistently higher in CCSM4 and MPI. MRI has a ratio closer to 1, as shears are substantially lower through the Atlantic in its LGM simulation. The time to reach H5 intensity in MRI is, globally averaged, about the same for the two climates.

Ventilation Index

Normalizing the shears shown in **Figure 49** by PI and multiplying by χ yields the ventilation index Λ defined by Tang and Emanuel (2010). This is shown in **Figure 51** for the three models' 20th century experiments (left panels), with the change in Λ shown in the right panels. This combined metric incorporates the combined effects of shear and thermodynamic changes: lower values of shear that are offset by higher values of saturation deficits were shown to be more detrimental to storm development in the experiments of Rappin et al. (2010). The ventilation index is higher (less favorable) at LGM in the Atlantic of CCSM4 and MPI, while it is lower (more favorable) at LGM in MRI. These changes are all consistent with each model's respective changes in LGM activity in that basin. The ventilation index is higher at LGM in the western North Pacific of CCSM4 as well as in middle latitudes across the North Pacific. Track densities decreased here but they increased over the eastern half of the western North Pacific where the ventilation index decreases.

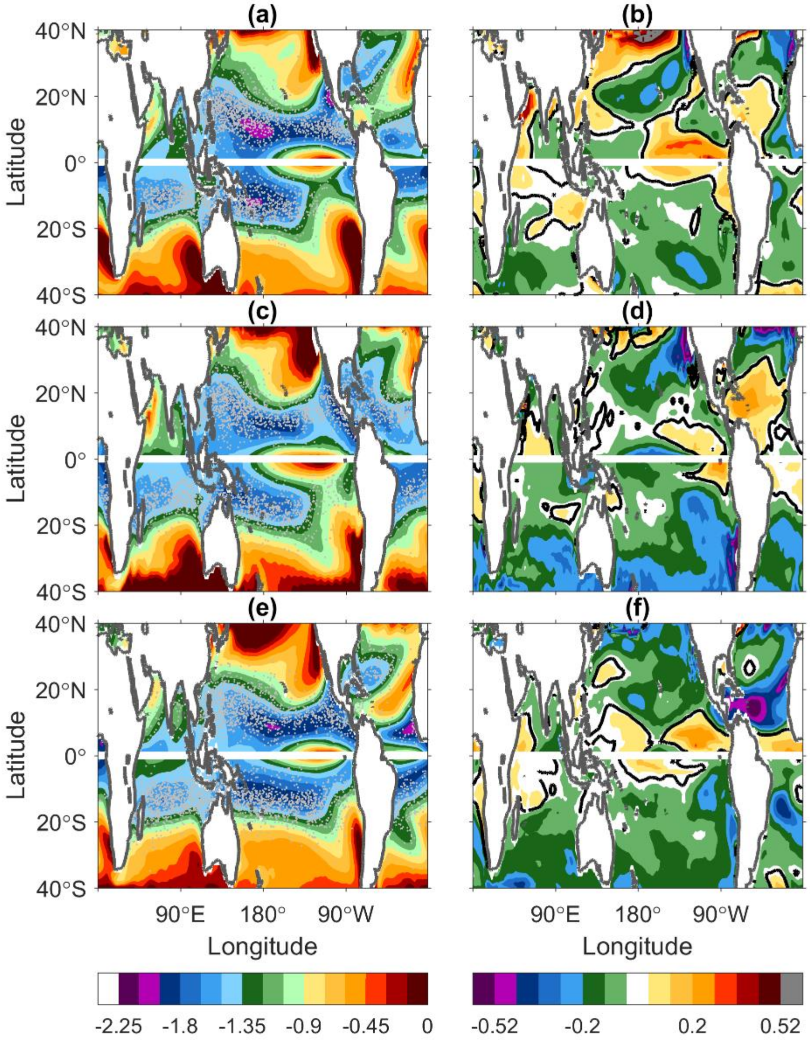

Figure 51 Storm season (July-October in Northern Hemisphere, January-April in Southern Hemisphere) logarithm of ventilation index $\log_{10}\Lambda$ in (a) CCSM4, (c) MPI, and (e) MRI 20th century climates overlaid with storm season genesis locations (gray shaded circles). Difference in $\log_{10}\Lambda$ (LGM-20C) for (b) CCSM4, (d) MPI, and (f) MRI models. Black line denotes locations where $\log_{10}\Lambda$ is equal between the two climates. Values shown are in unitless.

Figure 52 shows the difference in storm season track density at LGM (from right panels of **Figure 41**), but filtered to show only points where the ventilation index is higher at LGM than in the 20th century (i.e., conditions are, on average, less favorable at

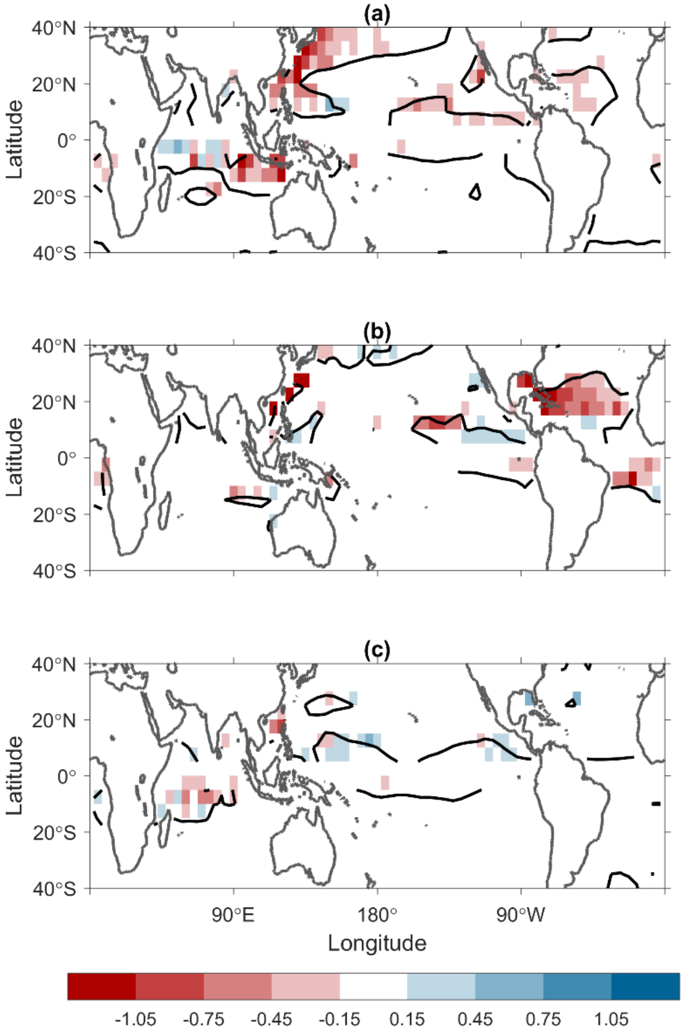

Figure 52 Difference in storm season track density. Only includes locations where storm season mean $\Lambda > 0$. Black line denotes line of zero change in storm season mean Λ.

LGM). The points where this condition is met feature mostly lower track densities at LGM. **Figure 53** is similar to **Figure 52**, but filtered to show only points where the ventilation index is lower (i.e., more favorable) at LGM. Their relationship is mixed, although the increase in LGM activity in MRI occurs concurrently with the large decreases in ventilation index in the Western Hemisphere (see **Figure 51f**). CCSM4

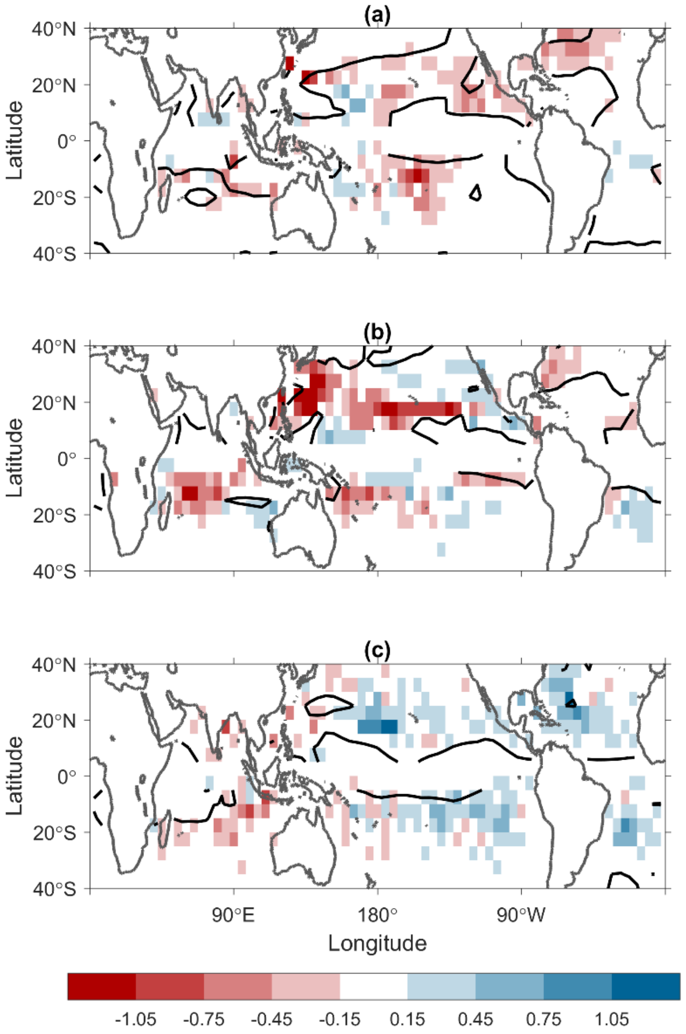

Figure 53 Difference in storm season track density. Only includes locations where storm season mean $\Lambda < 0$. Black line denotes line of zero change in storm season mean Λ.

shows some higher LGM activity where ventilation index drops in the eastern part of the western North Pacific, but there is a decrease in track density in the eastern North Pacific, Atlantic, and South Pacific despite the reduction in this index. MPI featured a lower ventilation index at LGM across most of the tropical North Pacific, but track density is lower. Some of this discrepancy may be related to the very small change in ventilation: **Figure 51d** shows that the change in ventilation index across the latitude belt where most storms form (see **Figure 51c**) in the Pacific in fact has close to zero change in ventilation. Also possible is that the much larger decrease in relative humidity at LGM in MPI (**Figure 47d**) is affecting the results more than its role in the ventilation index changes would suggest. As we will see in Chapter VII, the ventilation index does quite well predicting the locations of changes in TC activity in two experiments with CAM3 that go to very high levels of CO_2.

Latitude of Lifetime Maximum Intensity

Finally, we revisit the issue of differences in the latitude of lifetime maximum intensity Φ_{LMI} in the LGM. At the end of Chapter III, we saw that the vortices simulated directly by CCSM4 reached a peak intensity in LGM at an average latitude slightly poleward of where this occurred in the 20th century simulation in many basins (see **Figure 24**). However, the vortices examined in Chapter III are limited in the range of possible intensities by the spatial resolution of the model. The downscaling technique presented in this Chapter does not suffer from this limitation, and we revisit changes Φ_{LMI} in the downscaled set of storms by basin, hemisphere, and global mean in **Table 5**.

The data show the average absolute value of Φ_{LMI} for events downscaled from both climate experiments in the three global models. Differences that are statistically significant (using Welch's t-test) are highlighted in red or blue; red colors indicate Φ_{LMI} contracts equatorward with the cooling at LGM, while blue indicates Φ_{LMI} expands poleward at LGM. In CCSM4, Φ_{LMI} changes in many of the basins change in the same

Mean Φ_{LMI}	CCSM4 20C	CCSM4 LGM	MPI 20C	MPI LGM	MRI 20C	MRI LGM
Global	16.97°	16.67°	16.30°	16.79°	16.62°	17.14°
Northern Hemisphere	18.60°	18.09°	17.33°	17.82°	17.40°	18.32°
Southern Hemisphere	14.77°	14.86°	14.67°	15.48°	15.86°	15.91°
Southern Indian	12.98°	12.57°	13.04°	13.90°	15.42°	15.73°
Australia	14.58°	15.01°	13.54°	14.11°	14.64°	14.38°
South Pacific	18.13°	19.30°	19.05°	19.43°	17.60°	17.38°
North Indian	12.56°	13.05°	13.23°	15.24°	13.44°	14.50°
Western North Pacific	18.55°	18.03°	16.63°	17.36°	16.50°	16.84°
Eastern North Pacific	16.13°	16.79°	15.43°	17.34°	15.37°	15.76°
Atlantic	26.67°	24.68°	21.51°	21.88°	26.30°	26.36°

Table 5 Absolute value of mean latitude of lifetime maximum intensity of downscaled storms for 20th century and Last Glacial Maximum simulations for CCSM4, MPI, and MRI by basin. Gray shaded cells indicate basins that show no statistical difference in mean Φ_{LMI}.

way that the explicitly simulated vortices did in Chapter III (**Figure 24**). The average Φ_{LMI} moves equatorward at LGM in the South Indian and Atlantic basins in both cases.

The average Φ_{LMI} moves poleward at LGM in the Australia region, South Pacific, North Indian, and eastern North Pacific in both methods. The western North Pacific, which is responsible for the largest amount of the activity in any basin of the Northern Hemisphere showed a poleward shift in the Φ_{LMI} of explicitly resolved systems at LGM, but the downscaled set in Table 5 show a statistically significant (~0.5°) equatorward contraction in this basin.

Both MPI and MRI show a poleward shift in all Northern Hemisphere basins. (These are significant for MPI in all except the Atlantic, but the changes are statistically

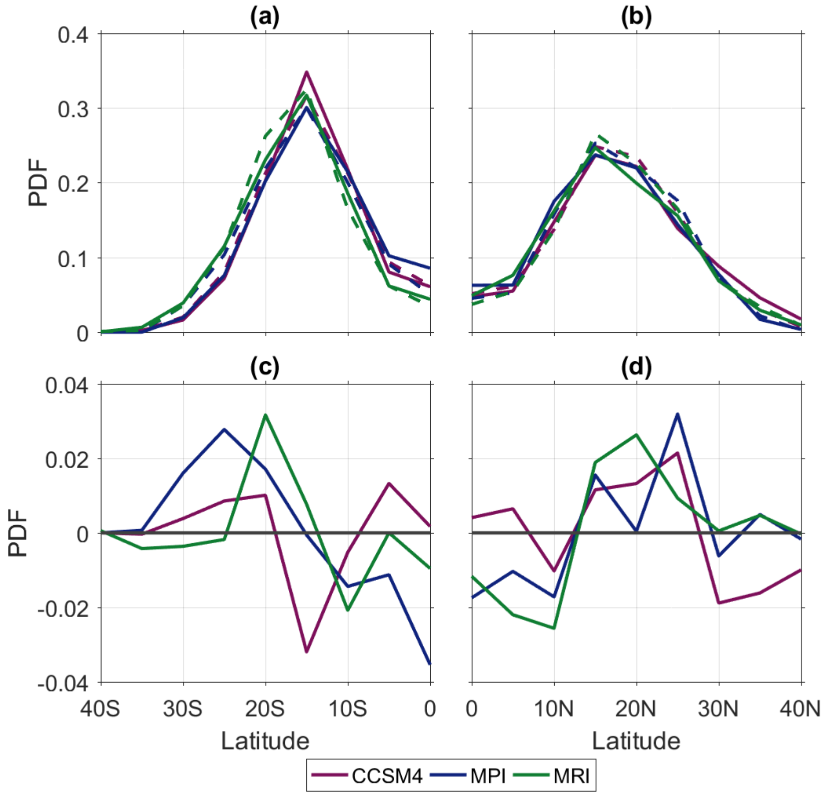

Figure 54 Probability distribution of Φ_{LMI} for CCSM4 (purple), MPI (blue), and MRI (green) 20th century (solid) and Last Glacial Maximum (dashed); (a) northern and (b) southern hemisphere downscaled storms. LGM-20C difference of the probability distribution of $\Phi\text{-}LMI$ for (c) Northern and (d) Southern Hemisphere storms.

insignificant for MRI). Recall that the responses of the *SST* fields (**Figure 44**) between models differed, with a sharp cooling of the North Pacific in CCSM4 that was diminished or absent in MPI and MRI. *PI* values (**Figure 45**) were higher at LGM in subtropical latitudes of the North Pacific of MPI and MRI, while they were significantly lower in CCSM4 between 20°N and 40°N. Also note that changes in basin activity can affect these results: while none of the differences in Φ_{LMI} in individual basins is statistically significant in MRI, the large increase in activity in the Atlantic lifts the hemispheric (and global) average position of Φ_{LMI}. (Φ_{LMI} occurs much farther poleward in the Atlantic than in other basins.) **Figure 54** shows the distribution of all Φ_{LMI} by latitude. The top panels show that there is a great deal of similarity between all of the models and the two climates.

Our findings show there are some qualitative correlations between environmental factors with tropical cyclone activity, particularly in areas featuring large differences in a single variable or a combination of many relatively favorable factors. CCSM4 and MPI models showed decreases in TC genesis during the LGM, while MRI showed an increase in the total counts (this increase is predominantly from weaker storms). In some regions (e.g. the Atlantic basin) models showed divergent responses in TC activity between the two climates, concurrent with changes in vertical wind shear and relative humidity that predict this response. Changes in vertical wind shear generally shows consistency with changes in TC activity (regions of high LGM wind shear such as in the MRI Indian Ocean and western North Pacific, as well as CCSM4 and MPI Atlantic showed decreases in track density. The MPI model showed a much larger degree of drying (lower values of *RH*) coincident with decrease in TC genesis across much of the central and western Pacific. Most importantly, each of the models showed decreases in the number of highest intensity storms and global power dissipation at the LGM, consistent with results of increased events with increased warming in the 21st century.

CHAPTER VI

MID-HOLOCENE

In this Chapter, we apply the techniques introduced in earlier chapters to simulations of the mid-Holocene. By six thousand years ago (6ka), CO_2 was 280 ppm, the level it would remain until the industrial revolution. Although methane levels were ~100 ppb lower than the preindustrial era, broadly speaking the Holocene is characterized by a stable climate. The major difference over the period comes from the precession of Earth's orbit, and so we focus on the changes in the seasonal cycle caused by top-of-the-atmosphere (TOA) solar radiation anomalies. We begin this chapter by providing a background on the precession of Earth's orbit, the changes it causes in TC environmental factors, and then present the response of both explicitly simulated systems in CCSM4's mid-Holocene run and results from applying Emanuel's downscaling technique.

Introduction

There is a growing source of geologic evidence of prehistoric storm activity from the Holocene. The first evidence came from select coastal sites where coarse-grained sand layers in sediment records taken on the inland side of barrier islands were identified (e.g., Liu and Fearn 1993, 2000; Donnelly 2005). Liu and Fearn (1993) proposed that these sand layers were preserved sediment transported by a strong storm surge to inland lakes, inserting a layer of sand on top of the ordinary organic-rich sediment. These large grain sediments are most likely deposited via intense tropical cyclones that generate large storm surge, and they provide evidence of variability in overwash deposits over the length of the core, which often spans the most recent two or three millennia. Radiocarbon dating is applied to the organic material at both ends of the sand layers to estimate the age of the sand deposit.

In select locations along the East Coast of the United States, historical observations of TCs recorded (e.g. weather logs) over the past 400 years can be used as another line of support for recent centuries of this analysis. Woodruff et al. (2008) has shown that a core from Cape Cod, Massachusetts, contained sedimentary deposits from a number of historic storms, including Hurricane Carol in 1954, the Great New England Hurricane in 1938, the Great September Gale in 1815, and the Colonial Hurricane of 1635, which was observed in the Jamestown, Virginia, colony a day earlier.

Overwash records in a sedimentary core create the ability to examine hurricane frequency in recent millennia, as some of these cores extend back to the age of modern barrier islands 5,000 years ago. The current barrier islands have been fairly stable over this time period due to the slowing of sea level rise that began around that time. Before 5,000 years ago, the change in sea level was much faster (Lighty et al. 1982), and barrier islands that existed then have succumbed to the rapid dynamics of coastal geomorphology.

However additional new methods may open the possibility of examining deep-sea sediment cores back to the late Pleistocene (i.e. prior to 11ka; Toomey et al. 2013). This technique, while still in its infancy, examines offshore cores located on sloping banks. As a storm travels across the ocean it generates strong currents in the ocean mixed layer, which over time will transfer momentum into the thermocline below it. Inertia-gravity waves, excited by the passage of strong surface winds, propagate downward (Price 1983) and pick up coarse-grained material from adjacent shelves and transfer them to sloping canyon walls where they would not be normally found. It is in these locations that a core can be drilled to possibly obtain records from earlier than was possible on barrier islands. Initial analysis in the Great Bahama Bank using this technique have been consistent with findings produced from nearby overwash records (Toomey et al. 2013), and cores from the Dry Tortugas show a stormy period during the Younger Dryas, 12-13 thousand years ago (Toomey et al. 2016).

The results from recent millennia show a large variability in storm frequency correlated with independent proxies of ENSO and West African Monsoon variability. However, prior to this time, increased Northern Hemisphere solar during the summer months had larger effects on seasonal climate, and Korty et al. (2012b) showed that it was likely to have repressed TC activity in the Northern Hemisphere during middle Holocene. The limited proxy evidence prior to 4ka generally shows little middle Holocene activity at sites in the Northern Hemisphere (Toomey et al. 2013), but there is not yet a large amount of geologic data from the period.

Berger (1978) calculated the variation in Earth’s orbital parameters over time, and 6000 years ago (6ka) Earth made its closest approach to the Sun during September (this occurs during January in modern times). Simulations of this period (Braconnot et al. 2007) are forced by this shifted seasonal cycle of solar radiation, which features larger top of the atmosphere radiation between June and October and reduced levels 6ka during the Southern Hemisphere summer months.

The orbital geometry during the mid-Holocene (MH; defined here to be 6ka) makes it an interesting period to examine. The atmospheric composition during this time is similar to that of the pre-industrial era, but the perihelion (when Earth is closest to the sun) occurred during September, the peak month of hurricane season in the Northern Hemisphere in modern times. The resulting shift in the top-of-the-atmosphere distribution during the mid-Holocene is the driving force behind the major differences in the seasonal cycle of climate. This variation results in the land surface warming faster than the ocean because of their different heat capacities, and Korty et al. (2012b) argued that this was also responsible for the increased tropospheric stability found over oceans. The warming of the upper troposphere coupled with little immediate change in the ocean surface temperature resulted in stabilized lapse rates, lower potential intensity, and larger saturation deficits in the mid-troposphere during the early months of the Northern Hemisphere TC season. By October, as ocean surface temperatures warm after several months of larger TOA solar radiation, the negative potential intensity anomalies disappeared.

Figure 55 plots the TOA solar radiation anomalies over the past 10k years (measured relative to our current climate) averaged over the 5°N – 20°N and 20°S – 5°S latitudinal bands for the peak months of each hemisphere's respective TC season. This plot was created by first calculating the daily insolation received as a function of latitude and past time (over the last 10k years) and then subtracting the modern-day value at that

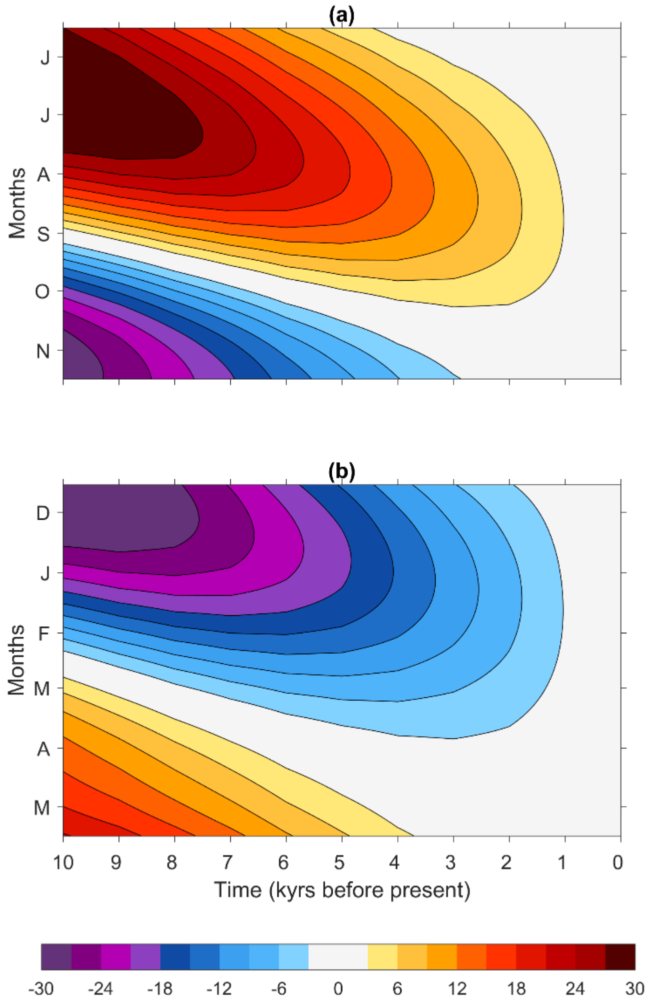

Figure 55 Top-of-the-atmosphere solar radiation anomalies over the past 10k years relative to our current climate averaged over the (a) 5°N – 20°N and (b) 20°S – 5°S latitudinal bands during the peak months of each hemisphere's respective TC season.

latitude to get the anomaly. This plot shows more TOA solar radiation was received between June and October during the mid-Holocene Northern Hemisphere storm season than is today. The Southern Hemisphere storm season is dominated by negative anomalies during this period, as Earth makes its closest approach to the Sun today in

January. The precession of Earth's orbit results in a significant change in the received solar insolation (~20 W m^{-2}) during the MH at these tropical latitudes, and results in changes in surface temperatures as well. However, over the ocean changes in *SSTs* tend to lag the anomalies in TOA solar radiation themselves, while temperature changes over land in at upper levels of the troposphere respond more rapidly to these anomalies. This results in an increase in stability in the MH in months of positive TOA radiation anomalies, and a decrease in stability during months of negative TOA radiation anomalies. The influence of these changes on potential intensity and tropical cyclone climatology is our primary interest in the mid-Holocene.

Effect on the Tropical Pacific Climate

Karamperidou et al. (2015) show that the mid-Holocene TOA anomalies affect the seasonal cycle of the Pacific equatorial cold tongue. In the 20th century and preindustrial era climate simulations, CCSM4 produces a fully developed cold tongue along the equator of the eastern and central Pacific during the late summer and fall months (JASO), concurrent with stronger southeasterly and northeasterly trade winds and the maximum northward extent of the intertropical convergence zone (ITCZ). They also show that, consistent with observations, the simulated cold tongue disappears during late Northern Hemisphere winter and spring. During this interval (February to May), trade winds are weaker.

In response to the stronger JASO radiation, Karamperidou et al. (2015) show that there is a weakening of the seasonal cycle in the cold-tongue region, with warmer *SSTs* (relative to the preindustrial era control) during JASO, and colder *SSTs* from February to May. The simulated trade winds are actually stronger during JASO in the mid-Holocene (Mantsis et al. 2013), which should drive a stronger cold tongue from Ekman transport away from the equator during these months, but the cold tongue actually warms in the simulation. Ocean dynamics are necessary to explain the discrepancy between the stronger trade winds yet weaker summer/fall cold tongue.

The analysis of Karamperidou et al. (2015) also showed that anomalous westerly winds in the western Pacific resulted in what they called an “annual Kelvin wave”, which is visible in the difference in thermocline depth between 6ka and the preindustrial era control (cf. their Fig. 6). The Kelvin wave pattern propagates across the Pacific in the mid-Holocene simulation during summer and reduces the eastern Pacific upper ocean stratification by fall.

Whether other models (or nature) respond in the same way to the mid-Holocene forcing is a question beyond the scope of this thesis. We review this response in CCSM4, however, as it affects the *SST* patterns felt by TCs in the different simulations. Our interest is in the relationship between TCs and their environment, whatever the source of the changes in that environment. This is considered in the next section, with the changes in TC climatology from both the Emanuel downscaling method and directly simulated vortices to follow.

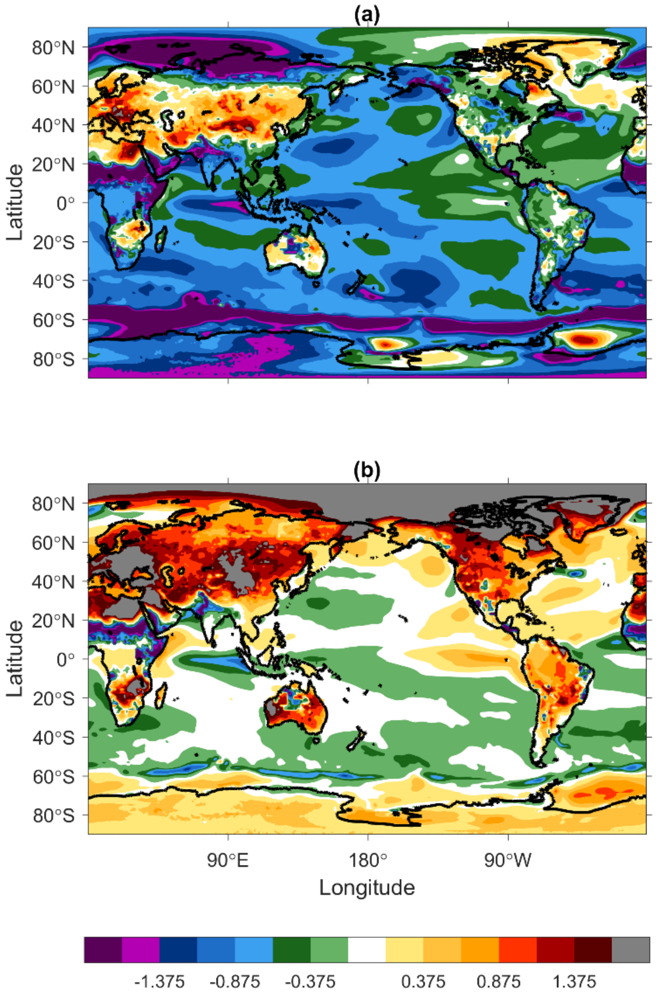

Figure 56 Change in Northern Hemisphere peak season (July-October; JASO) surface temperature T_{sfc} between (a) mid-Holocene and 20th century, and (b) mid-Holocene and preindustrial experiments.

Effects on Environmental Conditions

The change in surface temperatures averaged over the period July to October at mid-Holocene are shown in **Figure 56**. We compare to both the preindustrial era simulation and to the 20th century simulation. The late 20th century is warmer than either the mid-Holocene or preindustrial era run because of the cumulative effects of building CO_2 and other greenhouse gases. A second effect superimposed on this is the change in seasonal cycles induced by the different orbital parameters at MH. We include the charts showing the difference between MH and preindustrial era also to separate this element of the total response.

Korty et al. (2012b) showed that the different timescales for land and ocean surface temperatures to respond to the solar radiation anomalies led to lower potential intensity values during the summer months of the Northern Hemisphere TC season, as both land surface and upper tropospheric temperatures warmed faster than ocean surface temperatures did. This led to more stable lapse rates over tropical oceans in Northern Hemisphere summer, which in turn reduced potential intensity values.

The difference in surface temperatures shown in **Figure 56** reveals that temperatures along the equatorial cold tongue are warmer at mid-Holocene during these months than in the preindustrial era control. Across all tropical oceans, temperatures are universally cooler than in the 20th century, but the cooling is much smaller in the equatorial cold tongue region than in the western North Pacific. This relative change in *SST* means that the western Pacific was relatively colder at mid-Holocene than it is today (or in other words it is less warm relative to the remainder of the tropics), while the eastern North Pacific was relatively warmer. Temperature differences in the Atlantic are similar to those of the eastern North Pacific.

In response to this change in *SST* pattern, the potential intensity values shown in **Figure 57** were lower in the western North Pacific during JASO in the mid-Holocene,

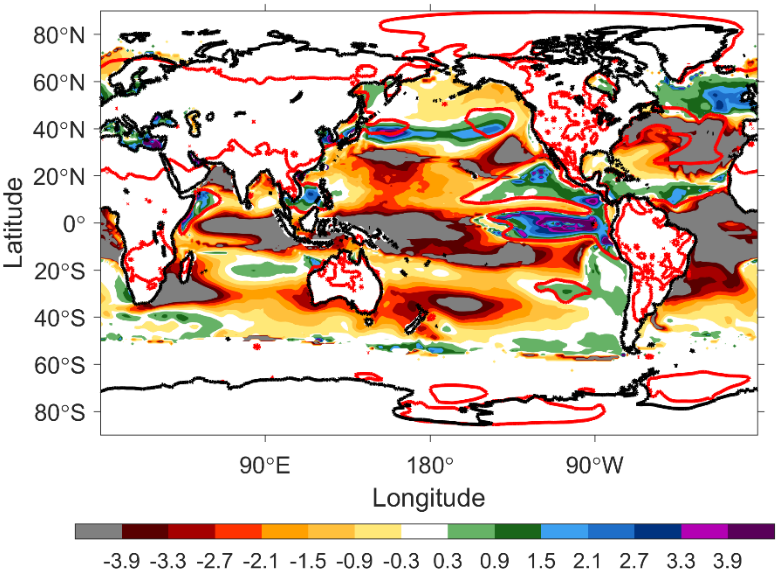

Figure 57 Change in Northern Hemisphere peak season (JASO) potential intensity *PI* between mid-Holocene and 20th century experiments, overlaid with change in surface temperature ΔT_{sfc} = -0.5°C contour (red).

while it was locally higher in the eastern North Pacific compared to the 20th century. As in the case with the LGM, despite the universally colder temperatures at mid-Holocene (compared to 20th century), some areas have higher *PI* because they cooled less than others. (Note here that the differences in temperature are all small compared to the anomalies at LGM.) In **Figure 57** we have overlaid the ΔT_{sfc} = -0.5°C contour to show the strong relationship between relative changes in *SST* and *PI* (Vecchi and Soden 2007). Where *SST* cooled more than this (i.e., the western North Pacific), *PI* fell. Where it cooled by less than this amount, *PI* remained the same or increased despite the lower temperature (eastern North Pacific and Atlantic).

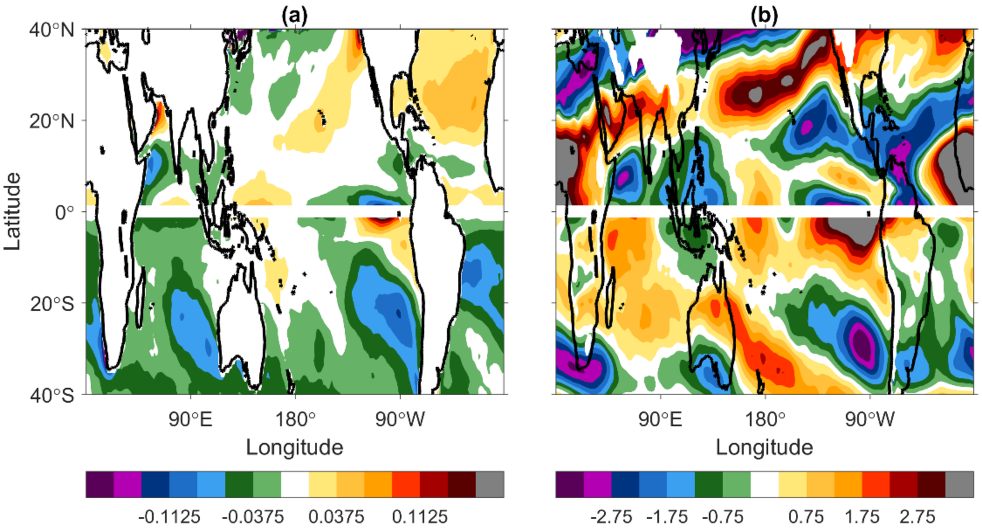

Figure 58 Change (MH-20C) in peak season (JASO in Northern Hemisphere, JFMA in Southern Hemisphere) (a) thermodynamic resistance parameter χ, and (b) 850-250 hPa shear V_{shear}.

Seasonal means of the difference between mid-Holocene and 20th century thermodynamic resistance parameter (χ), and 850-250 hPa shear (V_{shear}) are shown in **Figure 58**. Korty et al. (2012b) used a genesis potential index to summarize the cumulative effects of the different thermodynamic properties and wind shear at the mid-Holocene (cf. their Figure 8). As they noted, at the time there was not yet any study of simulated or downscaled storms in paleoclimate data, so the index was intended only a means to summarize the combined effects of individual factors. Nevertheless, the form they used has shown success relating activity from simulations of anthropogenic projections of warming with the environmental factors in those models. They used the form introduced by Emanuel (2010) but restricted the vorticity dependence to near equatorial latitudes, adopting the results of Tippet et al. (2011) who showed that elevated levels of absolute vorticity had no additional influence on genesis beyond ~10° or 15° latitude. The index is defined:

$$GPI = \frac{\boldsymbol{a\left[min\left(|\eta|, 4 \times 10^{-5}\right)\right]^3 [max(PI - 35, 0)]^2}}{\boldsymbol{\chi^{4/3}[25 + V_{shear}]^4}} \qquad (5)$$

where a is a normalizing coefficient chosen to predict an annual total of 80 events in the modern control climate, η is the absolute vorticity, and all other variables are as defined previously. Note that *GPI* is structurally similar to the inverse of the ventilation index, but with different offsets, weights, and exponents for its individual components.

Koh and Brierley (2015) repeated this method on the newer ensemble of mid-Holocene simulations from PMIP3, and found a repression of conditions during the Northern Hemispheric season, but without evidence of a late season rebound in October and November of the Northern Hemisphere. CCSM4's simulations were a part of this newer ensemble, and we apply (**5**) to its data here. **Figure 59** shows the annual cycle of (**5**) for each hemisphere of CCSM4's 20th century and mid-Holocene cases and a spatial map of the changes in each hemisphere's storm season. The annual cycle of *GPI* follows the seasonal cycle of historical tropical cyclones having peak values in September in the Northern Hemisphere and March in the Southern Hemisphere in both climates. Values of *GPI* are overall larger in the 20th century climate in both hemispheres, but show increases in the mid-Holocene during many months in the Southern Hemisphere.

Figure 59c shows the difference in storm season mean of *GPI* in both hemispheres, highlighting the regional increases in its value in many locations in the MH despite having lower values overall. *GPI* is enhanced in the mid-Holocene in a swath of

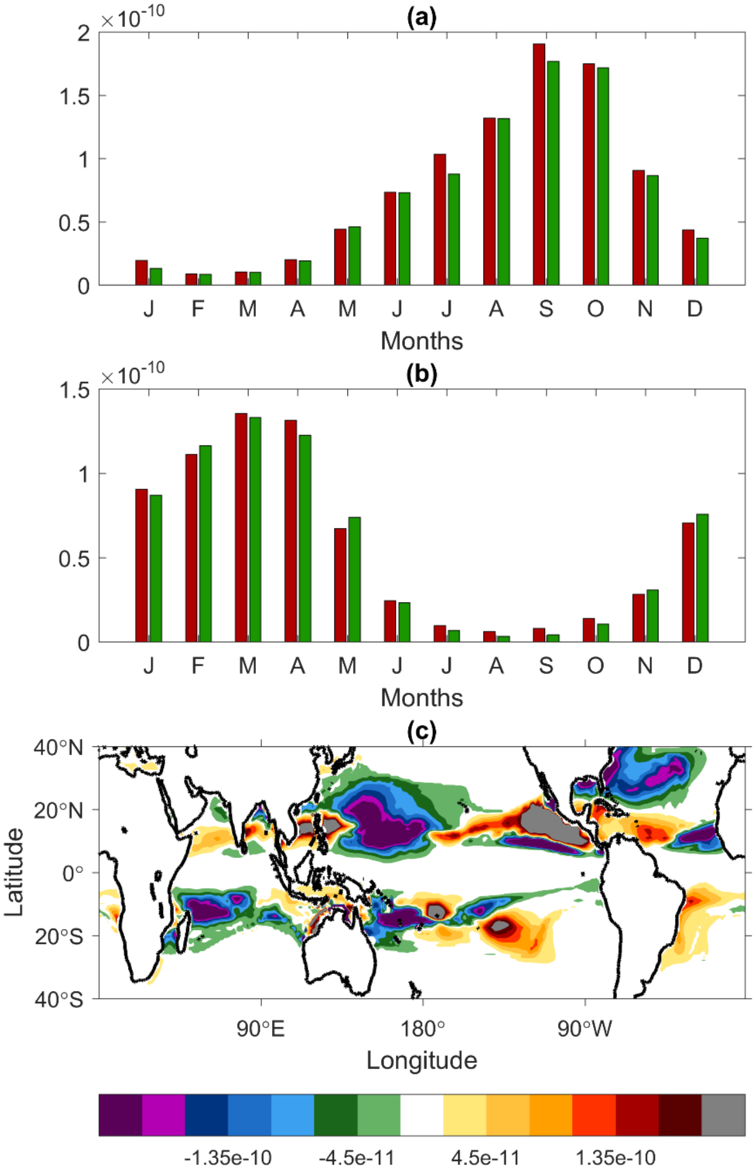

Figure 59 Annual cycle of genesis potential index *GPI* in the (a) Northern and (b) Southern Hemisphere for 20th century (red) and mid-Holocene (green) storms. (c) Storm season mean (JASO in NH, JFMA in SH) change in *GPI* between mid-Holocene and 20th century experiments.

area off the western coast of Central America into parts of the central Pacific, off the eastern coast of Central America (south of the Gulf of Mexico), and parts of the western

North Pacific and North Indian ocean along the ~10°N band. In the Southern Hemisphere, *GPI* has higher MH values off the eastern coast of South America (where there is little historical activity but a few storms do form), and parts of the central Pacific.

In the following sections we examine the climatology of downscaled TCs using the Emanuel seeding method applied in the last Chapter to the LGM. We also look at changes in the warm-core vortices simulated directly in CCSM4 and tracked with the Camargo and Zebiak (2002; henceforth CZ02) algorithm. In both cases, we compare changes in the climatology with changes in the large-scale environmental factors introduced here.

Statistically Downscaled Storms

We now examine results of downscaling CCSM4's mid-Holocene experiment to the climatology of events from its 20th century and preindustrial era simulations. While we continue to use the 20th century simulation as a control case (as it is the only period against which output can be compared to observations), we include the result of downscaling the preindustrial era control as well, to see what effects the changes in orbit had in isolation from the changes in CO_2 and other greenhouse gas changes since the industrial revolution.

The annual frequency of events in the 20th century has been calibrated to be 80 storms per year to match observations, and data breaking down the total number by intensity category and by hemispheres is shown in **Table 6**. The preindustrial era run produced 76 per year (5% fewer), and the mid-Holocene yielded 71 per year (10% lower than 20th century; 5% lower than preindustrial era). The decline from 20th century to mid-Holocene is statistically significant, but the smaller differences between the 20th century to preindustrial era and from preindustrial era to mid-Holocene are not.

	Annual Frequency	**Number of TS**	**Number of H1**	**Number of H2**	**Number of H3**	**Number of H4**	**Number of H5**
MH	71.2	35.29	11.98	7.4	5.52	6.63	4.38
20C	*80* ***(+12%)***	*40.7* ***(+15%)***	12.42 **(+4%)**	7.85 **(+6%)**	*6.78* ***(+23%)***	7.32 **(+10%)**	4.93 **(+13%)**
0k	*75.9* ***(+7%)***	36.23 **(+3%)**	*13.7* ***(+14%)***	7.52 **(+2%)**	5.91 **(+7%)**	6.27 **(–5%)**	4.46 **(+2%)**
MH (NH)	40.12	19.39	6.5	4.31	3.02	4.1	2.8
20C (NH)	*44.04* ***(+10%)***	*22.97* ***(+18%)***	6.89 **(+6%)**	4.19 **(-3%)**	3.59 **(+19%)**	3.7 **(-10%)**	2.7 **(-4%)**
0k (NH)	*43.5* ***(+8%)***	*20.9* ***(+8%)***	*8.24* ***(+27%)***	4.48 **(+4%)**	3.06 **(+1%)**	4.03 **(-2%)**	2.79 **(±0%)**
MH (SH)	31.08	15.9	5.47	3.09	2.5	2.53	1.59
20C (SH)	*35.96* ***(+16%)***	*17.73* ***(+12%)***	5.53 **(+1%)**	3.66 **(+18%)**	*3.19* ***(+28%)***	*3.62* ***(+43%)***	2.23 **(+40%)**
0k (SH)	32.4 **(+4%)**	15.33 **(-4%)**	5.46 **(±0%)**	3.04 **(-2%)**	2.85 **(+14%)**	2.24 **(-11%)**	1.67 **(+5%)**

Table 6 Downscaled Storms. Average number of mid-Holocene, 20th century, and preindustrial (0k) storm counts by intensity. Colored values indicate percentage change between 20th century and MH (20C-MH/MH), as well as preindustrial and MH (0k-MH/MH) storm counts. Green colors indicate larger number of MH generated storms.

Figure 60 shows the difference in track density between mid-Holocene and (a) 20th century and (b) preindustrial era. As expected from the changes in *PI* and relative *SST* pattern, there is a decline in TC activity in the western North Pacific while the

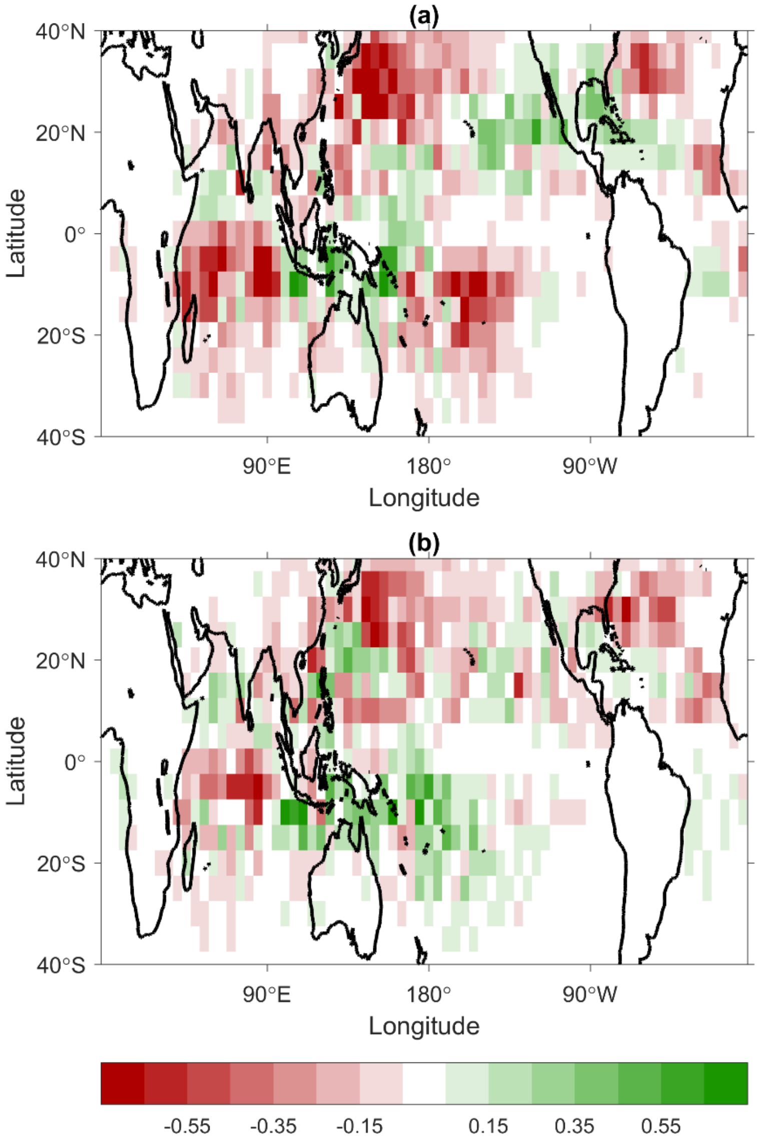

Figure 60 Downscaled storms. Total difference in track density between mid-Holocene and (a) 20th century, and (b) preindustrial era experiments. Values shown are in number of storm days per year.

eastern North Pacific shows more TC tracks at mid-Holocene. The data in **Table 6** shows that the decline between mid-Holocene and preindustrial era in the Northern Hemisphere activity comes mostly from the weaker part of the intensity spectrum: there is a ~10% decline in tropical storms and Category 1 hurricanes, but smaller changes in stronger ones. Decreases in tropical cyclone activity in the South Indian Ocean and western North Pacific are consistent with the decreases in *GPI* in these regions. In addition, increases in activity north of Australia and off the eastern coast of South America is concurrent with increases in *GPI*.

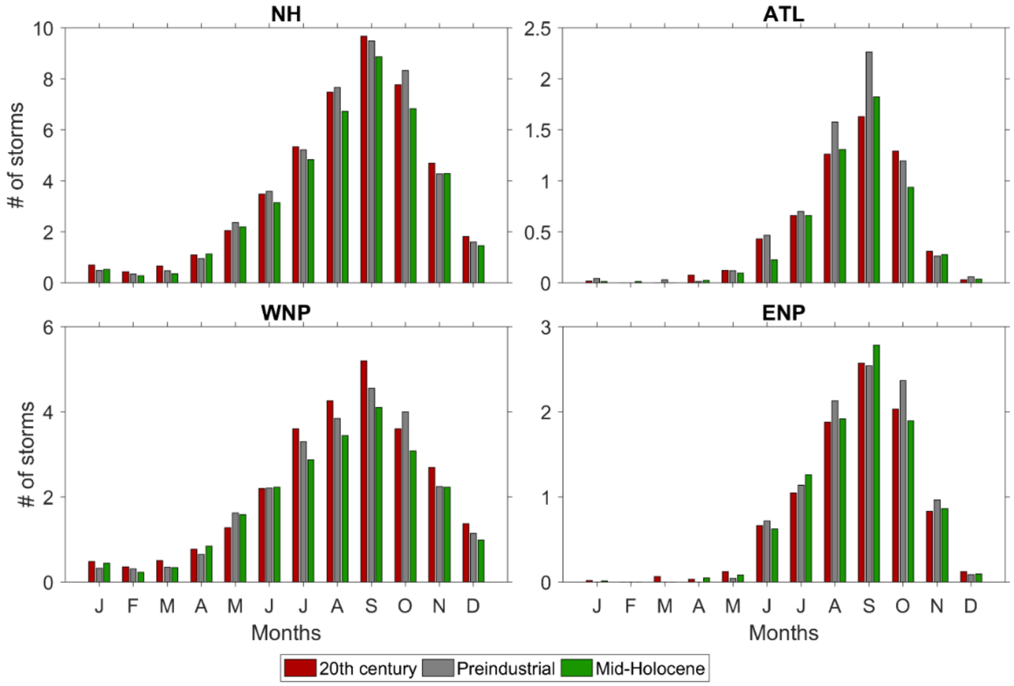

Figure 61 Downscaled storms. Annual cycle of events for 20th century (red), preindustrial era (gray), and mid-Holocene (green) in (a) Northern Hemisphere, (b) Atlantic, (c) western North Pacific, and (d) eastern North Pacific basins.

Figure 61 shows the annual cycle of events in 20th century, preindustrial era, and mid-Holocene in the Northern Hemisphere, Atlantic, western North Pacific, and eastern North Pacific. There is less activity in the Northern Hemisphere at mid-Holocene in every month except April and May. The annual cycles by basin shows that the decline in the western North Pacific is largest from July to November, consistent with the relative warming of the eastern North Pacific during these months reported by Karamperidou et al. (2015). There are smaller differences during the offseason months in the western North Pacific, and some of them feature more activity at mid-Holocene than in the 20th century. In the eastern North Pacific and Atlantic, mid-Holocene activity is the same as or higher than in the 20th century between July and September. During these months, *SSTs* in the Western Hemisphere are not as much cooler than the tropical mean in the

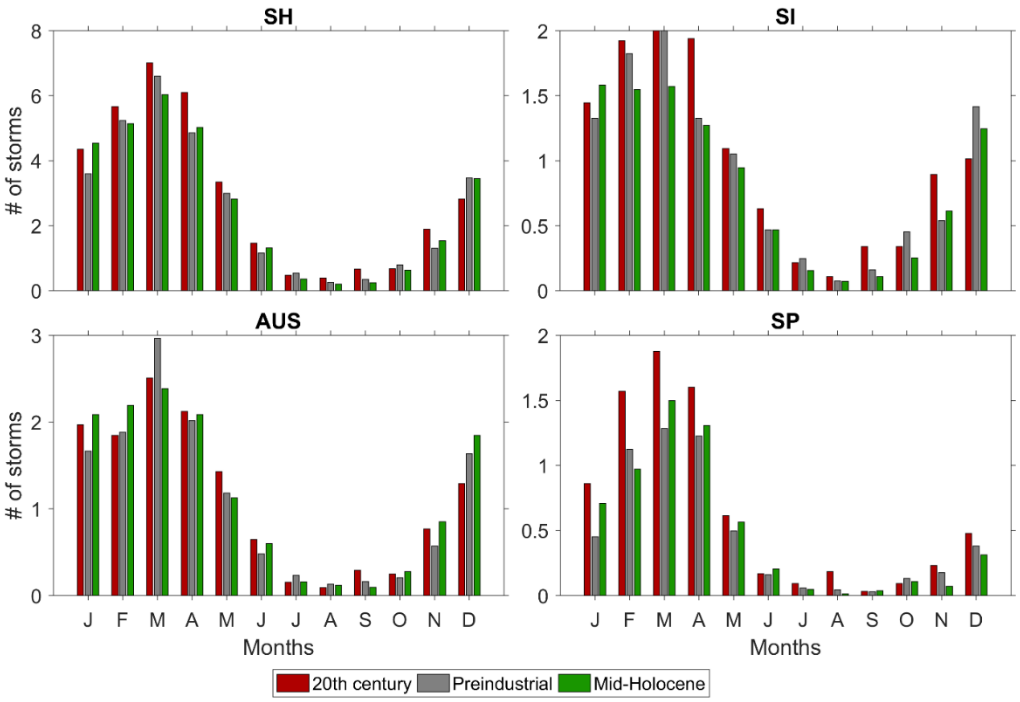

Figure 62 Downscaled storms. Annual cycle of events for 20th century (red), preindustrial era (gray), and mid-Holocene (green) in (a) Southern Hemisphere, (b) South Indian, (c) Australian, and (d) South Pacific basins.

mid-Holocene as they are in the 20th century. (Relative *SST* increases here, leading to the higher *PI* at mid-Holocene.)

Figure 62 shows the annual cycle of events in 20th century, preindustrial era, and mid-Holocene in the Southern Hemisphere, South Indian, Australia, and South Pacific basins. There is more activity in the Southern Hemisphere at mid-Holocene only in December and January when compared to the 20th century. Of the southern hemisphere peak season months, March and April have consistently lower values of MH genesis, particularly in the South Indian Ocean, while the Australian basin shows increases in January and February. There exists a decrease in MH activity in the South Indian and South Pacific Oceans (despite having relatively lower values of χ) coincident with values of relatively large vertical wind shear (**Figure 58b**) and potential intensity.

Decreases in mid-Holocene activity in the South Indian Ocean are consistent with decrease in both spatial distributions of *GPI* and in its value integrated over the Southern Hemisphere in individual months (**Figure 59**). Decreases in genesis and track density in the western South Pacific also echo these decreases in local *GPI*, as well as slight increases in both *GPI* and track density of the eastern coast of South America (although while track density is larger in the MH here, there is little activity in either climate). Mid-Holocene TC activity is generally larger or similar in the Australian basin when compared to the 20th century, though many of these regions depict lower values of MH *GPI*.

The downscaled results respond as the changes in environmental factors predict: there is less activity in the western North Pacific in mid-Holocene where potential intensity is lower. Reasons that it is lower in CCSM4 may be from external forcing (Korty et al. 2012b) and from the response of ocean dynamics leading to a weaker east Pacific cold tongue (Karamperidou et al. 2015). In the eastern North Pacific, locally higher potential intensity values are consistent with the increase in activity; these are consistent with the western Hemisphere being closer to the tropical mean (smaller negative relative *SST*) in the mid-Holocene than in the 20th century. In this model, this resulted indirectly from the orbital forcing via its effect on thermocline depths in the Pacific (Karamperidou et al. 2015). We leave it for future work to see if this aspect of the response is robust across the ensemble of mid-Holocene experiments in PMIP3, or unique to CCSM4.

Explicitly Tracked Storms

Climate and tropical cyclone statistics for systems explicitly simulated and tracked in the 20th century and mid-Holocene experiments are shown in **Table 7**. The global and tropical averaged sea surface temperatures are within 1°C of each other, with higher temperatures in the 20th century. The major difference between the two periods again comes from shifts in the annual cycle, although the 20th century simulation period (1980-2005) is also slightly warmer than the conditions present in the Holocene prior to the industrial era.

The average number of mid-Holocene storms generated by CCSM4 per year is greater than in the 20th century (+4%), and this remains true if the weakest systems (those whose surface winds fail to reach tropical storm force at any point in their

	20C Total	**MH Total**	**20C NH**	**MH NH**	**20C SH**	**MH SH**
Tropical mean *SST* (°C)	**26.44**	25.56	**26.91**	26.01	**26.02**	25.15
Global mean *SST* (°C)	**11.02**	9.86	**9.41**	8.18	**12.38**	11.26
Number of TD	**20.91**	17.25	**13.20**	11.25	**7.71**	6.00
Number of TS	31.86	**37.00**	17.77	**18.78**	14.09	**18.22**
Number of H1	3.60	**4.63**	**1.74**	1.72	1.86	**2.91**
Number of H2	**0.91**	0.56	**0.57**	0.25	**0.34**	0.31
Number of Major Storms	**0.11**	0.00	0.00	0.00	**0.11**	0.00
Number of Total Storms	57.40	**59.44**	**33.28**	32.00	24.11	**27.44**
Number of TS+	36.49	**42.19**	20.08	**20.75**	16.40	**21.44**

Table 7 Explicitly tracked storms. CCSM4 20th century and mid-Holocene *SST* and storm counts by intensity. Bolded fonts indicate values that are higher between 20th century and MH climates. Tropical means are averaged over 30°S–0° in the Southern Hemisphere and 0°–30°N in the Northern Hemisphere.

lifetime) are excluded from the dataset. The 20th century experiment has a larger number of these weak tropical depressions in both hemispheres in addition to a larger number of storms with intensities H2 and greater, but it should be noted that there are very few cases of storms this strong in either climate.

We note that while the difference in the total number of storms per year between the two experiments is not statistically different (by use of Welch's *t*-test), if the tropical depressions are excluded from further consideration, the differences of the remaining subset (tropical storms and stronger) are statistically significant.

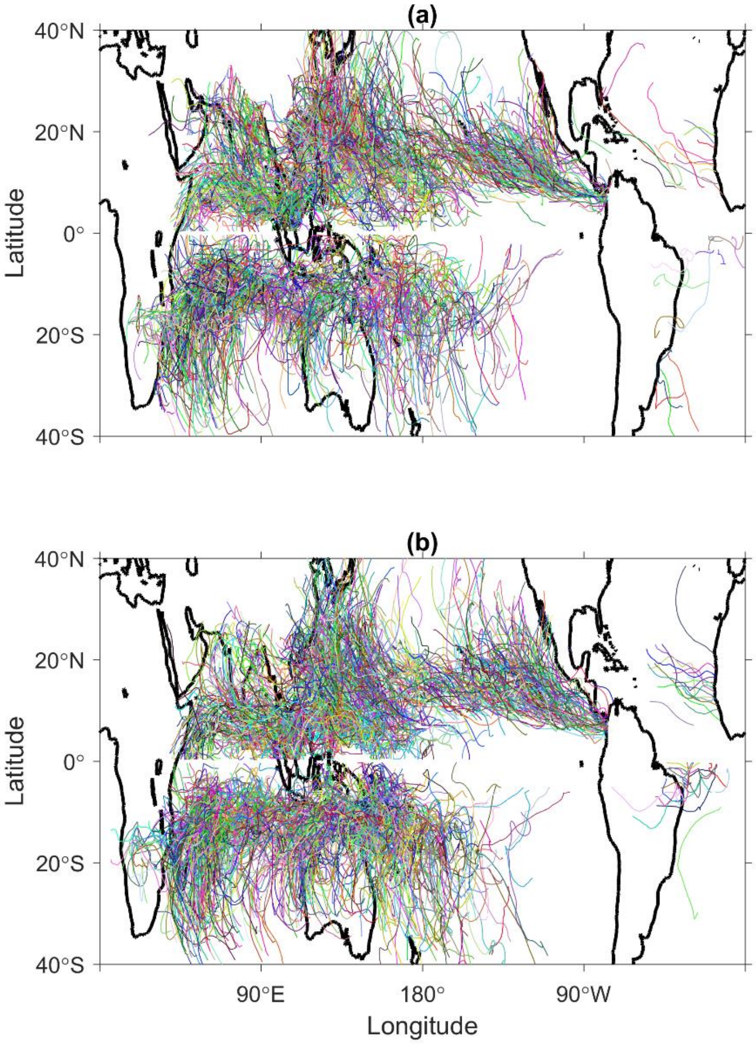

Figure 63 Explicitly resolved storms. Storm tracks for (a) 20th century and (b) mid-Holocene storms.

Figure 63 shows the tropical cyclone tracks for all of the cyclones tracked in both the 20th century and mid-Holocene experiments. The spatial distribution of the storms in the two experiments is similar, including the regions of genesis, their tracks

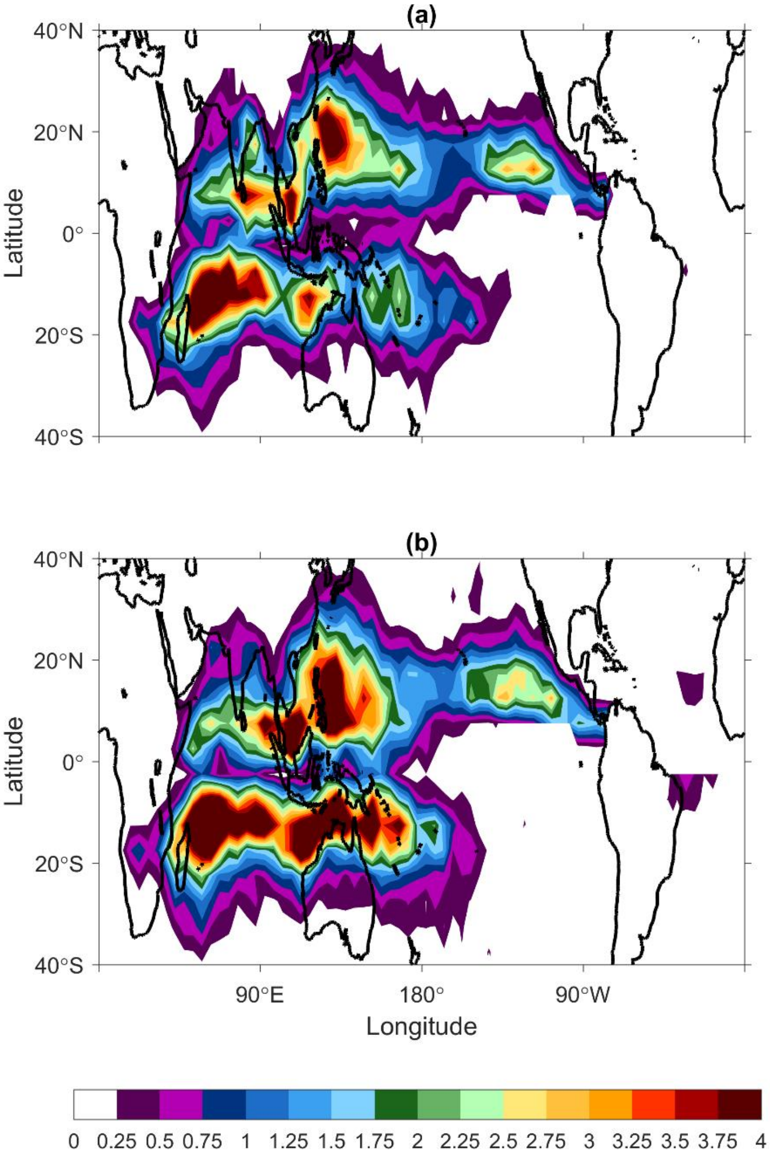

Figure 64 Explicitly resolved storms. Annual track density for (a) 20th century and (b) mid-Holocene storms. Values shown are in number of storm days per year.

and terminus, and the lack of Atlantic basin storms common in CCSM4. We followed 2,009 cyclones in the 20th century over 26 years of model output and 1,902 over 30 years of output in the MH experiment. We present the track densities that result from these cyclones (formed from 5° interpolated data as in the previous chapter for LGM experiments) in **Figure 64**, in an effort to more clearly see differences between the sets. While the two climates differ in the values of track density regionally, the regions where the highest densities exist do not change (i.e. western North Pacific, East Pacific, South Indian, and South Pacific basins). Although, there are broad similarities in the distributions of track density, there exists a much larger concentration of track density in the Australian basin the MH than what is found in the 20th century experiments. Track

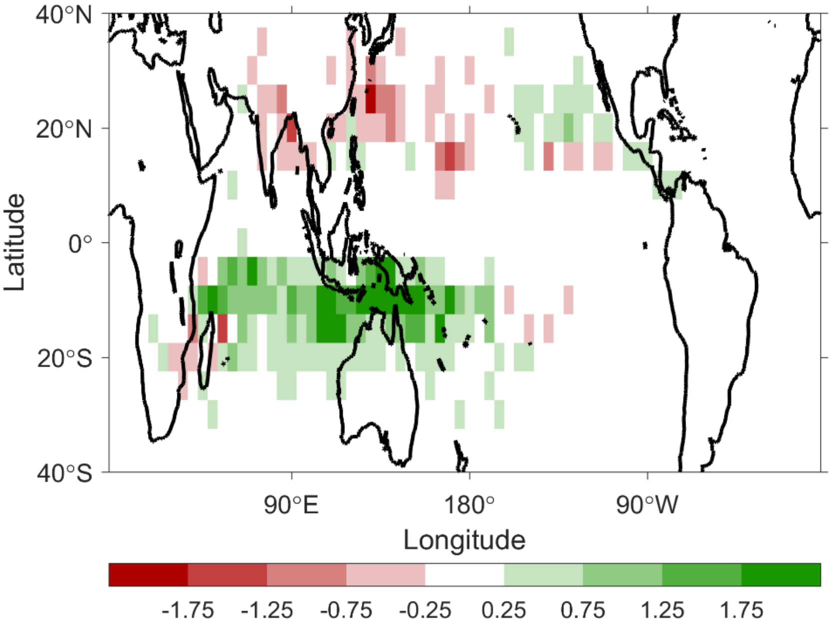

Figure 65 Explicitly resolved storms. Storm season (JASO in NH, JFMA in SH) difference in track density between mid-Holocene and 20th century. Values shown are in number of storm days per year.

densities are significantly lower at the mid-Holocene in the western North Pacific than in the 20th century.

Figure 65 shows the difference in track density between MH and 20th century during each hemispheres peak storm season. MH features a higher track density in the Southern Hemisphere than in the 20th century experiment, while the opposite is true in the Northern Hemisphere (20th century storms have a higher track density). This decline in Northern Hemisphere activity and increase in the Southern is consistent with the changes in environmental conditions that arose from increased stability during the Northern Hemisphere season in the PMIP2 ensemble members and the decrease during the Southern Hemisphere season (Korty et al. 2012b). Yet the increase in the Southern

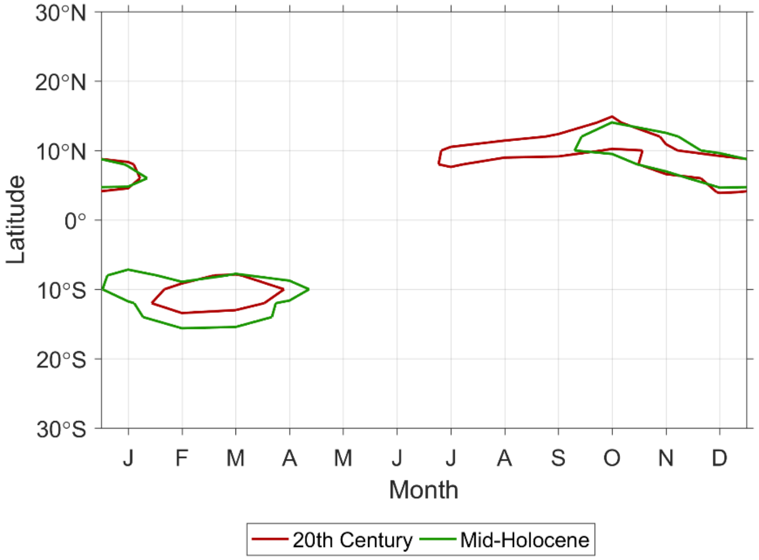

Figure 66 Explicitly resolved storms. Distribution of zonally summed genesis density by latitude and month that exceed 0.2 events per 1° latitude per year for 20th century (red) and mid-Holocene storms.

Hemisphere was not predicted by the environmental conditions from this model (CCSM4) itself (see **Figure 59c**); we revisit this point below.

As noted in the introduction of this chapter, the major change that we expect from mid-Holocene forcing is to distinct changes in the annual cycle in each hemisphere. If there is any influence of the TOA solar radiation anomalies on the climatology of TCs, do those changes match those predicted by the environmental factors?

Figure 66 shows the distribution of the zonally summed genesis density by latitude and month that exceed 0.2 events per 1° latitude per year. There are two findings of note in this plot: (1) significant genesis rates are delayed until autumn in the Northern Hemisphere of the mid-Holocene and (2) there is an expansion of the season and area of genesis farther poleward in the Southern Hemisphere in the mid-Holocene. The reduction of activity during peak months of July to September in the Northern Hemisphere at mid-Holocene is consistent with the response of the downscaling events examined in the last section, and it is consistent with the broadly less favorable environmental conditions in the model, particularly in the western North Pacific. The consistency of this Northern Hemisphere summer decline in both datasets, combined with its relationship to underlying changes in the large-scale environment, increases our confidence in the result. Koh and Brierley (2015) report that the environmental conditions are less favorable in the Northern Hemisphere in the ensemble of mid-Holocene simulations in PMIP3, as did Korty et al. (2012b) for the PMIP2 set.

The difference between the response of the vortices and of the downscaled set comes later in the year and during the Southern Hemisphere's season. **Figure 67** shows

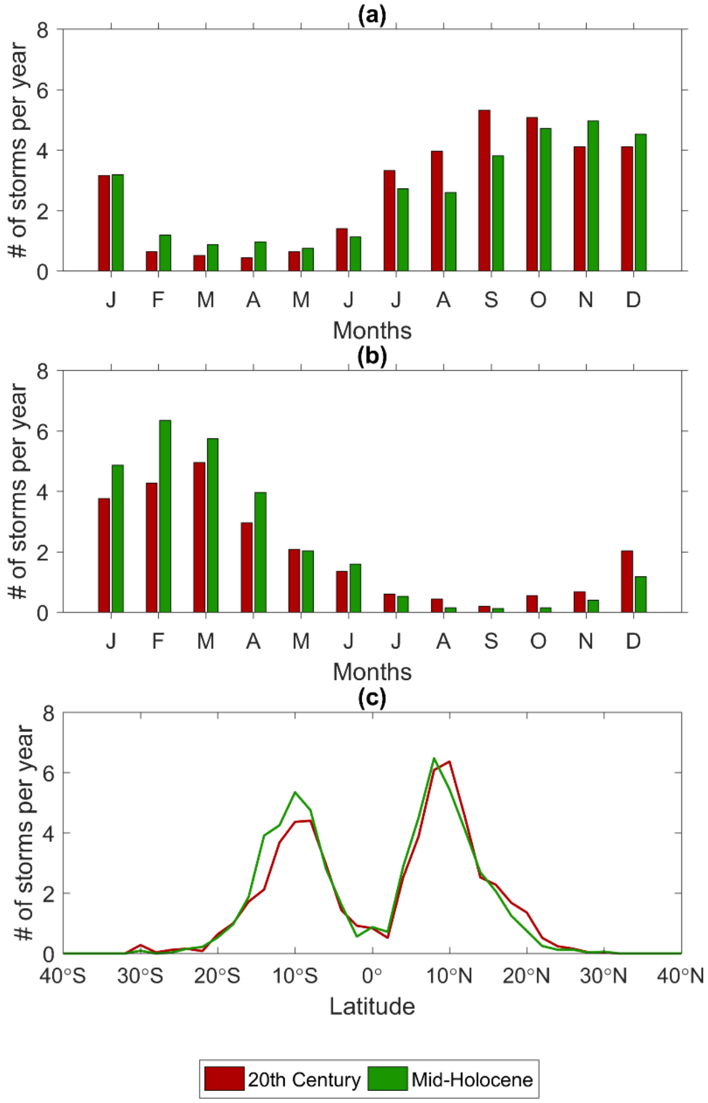

Figure 67 Explicitly resolved storms. Annual cycle of genesis in the (a) Northern and (b) Southern hemisphere for 20th century (red) and mid-Holocene storms. (c) Frequency and distribution of genesis by latitude per year.

the annual cycle of genesis in the Northern and Southern Hemisphere for 20th century and mid-Holocene simulated TCs. There is an important shift in the season in the Northern Hemisphere activity: genesis is lower at MH from June to September, but activity recovers in October and even increases in November and December. In addition, there are a greater number of mid-Holocene storms in the Southern Hemisphere during the peak 4-months of its storm season (January to April), which is in contrast to the declines seen in most basins with the downscaling set. **Figure 67c** depicts the frequency and distribution of genesis by latitude, and shows that the distribution between the two climates shifts southward in both hemispheres. Although the late season increases in Northern Hemisphere activity were a feature of the PMIP2 data Korty et al. (2012b) analyzed, it is not consistent with annual cycle constructed from (6) using the environmental factors from CCSM4 data (see **Figure 59c**). Below we examine the

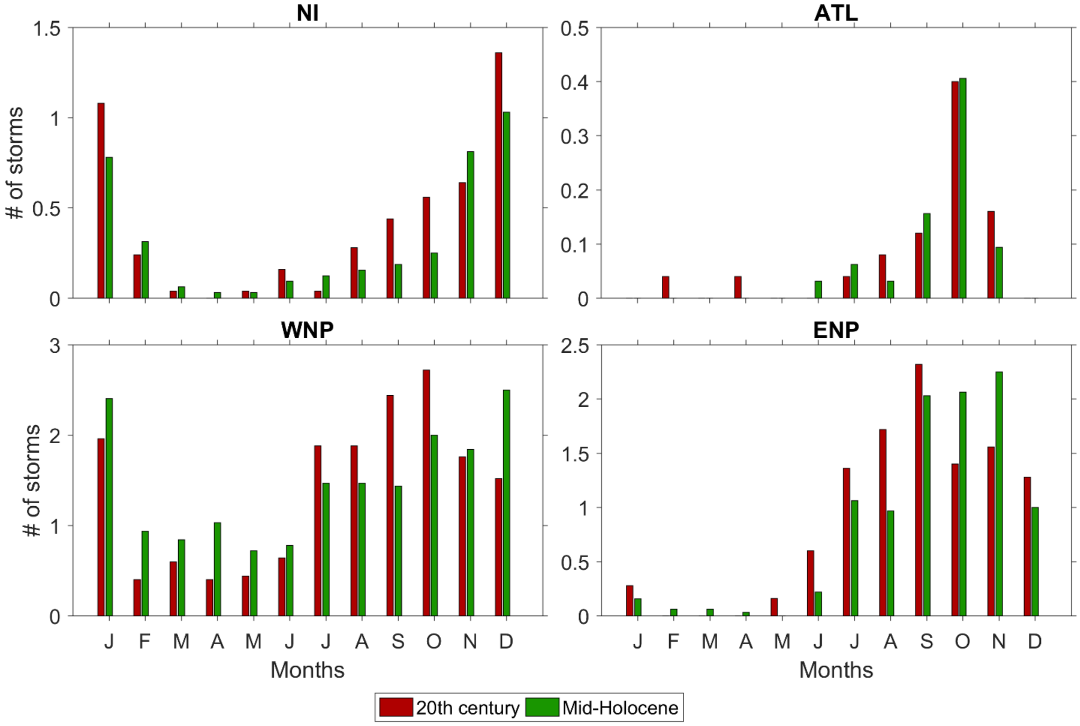

Figure 68 Explicitly resolved storms. Annual cycle of events for 20th century (red),and mid-Holocene (green) in (a) North Indian, (b) Atlantic, (c) western North Pacific, and (d) eastern North Pacific basins.

cycles by basin in more detail to identify the locations where the major contributions to the hemispheric and global totals originate.

Figure 68 shows the annual cycle of explicitly resolved storms in 20th century, and mid-Holocene experiments in Northern Indian, Atlantic, western North Pacific, and eastern North Pacific basins. One of the more apparent features of these plots is the relatively large number of off-season storms generated in the western North Pacific (January – May). This signature is unique to this basin, although large values are also seen in January and February in the North Indian Ocean. Generally the seasonality of 20th century storms (**Figure 67a**) is seen in each of the basins with the exception of the

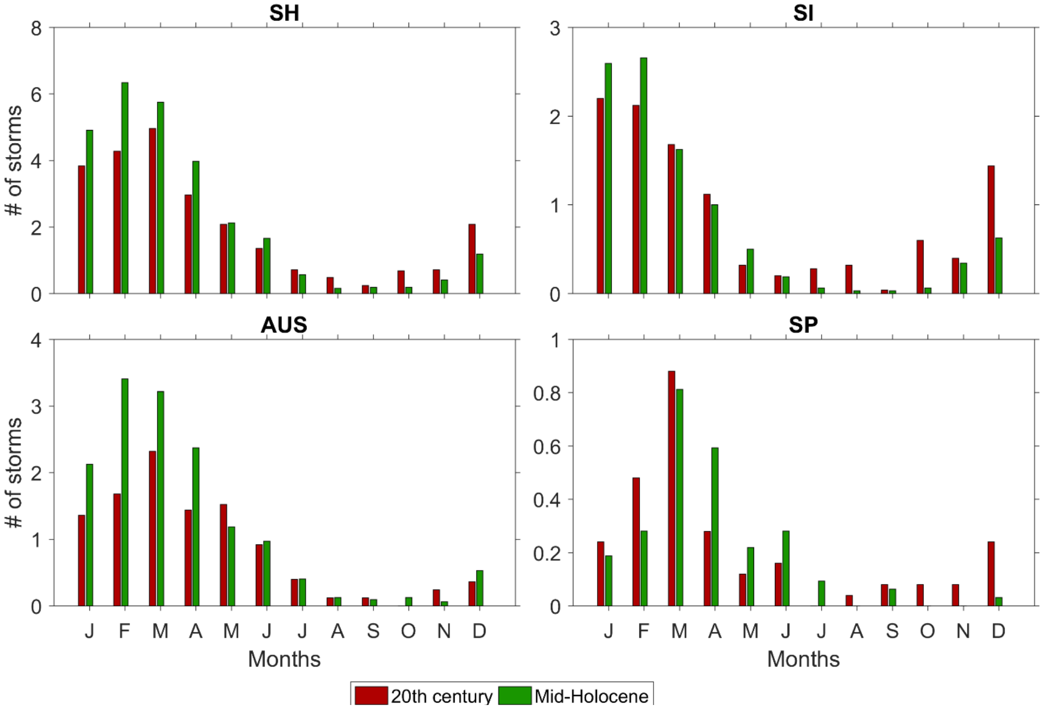

Figure 69 Explicitly resolved storms. Annual cycle of events for 20th century (red),and mid-Holocene (green) in (a) Southern Hemisphere, (b) South Indian, (c) Australian, and (d) South Pacific basins.

North Indian Ocean where peak values are reached in December. The other basins generate a peak number of storms in September or October, similar to our current climate. The mid-Holocene features peak storm counts occurring later in the season, predominantly in the western and eastern North Pacific basins (seasonality between the 20th century and mid-Holocene in the north Indian and Atlantic basins are similar).

Figure 69 shows the annual cycle of explicitly resolved storms in 20th century and mid-Holocene experiments in the Southern Hemisphere, South Indian, Australian, and South Pacific basins. The seasonality between each of the basins is similar. While the number of MH storms generated is higher in the peak TC season months (January – April), these increases can be only be attributed to the Australian and (to a lesser degree) South Indian Ocean basins, as the South Pacific generally featured relatively lower amounts of MH activity (with an exception of April). The number of off-season TCs is generally low in each of the Southern Hemisphere basins. While there are a few correlations between TC activity and the large-scale environment, (particularly in the 20th century WNP were values are predominantly higher during the peak TC season with coincident increases in 20th century PI, RH_{600}, and decreases in χ), the large scale environment does poorly in predicting changes in TC activity.

CHAPTER VII

SIMULATIONS OF VERY HOT CLIMATES[*]

The effects of a warmer climate state, relative to our current climate, on the environment is one of the currently most researched disciplines within our field. In particular, the sensitivity of tropical cyclones (and their consequent destruction) to an altered warmer climate state is of fundamental importance, as changes in intensity and of the frequency of high intensity events with warming have been reported in the historical record and in projections of the 21st century (e.g., Sobel et al. 2016; Walsh et al. 2016; Camargo and Wing 2016). In this Chapter, we apply Emanuel's downscaling storms technique to two global climate model simulations with very high carbon dioxide (CO_2) levels and very hot surface temperatures. Specifically, we examine how experiments with global levels of CO_2 that reach 8 (hereafter M-3) and 32 (hereafter M-5) times the preindustrial-era level of 280 ppm contrast with a contemporary experiment that uses 1990 levels of CO_2 (M-Ctrl).

We begin this chapter by presenting environmental variables that characterize each of these simulations, followed by an analysis of how the tropical cyclone climatology varies in these climates. We conclude with an analysis of the relationship between TC climatology and its environment in hotter climates, particularly in an expansion of the regions of favorable TC genesis and sustainment.

---

[*] Part of the data reported in this chapter is reprinted from: Korty, R. L., K. A. Emanuel, M. Huber, and R. A. Zamora, 2016: Tropical Cyclones Downscaled from Simulations with Very High Carbon Dioxide Levels. *Journal of Climate*, doi:10.1175/JCLI-D-16-0256. ©American Meteorological Society. Used with permission.

Properties of the Warmer Climate Simulations

The results presented here are generated from output of the final ~20 years of equilibrium simulations run with coarser spatial resolution (T42; ~2.5° horizontal resolution) of CAM3 than in earlier chapters, and with the atmospheric model coupled to

	M-Ctrl	**M-3**	**M-5**
Carbon Dioxide	355 ppmv	2240 ppmv	8960 ppmv
Tropical mean *SST*	25.7°C	30.1°C	40.1°C
Global mean *SST*	17.1°C	22.9°C	29.3°C
Annual Frequency	90.0	105 (*+16%*)	108 (*+20%*)
Number of TS	33.7	48.5 (*+44%*)	74.5 (*+121%*)
Number of H1	17.9	16.7 (*-7%*)	16.9 (*-6%*)
Number of H2	8.96	6.96 (*-22%*)	4.18 (*-53%*)
Number of H3	9.85	7.6 (*-23%*)	2.76 (*-72%*)
Number of H4	9.76	9.96 (*+2%*)	3.40 (*-65%*)
Number of H5	9.90	15.0 (*+52%*)	5.91 (*-40%*)
Mean storm lifetime	8.4 days	8.7 days (*+3%*)	9.8 days (*+17%*)

Table 8 M-Ctrl, M-3, and M-5 sea surface temperatures *SSTs*, storm counts by category, and mean storm lifetime. Italicized fonts indicate percentage change from M-Ctrl to M-3 and M-5 experiments

a slab ocean (Caballero and Huber 2010, 2013). (Recall that the downscaling method that is employed here simulates events in a separate hurricane model, and that it takes as input winds and thermodynamic properties from the global model being downscaled. It is not sensitive to the global model's resolution, unless that resolution affects the large-scale wind and temperature distributions used as input for the downscaling method [K.

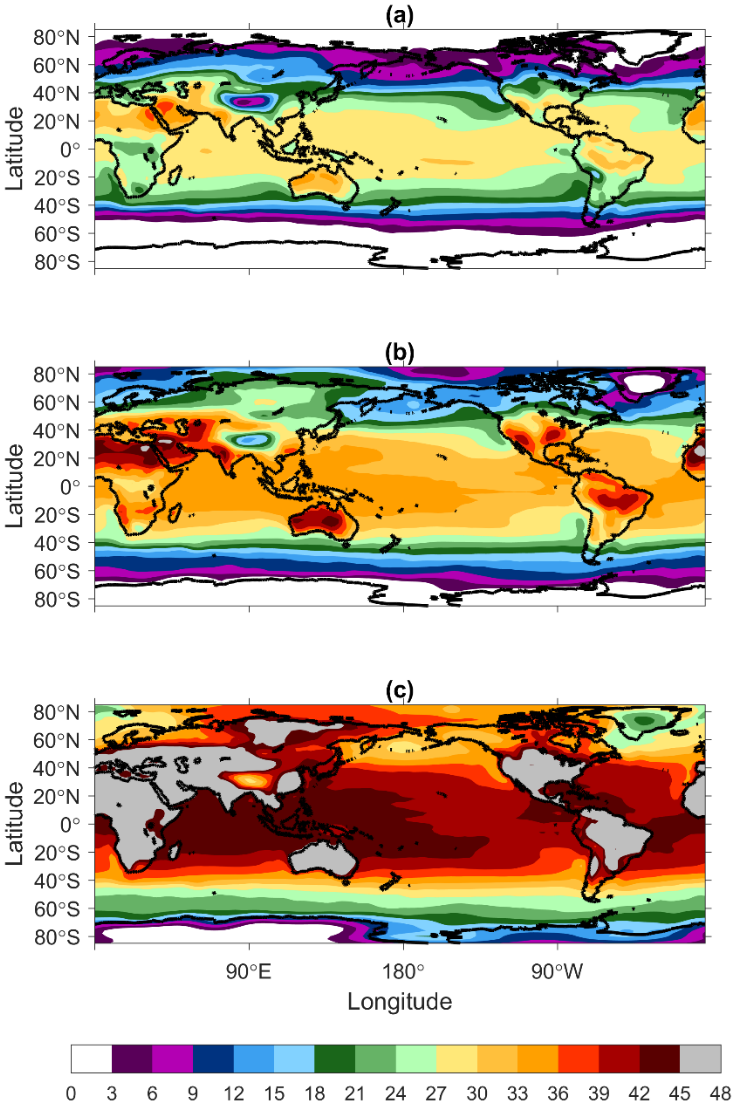

Figure 70 Annual peak surface temperatures T_{sfc} in (a) M-Ctrl, (b) M-3, and (c) M-5 climates. Values shown are in °C.

Emanuel, personal communication, 2016].) **Table 8** shows some of the properties of the CAM3 environment in the control climate and in simulations with CO_2 concentrations 2^3 and 2^5 times the level of the preindustrial era.

Figure 70 shows the annual peak surface temperatures for the three climates presented in **Table 8**. All three simulations use modern-day continental configurations. There are large increases in both ocean and land temperatures across each of the warming climates. Land regions show particularly large increases in surface temperatures, and in addition, the meridional temperature gradient weakens with climate as polar temperatures rise more rapidly. By the hottest case (M-5), air masses with convectively neutral lapse rates expand beyond the tropics into middle and even high latitudes (Zamora et al. 2016). The amount of warming is enhanced in particular in polar regions, where even in M-3, many of these regions have surface temperatures well above freezing, and in the hottest climate, features polar temperatures as high as 30°C warmer (although there remains an annual cycle to temperatures in the Arctic; annual means do not rise to the levels shown in **Figure 70**, which depicts the warmest month's temperature.)

We calculated the potential intensity (*PI*) in each of the three climate simulations, and the annual peak value of *PI* is shown in **Figure 71**. The highest values are confined to the tropics in M-Ctrl, but expand farther poleward (all the way to the Arctic in M-5) in higher CO_2 environments. This expansion is consistent with the results of Zamora et al. (2016), who showed expansions of air masses having convectively neutral lapse rates and overall tropical-like environmental conditions. It is also consistent with the

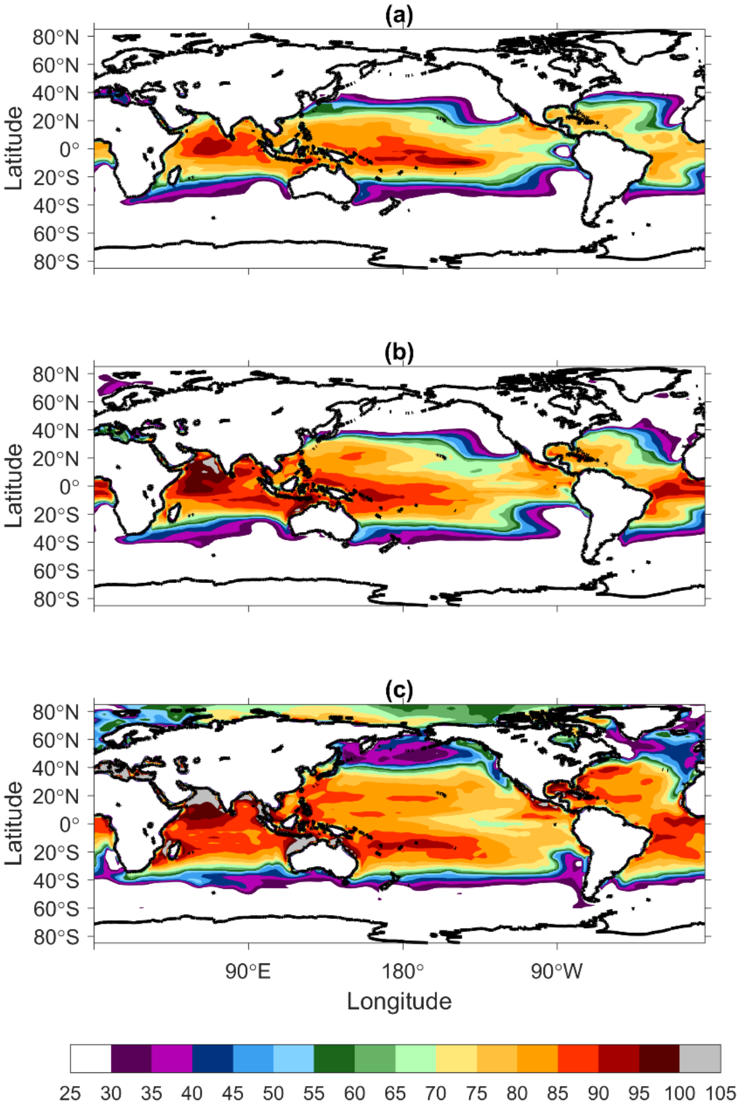

Figure 71 Annual peak potential intensity *PI* in (a) M-Ctrl, (b) M-3, and (c) M-5 climates. Values shown are in m/s.

numerous results reporting an expansion of the tropics in projections of the warmer 21st century: these include a widening of the Hadley circulation (Hu and Fu 2007; Seidel et al. 2008; Adam et al. 2014), a poleward shift in the region of the dry sinking branch of the Hadley cell and of middle latitude storm tracks (Barnes and Polvani 2013; Simpson et al. 2014), and in the lateral extent of low values of total column ozone found in the tropics (Hudson et al. 2006). Note that while *PI* expands to regions it does not currently exist, the values do not exceed levels found in lower latitudes today. *PI* values as reach as high as 95-100 m/s in M-Ctrl, but regions supporting 100 m/s are sparse even in the warmest climate (this issues is explored later in the chapter, and is consistent with the results of Emanuel and Sobel [2013] who showed that *PI* saturates in response to increasing CO_2 at temperatures not far above those of the modern climate).

Climatology of Downscaled Results

The data in **Table 8** report some properties of the downscaled storms. The annual frequency has been normalized to 90 storms per year for the control case, and each of the other simulations show increases over this amount. However, these increases are not homogenous across the distribution of storms by intensity. While, there are increases in tropical storms with warming (by 44% in M-3 and 121% in M-5 experiments), there number of category H1-H3 systems and of all tropical cyclones greater than TS decline. The number of the most intense H5 systems increases in M-3, but is lower in M-5. It is noteworthy, that while there are significant increases in the number of tropical storms with warming, the mean storm lifetime of all storms increases as well, possibly due to a higher expanse of regions favorable to TC growth and sustainment (this will be explored further in this Chapter).

Figure 72 shows the annual genesis density per year (each value shows the density of genesis in a 2° x 2° grid box). The M-Ctrl simulation shows genesis in regions similar to the historical record, with the largest concentration of storms in the western

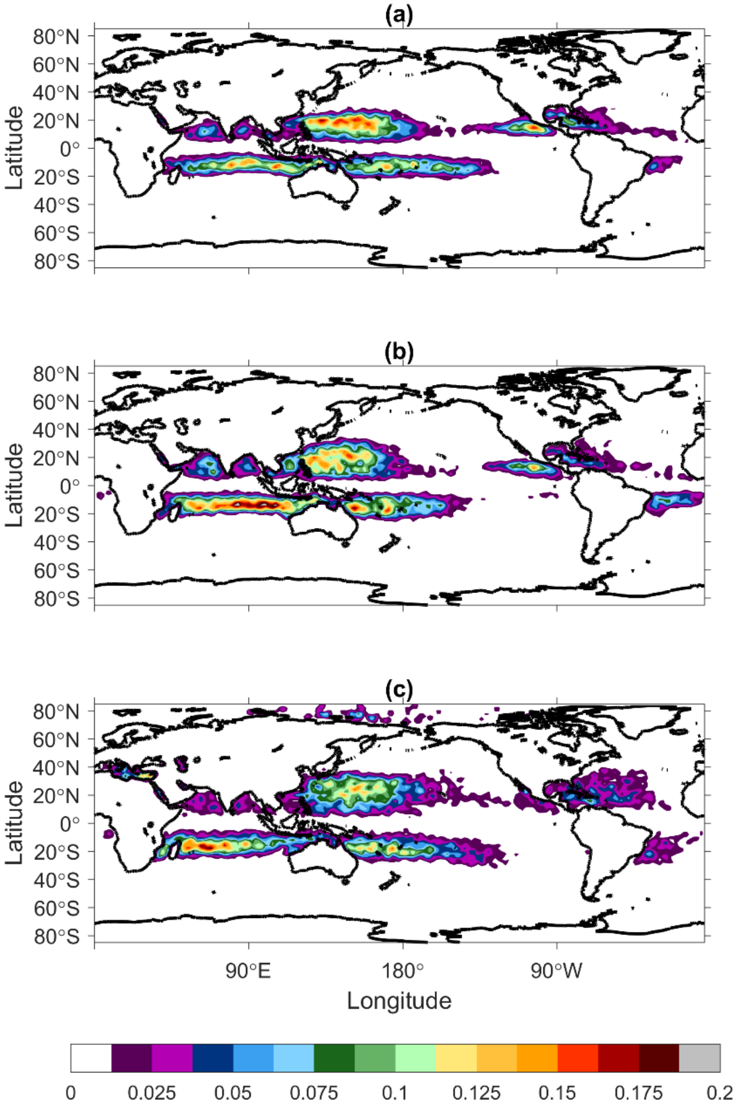

Figure 72 Annual genesis density in (a) M-Ctrl, (b) M-3, and (c) M-5 climates. Values shown are in number of storms per year per 2° by 2° grid box.

North Pacific basin. A major change in the two warmer climate simulations is an expansion of the genesis regions to higher latitudes (particularly in the Northern Hemisphere in latitudes greater than 20°N). Further, the hottest climate features some regions of genesis in the Arctic. Expansion of genesis territory in the Southern Hemisphere is less substantial, although total counts in M-3 have feature higher genesis in these regions. Likewise, **Figure 73** shows the annual track density per year in each climate. Similar to what is seen in genesis density, there is a poleward expansion of tracks with climate. In addition to shifts in formation regions, the track density increases from increases in the number of TCs and in their average storm lifetime with warming.

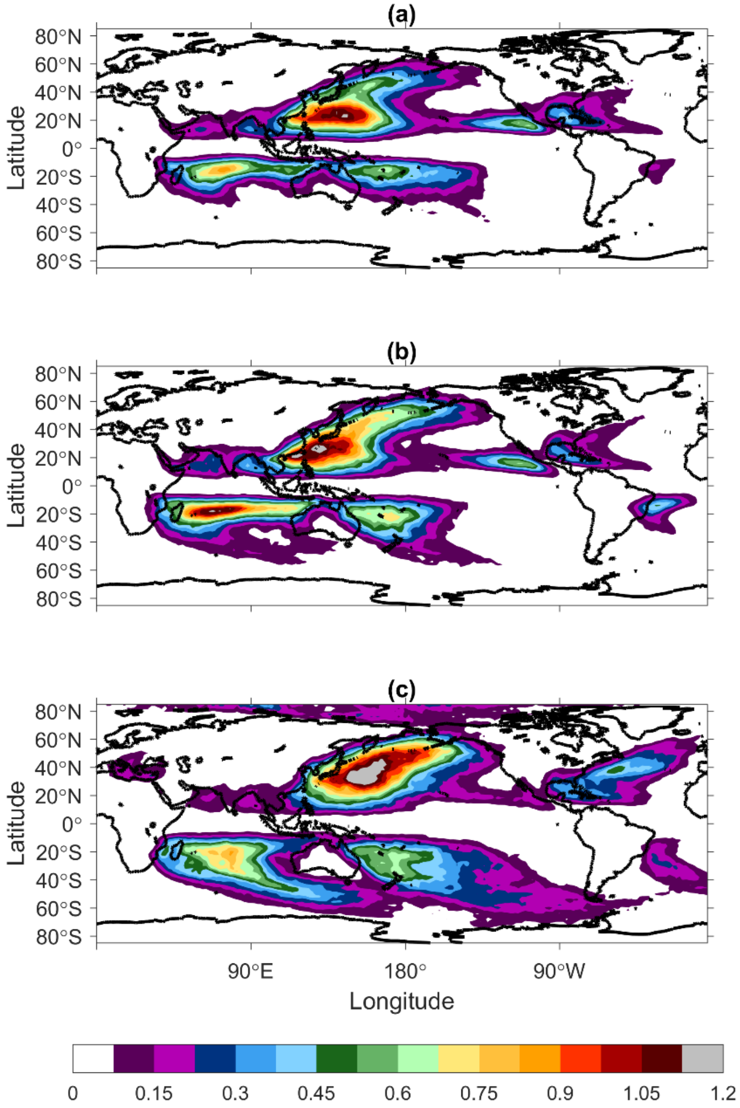

Figure 73 Annual track density in (a) M-Ctrl, (b) M-3, and (c) M-5 climates. Values shown are in number of storm days per year per 2° by 2° grid box.

Figure 74a shows the annually averaged cycle of genesis density by latitude and month that exceed 0.6 events per degree latitude area per year for M-Ctrl (black), M-3 (light blue), and M-5 (red) simulations. Each of the climates feature mostly similar seasons for genesis density, with changes occurring largely at the beginning of the season (start date of this level of activity in the Northern Hemisphere is delayed ~1

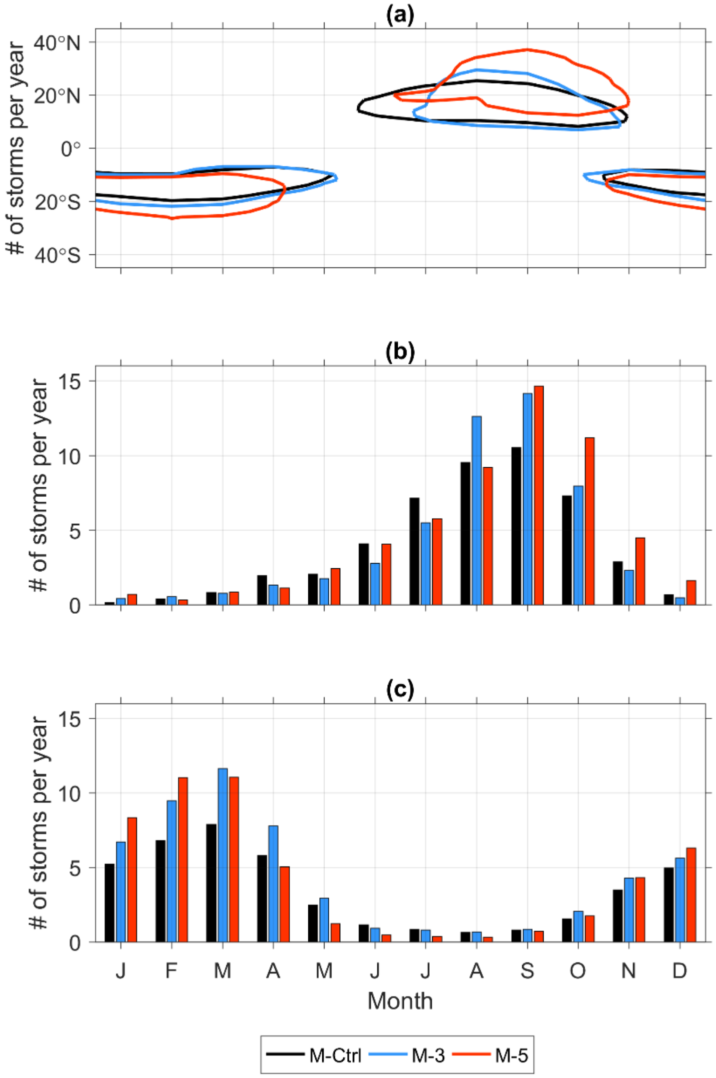

Figure 74 (a) Annually averaged cycle of genesis density by latitude and month that exceed 0.6 events per 1° latitude area per year in M-Ctrl (black), M-3 (light blue), and M-5 (red) simulations. (b) Annual cycle of genesis per year in the Northern Hemisphere. (c) As in (b), but for the Southern Hemisphere.

month in M-3 and M-5 simulations, and an earlier end in M-5 in the Southern Hemisphere), but the important change within the peak of the season is the poleward shift in activity. There is an expansion of the poleward boundary of significant genesis events in both climates and both hemispheres, but there is also a significant decline in low latitude activity of M-5 in the Northern Hemisphere. **Figure 74b and c** show the TC annual cycle in Northern and Southern Hemispheres, respectively. Counts for each of the simulations have a similar seasonal distribution (that follow the historical distribution,

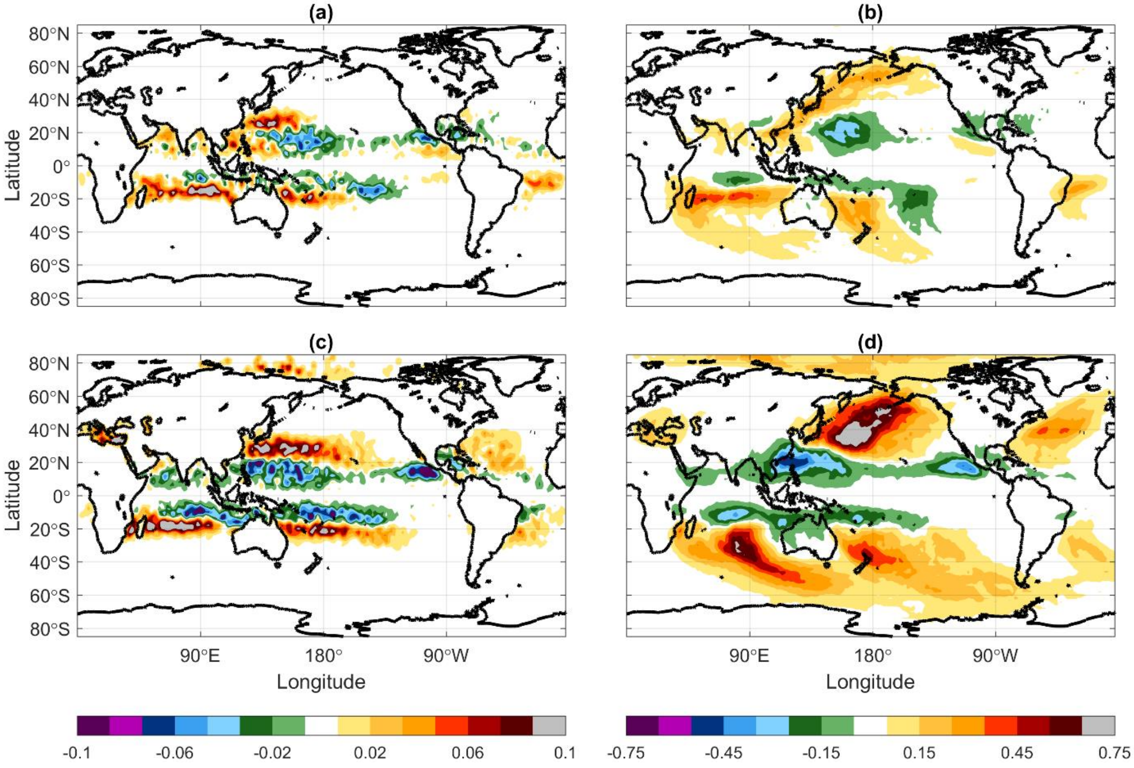

Figure 75 Difference in total genesis density between (a) M-3 and M-Ctrl, and (c) M-5 and M-Ctrl. Values shown are in number of storms per year per 2° by 2° grid box. (b, d) As in (a, c) but for track density. Values shown are in number of storm days per year per 2° by 2° grid box.

not shown), and feature generally amplified values in the peak storm season months in the warmer climate scenarios.

To explore the spatial changes in genesis and track density in greater detail, we show maps of differences in annual genesis and track density between the two warmer climates and M-Ctrl in **Figure 75**. **Figure 75a and b** capture the changes in the regions where TC genesis occurs between M-3 and M-Ctrl, showing a northwestward shift in genesis in the western North Pacific and a poleward shift in the Southern Hemisphere (note that there are declines in genesis activity on the equatorial side of the genesis band, and increases on the poleward side). These shifts in location result in substantial increases in tracks not only where storms form, but to the middle and higher latitudes where they travel. Genesis regions shift in both hemispheres, with large increases in activity along 20°S and 25°N.

Although storms still form in the deep tropics in M-5 there is a substantial decline in genesis (**Figure 75c**) and subsequent track density (**Figure 75d**) here. Genesis occurs at higher latitudes, expanding into subtropical regions (with some small amounts of activity even in the Arctic). While genesis expands poleward by 5°–10° latitude, the track density expands much further than this; it is substantially higher in middle and high latitudes of M-5 as systems live longer and travel farther into these regions of the planet.

Figure 76a shows the distribution of maximum intensity in each climate binned by Saffir-Simpson wind scale categories and one additional column showing the limited number of systems whose peak intensity exceeds 190 knots. (Note that to better show the smaller numbers for higher intensity categories, the axis showing annual frequencies is

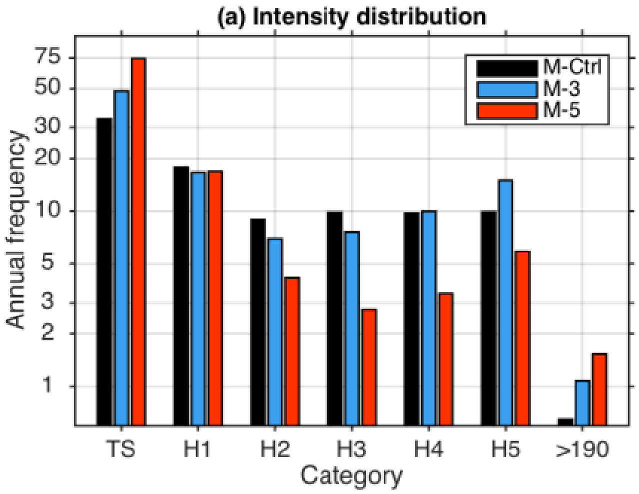
(a) Intensity distribution

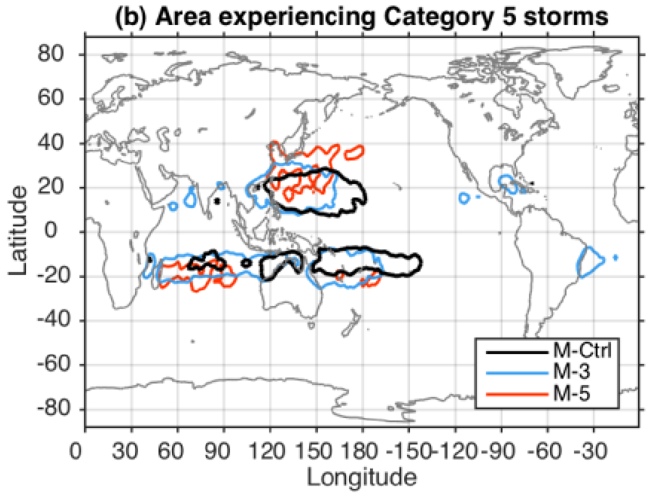
(b) Area experiencing Category 5 storms

Figure 76 (a) Annual frequency by Saffir-Simpson wind scale category with an additional column for events with peak intensities higher than 190 knots. (b) Area where track density of Category 5 winds (137 knots and higher) exceeds 0.02 storms per 1° latitude square.

on a logarithmic scale.) About one third of all events in M-Ctrl peak at tropical storm intensities, while about half of all hurricanes reach at least H3 status. In M-3 there is a very large increase in the number of tropical storms, mostly from an expansion of activity to higher latitudes, and a 52% increase in the number of H5 storms. The number of tropical storms in M-5 is 121% larger than in M-Ctrl, again primarily owing to a significant expansion of activity in subtropical, middle, and even some polar latitudes. But hurricanes of all intensities decline in frequency in M-5, with a 64% drop in the number of H2-H4 storms. There is a smaller drop in the number of H5 storms, but it still large (40%). On the other hand, the upper tail of the intensity distribution continues to become more populated in the warmer cases: the number of the most severe storms (those exceeding 190 knots) become 2.4 times more frequent than in the control case. The isolated number of events whose peak intensity exceeds 210 knots increases from about one storm every five years in M-Ctrl and M-3 to approximately one per year in M-5 (not shown). In fact, M-5 produced one hypercane (Emanuel 1987) that formed over the Caspian Sea and reached a peak velocity of 510 knots, the first observed in any set of events downscaled from global climate experiments (K. Emanuel, personal communication, 2016).

Figure 76b shows the area of significant track density for the subset of the event set with wind speed exceeding 137 knots, the threshold for H5. Importantly, the area experiencing such winds moves poleward with warming. The shift is not only in the poleward extent, but also in a poleward retreat from lower tropical latitudes, which experience a decline. This decline in low latitude activity drives down the global number of H5 events in M-5, and the environmental changes responsible for this are examined next. As noted earlier, the poleward expansion reported in this section is consistent with the changes in convectively neutral lapse rates reported in these simulations in Zamora et al. (2016). This expansion is also consistent with the findings of Kossin et al. (2014, 2016), who showed that the latitude at which TCs reach their peak intensity increases in both the historical record and in projections of the 21st century as the planet warms. The relationship between these changes and those of the underlying environmental factors are explored in the next section.

Environmental Factors

We now show that the changes in the TC climatology are related to the changes in the TC environmental factors. We examine the same set of parameters introduced in earlier chapters, namely changes in *PI*, the thermodynamic resistance parameter χ, and vertical wind shear. We show that the increases in genesis and track density reported above occur where aggregate conditions become more favorable, and that local decreases occur where aggregate measures become less favorable. In particular, *PI* does not increase much further from control values in the deep tropics despite significant warming, and robust shear and larger saturation deficits at these latitudes combine to reduce the favorability as measured by the ventilation index in the warmer climates (Tang and Emanuel 2010). On the other hand, although the highest *PI* values do not increase with warming (Emanuel and Sobel 2013), high values do expand poleward. This raises the favorability in the subtropics and middle latitudes, where genesis and track densities increase as reported above.

Figure 77 shows the difference in peak potential intensity between the hotter climate simulations and M-Ctrl. The largest values of *PI* expands to the subtropics in M-3, and even to some middle and polar latitudes in M-5, and this results in substantial

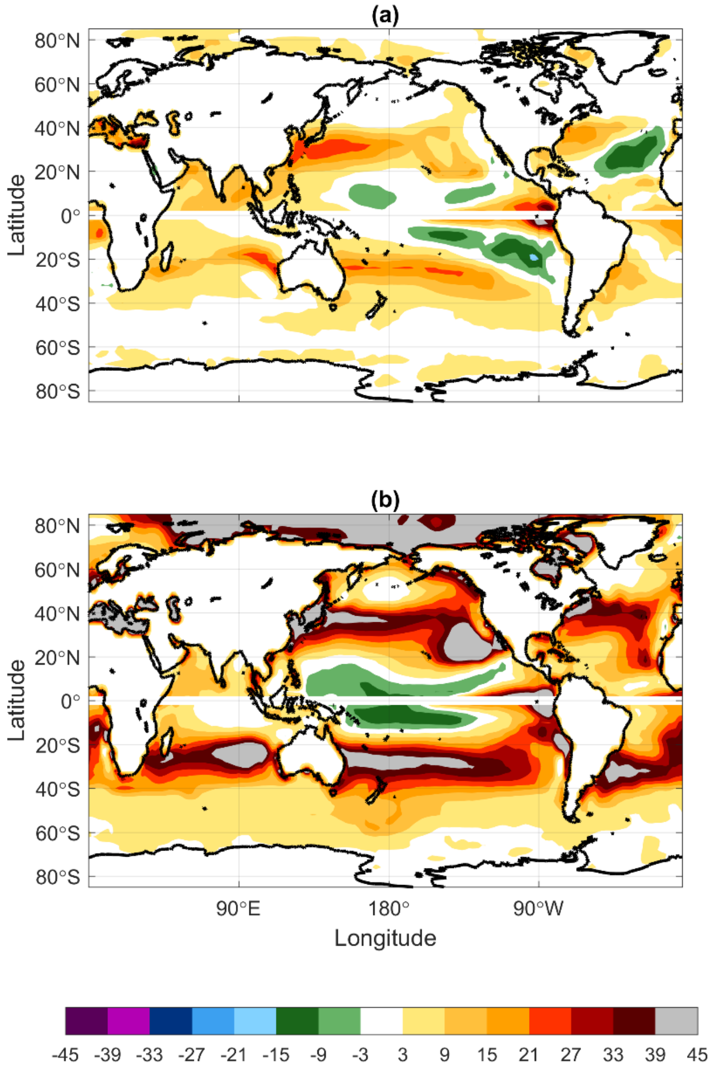

Figure 77 Difference in storm season (July – October in Northern Hemisphere and January – April in Southern Hemisphere) potential intensity *PI* between (a) M-3 and M-Ctrl, and (b) M-5 and M-Ctrl. Values shown are in m/s.

increases in *PI* values there. There are also some noteworthy changes at low latitudes: the Atlantic features values lower than elsewhere in the tropics in M-Ctrl, but they become as high as much of the western tropical Pacific in M-5. (In response, TC activity also increases by 50% in the Atlantic in M-5.) Values of *PI* across the Pacific near the equator are no larger in M-3 or M-5 than they were in M-Ctrl, and are even lower in parts of the central equatorial Pacific where *SSTs* rise less than the average over entire the tropics. This change in relative *SST* patterns is coincident with a decrease in *PI* over the central Pacific (Vecchi and Soden 2007). As noted earlier, Emanuel and Sobel (2013) found that *PI* saturates when surface warming results from increasing CO_2, because the net surface longwave flux approaches zero at sufficiently high temperature (O'Gorman and Schneider 2008). They showed that the expression for *PI* can be rewritten using the surface energy balance to show that *PI* is proportional to the sum of

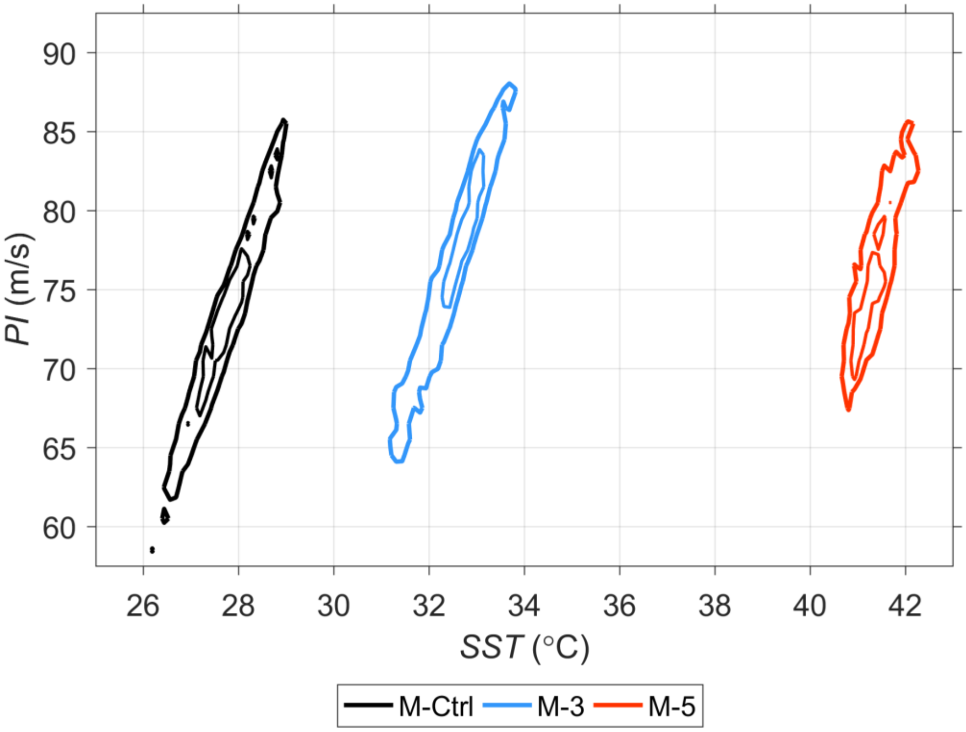

Figure 78 Bivariate joint distribution of potential intensity *PI* and sea surface temperature *SST*. Data is limited to the Northern Hemisphere storm season (July to October) in the 0° – 20°N latitudinal band for M-Ctrl (black), M-3 (light blue), and M-5 (red). Thick line denotes the 0.025 contour, while the thinner line denotes the 0.065 contour.

net solar and longwave fluxes at the surface. An upper bound is achieved as the net longwave flux tends to zero as CO_2 rises. **Figure 78** shows the joint distribution of *SST* and *PI* in the 0° – 20°N latitudinal band for each of the climates. This plot is limited to the months of peak storm season in the Northern Hemisphere (July – October). The data are binned by 0.125°C and 1 m/s spaced bins for *SST* and *PI*, respectively. The plot

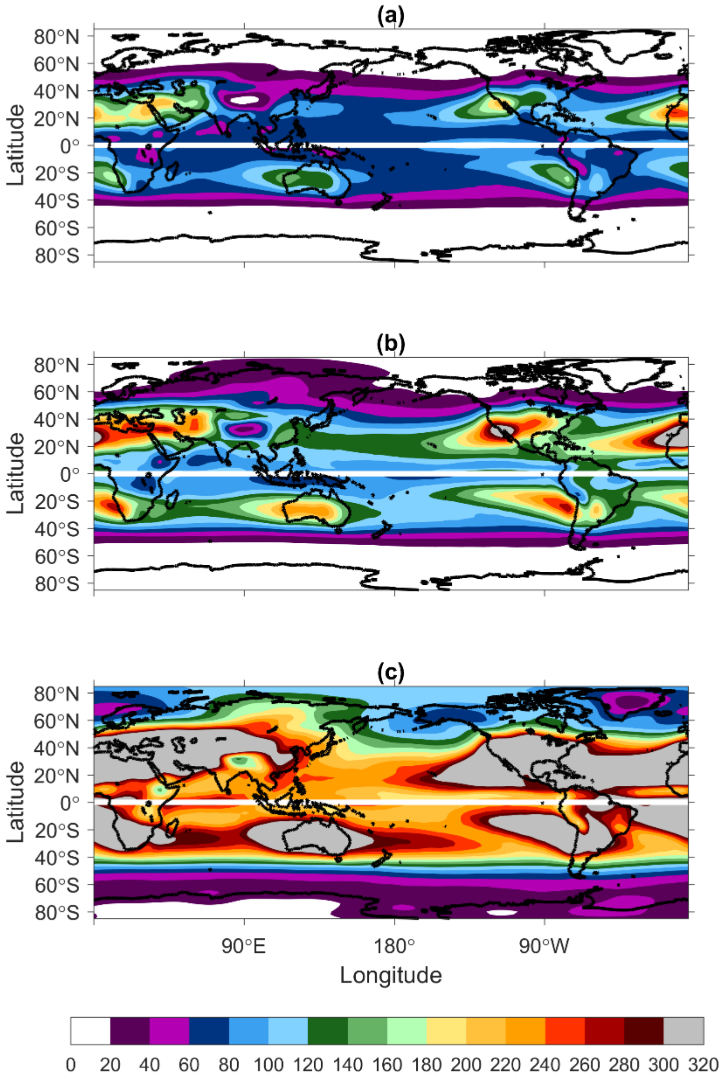

Figure 79 Storm season mean saturation deficit between (a) M-3 and M-Ctrl, and (b) M-5 and M-Ctrl. Values shown are in J.

shows how the values of *SST* vary with *PI*, particularly showing the saturation in *PI* values in the M-5 experiment despite the large warming.

A second important thermodynamic measure is the resistance parameter (χ), which compares the magnitude of the saturation deficit in the middle troposphere to the strength of surface fluxes that supply the moisture. This resistance parameter is tightly coupled to temperature, showing increases in colder climates (Chapter IV; Korty et al. 2012a), and decreases in warmer ones (Emanuel et al. 2008). The figures that follow show how these individual factors change in the increased CO_2 concentration scenarios.

Figure 79 shows the storm season mean saturation deficit (numerator of χ) for each of the climate experiments. While the regional distribution of the changes of its value with climate is similar, the saturation deficit greatly increases with warming climate. A growing saturation deficit makes it increasingly difficult for a tropical cyclone to receive a sufficient amount of moisture, unless the surface fluxes grow proportionally. **Figure 80** shows the strength of surface fluxes (denominator of χ) with climate. As with saturation deficit, which is also tightly coupled to temperature, surface fluxes increase in strength homogenously with increased warming. Stronger surface fluxes provide an increased supply of moisture for convection to carry to the mid-troposphere. However, the rate at which the value of the numerator χ increases greatly outpaces the change in the denominator. This results in larger values of χ in warmer climates (which mirrors the results showing decreases in colder climates).

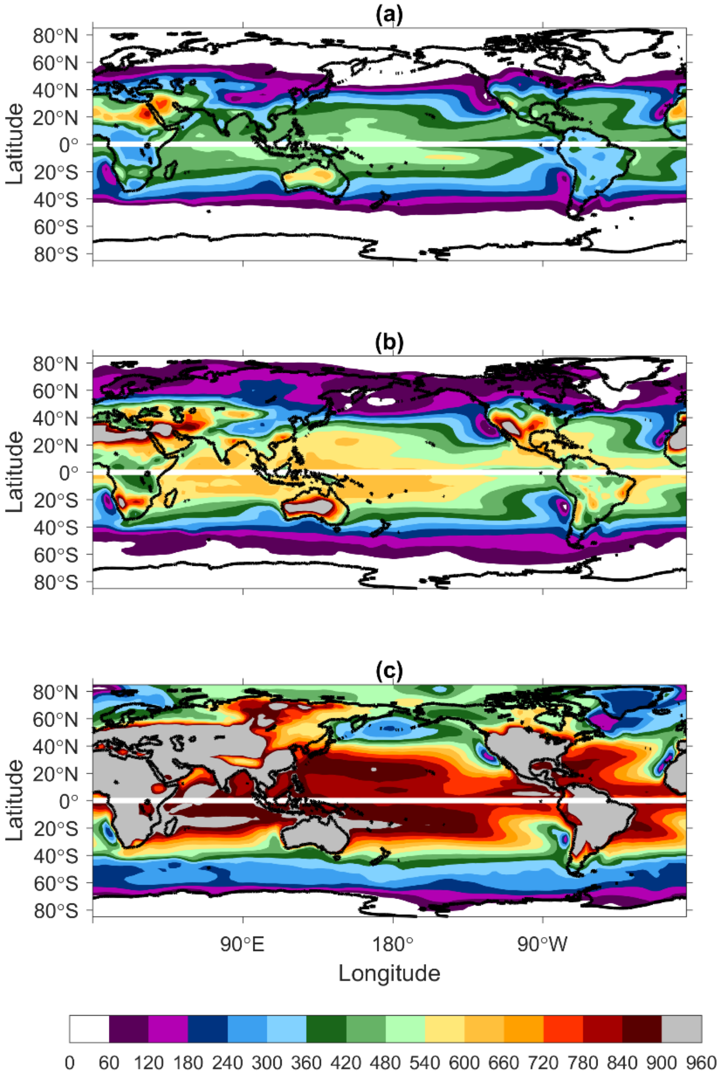

Figure 80 Storm season mean surface fluxes between (a) M-3 and M-Ctrl, and (b) M-5 and M-Ctrl. Values shown are in J.

Large increases with saturation deficit become particularly important in regions of large vertical wind shear as this will impede TC growth and sustainment via entrainment of dry environmental air. **Figure 81** shows the storm season mean magnitude of vertical wind shear for each of the climate experiments. Generally, the distribution of vertical wind shear in M-Ctrl shows lower values in the tropics, and

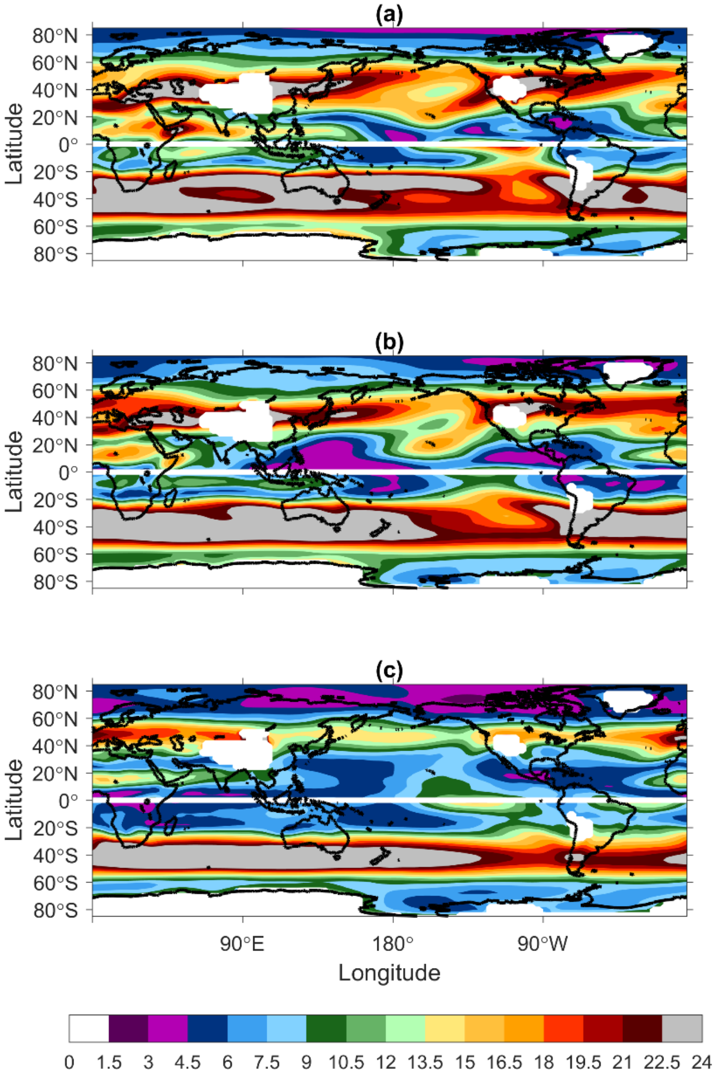

Figure 81 Difference in storm season mean vertical wind shear between (a) M-3 and M-Ctrl, and (b) M-5 and M-Ctrl. Values shown are in m/s.

increases at higher latitudes (particularly in the extratropics, as smaller values exist in polar regions). In the increased warming scenarios, the magnitude of vertical wind shear declines, particularly in the Northern Hemisphere. This decrease in wind shear in the midlatitudes is consistent with the increases in genesis density (**Figure 75**) and potential intensity. Similarly, large values of wind shear in the Southern Hemisphere persist in the

~30°S – 50°S latitudinal band, in the M-3 and M-5 simulations, coincident with a much smaller poleward shift in genesis (relative to the Northern Hemisphere).

However, Tang and Camargo (2014) showed that it is not a change in any single factor, but rather changes in their aggregate effects that matter. For example, the thermodynamic effects of a small increase in wind shear can be more than offset if relative humidity rose so that the air entrained by wind shear were not as dry. Similarly, even reductions in wind shear may not have a beneficial effect if the environmental air is that even low values of shear mix into a storm is hot and dry (Rappin et al. 2010). We combine these factors into a single parameter **(4**) that describes the inhibiting effects of ventilation (Λ). **Figure 82a and c** show the difference in $\log_{10}\Lambda$ of the warmer climate scenarios with M-Ctrl. (We again follow the practice introduced in Tang and Emanuel (2012) and show the logarithm of ventilation, to aid visualizing the changes.) Lower values of $\log_{10}\Lambda$ indicate a higher favorability of TC genesis, and as such positive values (redder colors) indicate regions of higher favorability in M-Ctrl. These plots show a general increase in favorability of $\log_{10}\Lambda$ at poleward latitudes in the warmer climate scenarios than in the control simulation.

To show the effectiveness of this parameter in predicting the changes found in TC activity, **Figure 82b and d** plot the change in total genesis density (as in **Figure 75a and c**, but restricted only to each hemispheres 4-month storm season), overlaid with the

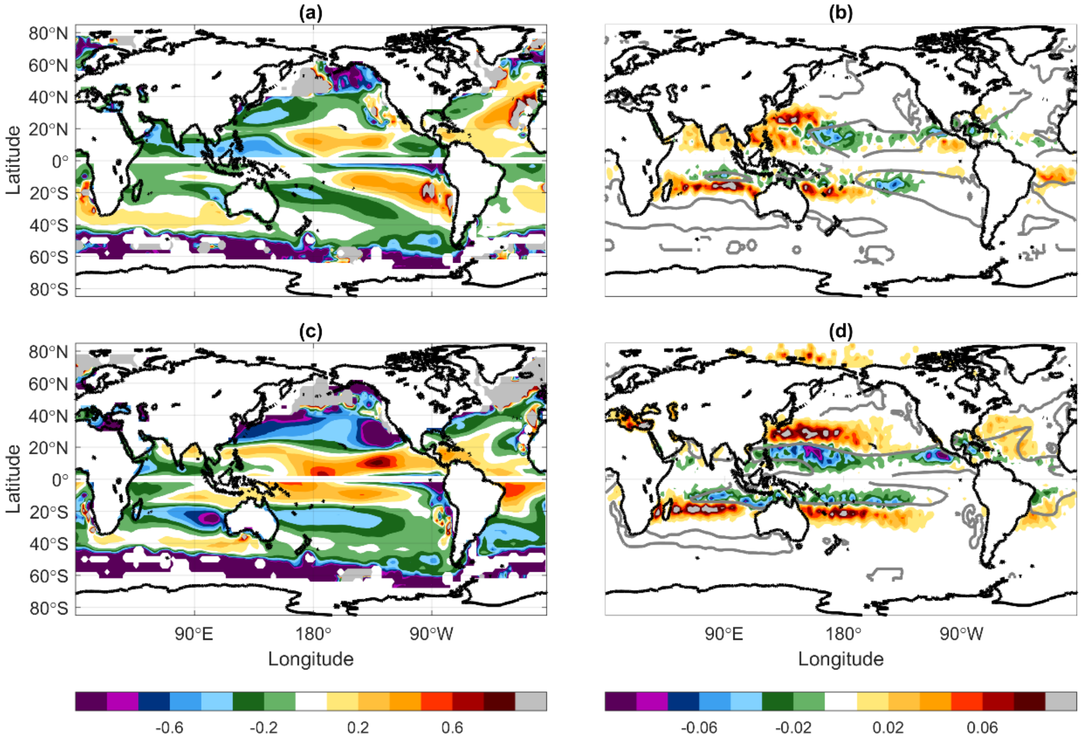

Figure 82 Difference in storm season mean $\log_{10}\Lambda$ between (a) M-3 and M-Ctrl, and (c) M-5 and M-Ctrl. Values shown are unitless. Difference in storm season genesis density between (b) M-3 and M-Ctrl, and (d) M-5 and M-Ctrl, overlaid (gray) with line of zero change in $\log_{10}\Lambda$.

0-valued contour (gray) in $\log_{10}\Lambda$ from **Figure 82a and c**, respectively. Regions where genesis density has decreased relative to M-Ctrl (generally near the equator), are likewise co-located with less favorable regions of $\log_{10}\Lambda$. Similarly, many of the regions showing increased genesis density in the hotter climate scenarios are highly correspondent to regions of favorable $\log_{10}\Lambda$. The rapid rise in saturation deficits with the extreme levels of warming in these simulations, coupled with *PI* that is no higher than in M-Ctrl leave the near equatorial latitudes less favorable in the warmer simulations. Evidence of this is seen in M-3 with the decrease in genesis density at the same low latitudes where ventilation increases, but it is especially prominent in M-5, where almost every point equatorward of 20° latitude in the Pacific shows both less favorable conditions and lower genesis density. Poleward of this region, where *PI* rises to high levels in the warmer climates, ventilation decreases and genesis density increases. Consistent with the findings of Kossin et al. (2014, 2016), we observe a significant poleward shift in TC activity in both climates with favorable conditions expanding to higher latitudes. The latitude at which storms reach their peak intensity moves 1.6° latitude poleward in M-3, and 7.4° latitude poleward in M-5. Additional analyses of these simulations can be found in Korty et al. (2016).

We summarize the major findings of this section as follows:

1. Tropical cyclone activity shifts to higher latitudes in simulations of increased CO_2 environments. The latitude at which storms reach their peak intensity shifts 1.6^o latitude poleward in M-3 and 7.4° latitude poleward in M-5.
2. Regions of high values *PI* expands poleward with regions of moist neutral lapse rates, which follow results from Zamora et al. (2016) showing that the tropics expand and areas of tropical-like conditions expand with it.
3. Although the larger values of *PI* become more widespread globally in warmer climate scenarios, the highest values of *PI* do not increase despite the significant amounts of warming. This is consistent with the results of Emanuel and Sobel (2013), who showed that *PI* saturates in response to increasing CO_2 levels.

4. Differences in large-scale environmental factors known to be favorable for TC genesis are strongly correlated with changes in the genesis density of simulated storms. As the environment becomes more favorable at higher latitudes, it can support genesis in regions our modern climate cannot support, and the better conditions permit storms to track farther poleward from there. In low latitudes, where *PI* remains unchanged, and saturation deficits increase exponentially with temperature, conditions become quite hostile in the hottest climate to TC activity. This is consistent with the results of Rappin et al. (2010) who showed that in the presence of any nonzero wind shear, it became more difficult—in some of the parameter space impossible—to spin up storms when such hot and dry environmental air surrounds a system.

CHAPTER VIII

SUMMARY

This thesis examined the relationship between simulated tropical cyclones and the large-scale environmental conditions that support them across a large range of climates. The simulated storms that we studied were generated via two techniques: explicitly tracking TC-like structures simulated directly in coarse global climate models, and a method that downscales global climate output to a higher resolution models able to resolve tropical cyclones. These techniques were applied to three climates in several models (but with a focus on NCAR’s Community Climate System Model) that uniquely differ from modern: the Last Glacial Maximum (a period 21,000 years ago when tropical surface temperatures were 2°–3°C colder, ice sheets covered many Northern Hemisphere continents, and concentrations of CO_2 were only 185 ppm), the mid-Holocene (a period 6,000 years ago with a climate very similar to preindustrial era but that received an increased amount of solar radiation during Northern Hemisphere summer due to variations in Earth’s orbit), and a suite of simulations that feature very hot surface conditions (forced by high levels of CO_2) applicable to hot periods like the Miocene and Eocene epochs. We compared the climatologies of these simulated tropical cyclones with large-scale environmental factors important for TC genesis and development to complement existing research on how TCs change in projections of 21st century warming, and to extend these to a wider understanding of how the properties very across different climates.

Storms generated from Emanuel's downscaled storms technique generally relate well to ventilation index or *GPI*. Many of the areas that featured increased TC activity exhibited favorable values in vertical wind shear, relative humidity, and potential intensity. Similarly, areas that showed decreased activity were coincident with unfavorable changes in the large-scale environment. While there existed some regions where this trend was not true, areas that featured large departures in values of environmental factors appeared to be able to capture corresponding changes in TC activity.

Intensity and genesis rise in simulations of warmer climates (although the hottest climate scenario shows that if conditions in the tropics become too harsh, this is not indefinite). Tropical cyclone activity shifted to higher latitudes with increased CO_2 and showed some subsequent decreases at lower latitudes. This expansion was consistent with findings from Zamora et al. (2016) that showed the expansion of tropical like conditions to higher latitudes than are found in our present climate. Regions exhibiting high values of potential intensity also expanded poleward, while the highest values did not show significant increases (barring a few regions such as the Indian Ocean) than what is found in our current climate. Differences in environmental factors predicted the expansion of genesis to higher latitudes particularly in the combination of factors (high *PI*, low V_{shear}, and low χ) that generate low values of ventilation index. Further, downscaled storms in LGM simulations in two (CCSM4 and MPI) of three models showed decreases in the total number of LGM storms, while the MRI model showed slight increases during the LGM. Despite an increased amount of LGM storms generated in MRI, each model showed decreases in the strongest (Category 4 and 5) storms and global power dissipation at the LGM. For the relevant range in this and coming centuries, however, number of intense storms and their average intensity would appear on track to increase with warming, should nature follow the behavior of the Emanuel downscaling.

Yet there are some important drawbacks to the technique (especially related to the question of frequency). Khairoutdinov and Emanuel (2013) showed that the distance separating storms in radiative-convective equilibrium simulations increases with warming, a possible constraint not included in Emanuel's downscaling technique. Further, changes in the climatology, location, etc. of precursor events may be important, and is not considered in the Emanuel method.

Explicitly resolved systems did not relate well to any common set of environmental factors. While tropical temperatures were much colder during the LGM, the environment could still foster TC genesis and sustainment, as potential intensity and relative sea surface temperatures exhibited large values in many basins. Distribution of genesis locations were restricted to regions of high potential intensity, large amount of moisture, and low vertical wind shear. However, when examining the difference in these factors between climates and comparing them to associated changes in genesis or track density, many regions do not exhibit favorable correlations.

In addition, the changes in climate are potentially sensitive to the inclusion of the weakest systems, which differed when thresholds were tightened. The total counts of explicitly tracked storms showed decreases during the much colder LGM when compared to the 20th century control. However, when excluding the weakest intensity storms (tropical depressions), the number of storms during the LGM was larger than in the 20th century. Through a series of sensitivity tests on the thresholds that determine a tropical cyclone in the algorithm (exceedance of vertically integrated temperature anomaly, surface wind speed, pressure, and low-level vorticity), it was found that the resultant TC climatology was sensitive to the handling of weak systems. Altering the threshold that must be exceeded for surface wind speed of an initial vortex, by making it tighter, resulted in a reversal in the sign of the LGM-20C difference in total counts (by as little as 20%). This underscored the importance to better understand the sensitivity of these techniques to chosen thresholds and model resolution, particularly for the weakest storms generated. Still, broadly speaking, there are some common results: fewer Northern Hemisphere storms at mid-Holocene the number of the strongest systems at LGM capable of being resolved was lower. Storms in the LGM form in the same regions as the downscaled method, and during the same season.

All of this is consistent with the recent reviews by Sobel et al. (2016) showing higher confidence in the results that intensity rises with warming. But that changes in frequency were less certain, certainly partly because we lack a theoretical understanding of what controls frequency in the modern climate.

REFERENCES

Adam, O., T. Schneider, and N. Harnik, 2014: Role of Changes in Mean Temperatures versus Temperature Gradients in the Recent Widening of the Hadley Circulation. *Journal of Climate*, **27**, 7450-7461.

Barnes, E. A., and L. Polvani, 2013: Response of the Midlatitude Jets, and of Their Variability, to Increased Greenhouse Gases in the CMIP5 Models. *Journal of Climate*, **26**, 7117-7135.

Bell, G. D., M. S. Halpert, R. C. Schnell, R. W. Higgins, J. Lawrimore, V. E. Kousky, R. Tinker, W. Thiaw, M. Chelliah, and A. Artusa, 2000: Climate Assessment for 1999. *Bulletin of the American Meteorological Society*, **81**, S1-S50.

Bellouin, N., O. Boucher, J. Haywood, C. Johnson, A. Jones, J. Rae, and S. Woodward, 2007: Improved Representation of Aerosols for HadGEM2. *Hadley Centre Technical Note*, **73**, 43.

Bengtsson, L., H. Böttger, and M. Kanamitsu, 1982: Simulation of Hurricane-Type Vortices in a General Circulation model. *Tellus,* **34**, 440-457.

Bengtsson, L., K. I. Hodges, and M. Esch, 2007: Tropical Cyclones in a T159 Resolution Global Climate Model: Comparison with Observations and Re-analyses. *Tellus A*, **59**, 396-416.

Berger, A., 1978: Long-term Variations of Daily Insolation and Quaternary Climatic Changes. *Journal of Atmospheric Sciences,* **35**, 2362-2367.

Bister, M., and K. A. Emanuel, 1998: Dissipative Heating and Hurricane Intensity. *Meteorology and Atmospheric Physics*, **65**, 233-240.

——, 2002: Low Frequency Variability of Tropical Cyclone Potential Intensity 1. Interannual to Interdecadal Variability. *Journal of Geophysical Research: Atmospheres*, **107**, 2156-2202.

Braconnot, P., S. P. Harrison, M. Kageyama, P. J. Bartlein, V. Masson-Delmotte, A. Abe-Ouchi, B. Otto-Bliesner, and Y. Zhao, 2012: Evaluation of Climate Models Using Palaeoclimatic Data. *Nature Climate Change*, **2**, 417-424.

Braconnot, P., B. Otto-Bliesner, S. Harrison, S. Joussaume, J. Y. Peterchmitt, A. Abe-Ouchi, M. Crucifix. E. Driesschaert, Th. Fichefet, C. D. Hewitt, M. Kageyama, A. Kitoh, A. Laine, M.-F. Loutre, O. Marti, U. Merkel, G. Ramstein, P. Valdes, S. L. Weber, Y. Yu, and Y. Zhao, 2007: Results of PMIP2 Coupled Simulations of the Mid-Holocene and Last Glacial Maximum - Part 1: Experiments and Large-scale Features. *Climate of the Past*, **3**, 261-277.

Broccoli, A. J., 2000: Tropical Cooling at the Last Glacial Maximum: An Atmosphere–Mixed Layer Ocean Model Simulation. *Journal of Climate*, **13**, 951-976.

Bruyère, C. L., G. J. Holland, and E. Towler, 2012: Investigating the Use of a Genesis Potential Index for Tropical Cyclones in the North Atlantic Basin. *Journal of Climate*, **25**, 8611-8626.

Bye, J., and K. Keay, 2008: A New Hurricane Index for the Caribbean. *Interciencia*, **33**, 556-560.

Caballero, R., and M. Huber, 2010: Spontaneous Transition to Superrotation in Warm Climates Simulated by CAM3. *Geophysical Research Letters*, **37**, L11701.

——, 2013: State-dependent Climate Sensitivity in Past Warm Climates and its Implications for Future Climate Projections. *Proceedings of the National Academy of Sciences*, **110**, 14162-14167.

Camargo, S. J., 2013: Global and Regional Aspects of Tropical Cyclone Activity in the CMIP5 Models. *Journal of Climate*, **26**, 9880-9902.

——, 2014: Tropical Cyclones, Western North Pacific Basin, in "State of the Climate in 2013". *Bulletin of the American Meteorological Society*, **95**, S92-S94.

Camargo, S. J., and S. E. Zebiak, 2002: Improving the Detection and Tracking of Tropical Cyclones in Atmospheric General Circulation Models. *Weather and Forecasting*, **17**, 1152-1162.

Camargo, S. J., and A. H. Sobel, 2005: Western North Pacific Tropical Cyclone Intensity and ENSO. *Journal of Climate*, **18**, 2996-3006.

Camargo, S. J., and A. A. Wing, 2016: Tropical Cyclones in Climate Models. *Wiley Interdisciplinary Reviews Climate Change*, **7**, 211-237.

Camargo, S. J., A. H. Sobel, A. G. Barnston, and K. A. Emanuel, 2007: Tropical Cyclone Genesis Potential Index in Climate Models. *Tellus A*, **59**, 428-443.

Collins, W., N. Bellouin, M. Doutriaux-Boucher, N. Gedney, P. Halloran, T. Hinton, J. Hughes, C. D. Jones, M. Joshi, S. Liddicoat, G. Martin, F. O’Connor, J. Rae, C. Senior,

S. Sitch, I. Totterdell, A. Wiltshire, and S. Woodward, 2011: Development and Evaluation of an Earth-system Model–HadGEM2. *Geoscientific Model Development*, **4**, 1051-1075.

DeMaria, M., 1996: The effect of Vertical Shear on Tropical Cyclone Intensity Change. *Journal of Atmospheric Sciences*, **53**, 2076-2088.

DeMaria, M., J. A. Knaff, and B. H. Connell, 2001: A Tropical Cyclone Genesis Parameter for the Tropical Atlantic. *Weather and Forecasting*, **16**, 219-233.

Donnelly, J. P., 2005: Evidence of Past Intense Tropical Cyclones from Backbarrier Salt Pond Sediments: A Case Study from Isla de Culebrita, Puerto Rico, USA. *Journal of Coastal Research*, **42**, 201-210.

Dwyer, J. G., S. J. Camargo, A. H. Sobel, M. Biasutti, K. A. Emanuel, G. A. Vecchi, M. Zhao, and M. K. Tippett, 2015: Projected Twenty-First-Century Changes in the Length of the Tropical Cyclone Season. *Journal of Climate*, **28**, 6181-6192.

Elsner, J. B., J. P. Kossin, and T. H. Jagger, 2008: The Increasing Intensity of the Strongest Tropical Cyclones. *Nature*, **455**, 92-95.

Emanuel, K. A., 1987: The Dependence of Hurricane Intensity on Climate. *Nature*, **326**, 483-485.

——, 1994: *Atmospheric Convection.* Oxford University Press on Demand.

Emanuel, K., 2005: Increasing Destructiveness of Tropical Cyclones over the Past 30 years. *Nature,* **436**, 686-688.

——, 2006: Climate and Tropical Cyclone Activity: A New Model Downscaling Approach. *Journal of Climate*, **19**, 4797-4802.

——, 2010: Tropical Cyclone Activity Downscaled from NOAA-CIRES Reanalysis, 1908–1958. *Journal of Advances in Modeling Earth Systems*, **2**, 1-12.

Emanuel, K. A., 2013: Downscaling CMIP5 Climate Models Shows Increased Tropical Cyclone Activity over the 21st Century. *Proceedings of the National Academy of Sciences*, **110**, 12219-12224.

Emanuel, K. A., and D. S. Nolan, 2004: Tropical Cyclone Activity and the Global Climate System. *Preprints, 26th Conf. on Hurricanes and Tropical Meteorology, Miami, FL, Amer. Meteor. Soc.*

Emanuel, K., and A. Sobel, 2013: Response of Tropical Sea Surface Temperature, Precipitation, and Tropical Cyclone-related Variables to Changes in Global and Local Forcing. *Journal of Advances in Modeling Earth Systems*, **5**, 447-458.

Emanuel, K. A., R. Sundararajan, and J. Williams, 2008: Downscaling Hurricane Climatologies from Global Models and Re-analyses. *28th Conference on Hurricanes and Tropical Meteorology. Orlando*.

Emanuel, K., C. DesAutels, C. Holloway, and R. Korty, 2004: Environmental Control of Tropical Cyclone Intensity. *Journal of Atmospheric Sciences*, **61**, 843-858.

Emanuel, K., K. Oouchi, M. Satoh, H. Tomita, and Y. Yamada, 2010: Comparison of Explicitly Simulated and Downscaled Tropical Cyclone Activity in a High-resolution Global Climate Model. *Journal of Advances in Modeling Earth Systems*, **2**, 1-9.

Fedorov, A. V., C. M. Brierley, and K. Emanuel, 2010: Tropical Cyclones and Permanent El Niño in the Early Pliocene Epoch. *Nature*, **463**, 1066-1070.

Ferreira, R. N., and W. H. Schubert, 1999: The Role of Tropical Cyclones in the Formation of Tropical Upper-tropospheric Troughs. *Journal of Atmospheric Sciences*, **56**, 2891-2907.

Giorgetta, M. A., J. Jungclaus, C. H. Reick, S. Legutke, J. Bader, M. Bottinger, V. Brovkin, T. Crueger, M. Esch, and K. Fieg, 2013: Climate and Carbon Cycle Changes from 1850 to 2100 in MPI-ESM Simulations for the Coupled Model Intercomparison Project Phase 5. *Journal of Advances in Modeling Earth Systems*, **5**, 572-597.

Gray, W. M., 1968: Global View of the Origin of Tropical Disturbances and Storms. *Monthly Weather Review*, **96**, 669-700.

Grodsky, S. A., J. A. Carton, S. Nigam, and Y. M. Okumura, 2012: Tropical Atlantic Biases in CCSM4. *Journal of Climate*, **25**, 3684-3701.

Hodges, K. I., 1994: A General Method for Tracking Analysis and Its Application to Meteorological Data. *Monthly Weather Review*, **122**, 2573-2586.

——, 1995: Feature Tracking on the Unit Sphere. *Monthly Weather Review*, **123**, 3458-3465.

Holland, G., and C. L. Bruyère, 2014: Recent Intense Hurricane Response to Global Climate Change. *Climate Dynamics*, **42**, 617-627.

Horn, M., K. Walsh, M. Zhao, S. J. Camargo, E. Scoccimarro, H. Murakami, H. Wang, A. Ballinger, A. Kumar, D. A. Shaevitz, J. A. Jonas, and K. Oouchi, 2014: Tracking Scheme Dependence of Simulated Tropical Cyclone Response to Idealized Climate Simulations. *Journal of Climate*, **27**, 9197-9213.

Hu, Y., and Q. Fu, 2007: Observed Poleward Expansion of the Hadley Circulation since 1979. *Atmospheric Chemistry and Physics*, **7**, 5229-5236.

Hudson, R. D., M. F. Andrade, M. B. Follette, and A. D. Frolov, 2006: The Total Ozone Field Separated into Meteorological Regimes; Part II: Northern Hemisphere Mid-latitude Total Ozone Trends. *Atmospheric Chemistry and Physics*, **6**, 5183-5191.

Karamperidou, C., P. N. Di Nezio, A. Timmermann, F. F. Jin, and K. M. Cobb, 2015: The Response of ENSO Flavors to Mid-Holocene Climate: Implications for Proxy Interpretation. *Paleoceanography*, **30**, 527-547.

Khairoutdinov, M., and K. Emanuel, 2013: Rotating Radiative-convective Equilibrium Simulated by a Cloud-resolving Model. *Journal of Advances in Modeling Earth Systems*, **5**, 816-825.

Kitoh, A., 2004: Effects of Mountain Uplift on East Asian Summer Climate Investigated by a Coupled Atmosphere–Ocean GCM. *Journal of Climate*, **17**, 783-802.

Klotzbach, P. J., and C. W. Landsea, 2015: Extremely Intense Hurricanes: Revisiting Webster et al.(2005) After 10 Years. *Journal of Climate*, **28**, 7621-7629.

Knapp, K. R., M. C. Kruk, D. H. Levinson, H. J. Diamond, and C. J. Neumann, 2010: The International Best Track Archive for Climate Stewardship (IBTrACS). *Bulletin of the American Meteorological Society*, **91**, 363.

Knutson, T. R., J. J. Sirutis, M. Zhao, R. E. Tuleya, M. Bender, G. A. Vecchi, G. Villarini, and D. Chavas, 2015: Global Projections of Intense Tropical Cyclone Activity for the Late Twenty-first Century from Dynamical Downscaling of CMIP5/RCP4. 5 Scenarios. *Journal of Climate*, **28**, 7203-7224.

Knutson, T. R., J. L. McBride, J. Chan, K. Emanuel, G. Holland, C. Landsea, I. Held, J. P. Kossin, A. Srivastava, and M. Sugi, 2010: Tropical Cyclones and Climate Change. *Nature Geoscience*, **3**, 157-163.

Knutson, T. R., J. J. Sirutis, G. A. Vecchi, S. Garner, M. Zhao, H.-S. Kim, M. Bender, R. E. Tuleya, I. M. Held, and G. Villarini, 2013: Dynamical Downscaling Projections of Twenty-first-century Atlantic Hurricane Activity: CMIP3 and CMIP5 Model-based Scenarios. *Journal of Climate*, **26**, 6591-6617.

Koh, J., and C. Brierley, 2015: Tropical Cyclone Genesis Potential across Palaeoclimates. *Climate of the Past*, **11**, 1433.

Korty, R. L., and K. A. Emanuel, 2007: The Dynamic Response of the Winter Stratosphere to an Equable Climate Surface Temperature Gradient. *Journal of Climate*, **20**, 5213-5228.

Korty, R. L., S. J. Camargo, and J. Galewsky, 2012: Tropical Cyclone Genesis Factors in Simulations of the Last Glacial Maximum. *Journal of Climate*, **25**, 4348-4365.

——, 2012: Variations in Tropical Cyclone Genesis Factors in Simulations of the Holocene Epoch. *Journal of Climate*, **25**, 8196-8211.

Korty, R. L., K. A. Emanuel, M. Huber, and R. A. Zamora, 2016: Tropical Cyclones Downscaled from Simulations with Very High Carbon Dioxide Levels. *Journal of Climate*, doi:10.1175/JCLI-D-16-0256.

Kossin, J. P., T. L. Olander, and K. R. Knapp, 2013: Trend Analysis with a New Global Record of Tropical Cyclone Intensity. *Journal of Climate*, **26**, 9960-9976.

Kossin, J. P., K. A. Emanuel, and G. A. Vecchi, 2014: The Poleward Migration of the Location of Tropical Cyclone Maximum Intensity. *Nature*, **509**, 349-352.

Kossin, J. P., K. A. Emanuel, and S. J. Camargo, 2016: Past and Projected Changes in Western North Pacific Tropical Cyclone Exposure. *Journal of Climate*, **29**, 5725-5739.

Kurihara, K., K. Ishihara, H. Sasaki, Y. Fukuyama, H. Saitou, I. Takayabu, K. Murazaki, Y. Sato, S. Yukimoto, and A. Noda, 2005: Projection of Climatic Change over Japan Due to Global Warming by High-resolution Regional Climate Model in MRI. *Scientific Online Letters on the Atmosphere*, **1**, 97-100.

Landsea, C. W., B. A. Harper, K. Hoarau, and J. A. Knaff, 2006: Can We Detect Trends in Extreme Tropical Cyclones? *Science*, **313**, 452-454.

Landsea, C. W., G. A. Vecchi, L. Bengtsson, and T. R. Knutson, 2010: Impact of Duration Thresholds on Atlantic Tropical Cyclone Counts. *Journal of Climate*, **23**, 2508-2519.

Lau, N.-C., and M. J. Nath, 1991: Variability of the Baroclinic and Barotropic Transient Eddy Forcing Associated with Monthly Changes in the Midlatitude Storm Tracks. *Journal of Atmospheric Sciences*, **48**, 2589-2613.

Lighty, R. G., I. G. Macintyre, and R. Stuckenrath, 1982: Acropora Palmata Reef Framework: A Reliable Indicator of Sea Level in the Western Atlantic for the Past 10,000 Years. *Coral Reefs*, **1**, 125-130.

Liu, K.-b., and M. L. Fearn, 1993: Lake-sediment Record of Late Holocene Hurricane Activities from Coastal Alabama. *Geology*, **21**, 793-796.

——, 1998: Landfall Probabilities of Prehistoric Catastrophic Hurricanes Estimated from Gulf Coast Lake-Sediment Records. *The Association of American Geographers 94th Annual Meeting*.

Manabe, S., J. L. Holloway Jr, and H. M. Stone, 1970: Tropical Circulation in a Time-Integration of a Global Model of the Atmosphere. *Journal of Atmospheric Sciences*, **27**, 580-613.

Mantsis, D. F., B. R. Lintner, A. J. Broccoli, and M. Khodri, 2013: Mechanisms of Mid-Holocene Precipitation Change in the South Pacific Convergence Zone. *Journal of Climate*, **26**, 6937-6953.

Marchok, T. P., 2002: How the NCEP Tropical Cyclone Tracker Works. *Preprints, 25th Conf. on Hurricanes and Tropical Meteorology, San Diego, CA, Amer. Meteor. Soc. P*.

Martin, G., N. Bellouin, W. J. Collins, I. D Culverwell, P. R. Halloran, S. C. Hardiman, T. J. Hinton, C. D. Jones, R. E. McDonald, and A. J. McLaren, 2011: The HadGEM2

Family of Met Office Unified Model Climate Configurations, *Geoscientific Model Development*, **4**, 723–757.

Mbengue, C., and T. Schneider, 2013: Storm Track Shifts under Climate Change: What Can Be Learned from Large-Scale Dry Dynamics, *Journal of Climate*, **26**, 9923-9930.

Murakami, H., G. A. Vecchi, S. Underwood, T. L. Delworth, A. T. Wittenberg, W. G. Anderson, J.-H. Chen, R. G. Gudgel, L. M. Harris, and S.-J. Lin, 2015: Simulation and Prediction of Category 4 and 5 Hurricanes in the High-Resolution GFDL HiFLOR Coupled Climate Model. *Journal of Climate*, **28**, 9058-9079.

Nolan, D. S., and E. D. Rappin, 2008: Increased Sensitivity of Tropical Cyclogenesis to Wind Shear in Higher SST Environments. *Geophysical Research Letters*, **35**, L14805.

Nolan, D. S., E. D. Rappin, and K. A. Emanuel, 2007: Tropical Cyclogenesis Sensitivity to Environmental Parameters in Radiative–convective Equilibrium. *Quarterly Journal of the Royal Meteorological Society*, **133**, 2085-2107.

O'Gorman, P. A., and T. Schneider, 2008: Energy of Midlatitude Transient Eddies in Idealized Simulations of Changed Climates. *Journal of Climate*, **21**, 5797-5806.

Palmén, E. H., 1948: On the Formation and Structure of Tropical Cyclones. *Geophysica*, **3**, 26-38.

Ramsay, H. A., and A. H. Sobel, 2011: Effects of Relative and Absolute Sea Surface Temperature on Tropical Cyclone Potential Intensity Using a Single-column Model. *Journal of Climate*, **24**, 183-193.

Rappin, E. D., D. S. Nolan, and K. A. Emanuel, 2010: Thermodynamic Control of Tropical Cyclogenesis in Environments of Radiative-convective Equilibrium with Shear. *Quarterly Journal of the Royal Meteorological Society*, **136**, 1954-1971.

Rotunno, R., and K. A. Emanuel, 1987: An Air-sea Interaction Theory for Tropical Cyclones. Part II: Evolutionary Study Using a Nonhydrostatic Axisymmetric Numerical Model. *Journal of Atmospheric Sciences*, **44**, 542-561.

Schreck III, C. J., K. R. Knapp, and J. P. Kossin, 2014: The Impact of Best Track Discrepancies on Global Tropical Cyclone Climatologies Using IBTrACS. *Monthly Weather Review*, **142**, 3881-3899.

Seidel, D. J., and W. J. Randel, 2007: Recent Widening of the Tropical Belt: Evidence from Tropopause Observations. *Journal of Geophysical Research: Atmospheres*, **112**, D20113.

Seidel, D. J., Q. Fu, W. J. Randel, and T. J. Reichler, 2008: Widening of the Tropical Belt in a Changing Climate. *Nature Geoscience*, **1**, 21-24.

Shaevitz, D. A., S. J. Camargo, A. H. Sobel, J. A. Jonas, D. Kim, A. Kumar, T. E. LaRow, Y.-K. Lim, H. Murakami, and K. A. Reed, 2014: Characteristics of Tropical Cyclones in High-resolution Models in the Present Climate. *Journal of Advances in Modeling Earth Systems*, **6**, 1154-1172.

Sherwood, S. C., and M. Huber, 2010: An Adaptability Limit to Climate Change Due to Heat Stress. *Proceedings of the National Academy of Sciences*, **107**, 9552-9555.

Simpson, I. R., T. A. Shaw, and R. Seager, 2014: A Diagnosis of the Seasonally and Longitudinally Varying Midlatitude Circulation Response to Global Warming. *Journal of Atmospheric Sciences*, **71**, 2489-2515.

Sobel, A. H., S. J. Camargo, T. M. Hall, C.-Y. Lee, M. K. Tippett, and A. A. Wing, 2016: Human Influence on Tropical Cyclone Intensity. *Science,* **353**, 242-246.

Stevens, B., M. Giorgetta, M. Esch, T. Mauritsen, T. Crueger, S. Rast, M. Salzmann, H. Schmidt, J. Bader, and K. Block, 2013: Atmospheric Component of the MPI-M Earth System Model: ECHAM6. *Journal of Advances in Modeling Earth Systems,* **5**, 146-172.

Swanson, K. L., 2008: Nonlocality of Atlantic Tropical Cyclone Intensities. *Geochemistry, Geophysics, Geosystems,* **9**, XXXXXX, doi:10.1029/2007GC001844.

Tang, B., and K. Emanuel, 2010: Entropy Ventilation in an Axisymmetric Tropical Cyclone Model. *29th Conference on Hurricanes and Tropical Meteorology*.

Tang, B., and K. Emanuel, 2012: Sensitivity of Tropical Cyclone Intensity to Ventilation in an Axisymmetric Model. *Journal of Atmospheric Sciences,* **69**, 2394-2413.

——, 2012: A Ventilation Index for Tropical Cyclones. *Bulletin of the American Meteorological Society*, **93**, 1901-1912.

Tang, B., and S. J. Camargo, 2014: Environmental Control of Tropical Cyclones in CMIP5: A Ventilation Perspective. *Journal of Advances in Modeling Earth Systems*, **6**, 115-128.

Taylor, K. E., R. J. Stouffer, and G. A. Meehl, 2012: An Overview of CMIP5 and the Experiment Design. *Bulletin of the American Meteorological Society*, **93**, 485-498.

Ting, M., S. J. Camargo, C. Li, and Y. Kushnir, 2015: Natural and Forced North Atlantic Hurricane Potential Intensity Change in CMIP5 Models. *Journal of Climate*, **28**, 3926-3942.

Tippett, M. K., S. J. Camargo, and A. H. Sobel, 2011: A Poisson Regression Index for Tropical Cyclone Genesis and the Role of Large-scale Vorticity in Genesis. *Journal of Climate*, **24**, 2335-2357.

Toomey, M. R., J. P. Donnelly, and J. E. Tierney, 2016: South Pacific Hydrologic and Cyclone Variability during the Last 3000 Years. *Paleoceanography*, **31**, 491-504.

Toomey, M. R., W. B. Curry, J. P. Donnelly, and P. J. Hengstum, 2013: Reconstructing 7000 years of North Atlantic Hurricane Variability Using Deep-sea Sediment Cores from the Western Great Bahama Bank. *Paleoceanography*, **28**, 31-41.

Tory, K., S. Chand, R. Dare, and J. McBride, 2013: An Assessment of a Model-, Grid-, and Basin-independent Tropical Cyclone Detection Scheme in Selected CMIP3 Global Climate Models. *Journal of Climate*, **26**, 5508-5522.

Vecchi, G. A., and B. J. Soden, 2007: Global Warming and the Weakening of the Tropical Circulation. *Journal of Climate*, **20**, 4316-4340.

Vecchi, G. A., A. Clement, and B. J. Soden, 2008: Examining the Tropical Pacific's Response to Global Warming. *Eos, Transactions American Geophysical Union*, **89**, 81-83.

Vitart, F., and T. N. Stockdale, 2001: Seasonal Forecasting of Tropical Storms Using Coupled GCM Integrations. *Monthly Weather Review*, **129**, 2521-2537.

Vitart, F., J. Anderson, and W. Stern, 1997: Simulation of Interannual Variability of Tropical Storm Frequency in an Ensemble of GCM Integrations. *Journal of Climate*, **10**, 745-760.

Walsh, K., M. Fiorino, C. Landsea, and K. McInnes, 2007: Objectively Determined Resolution-dependent Threshold Criteria for the Detection of Tropical Cyclones in Climate Models and Reanalyses. *Journal of Climate*, **20**, 2307-2314.

Walsh, K. J., J. L. McBride, P. J. Klotzbach, S. Balachandran, S. J. Camargo, G. Holland, T. R. Knutson, J. P. Kossin, T.-C. Lee, and A. Sobel, 2016: Tropical Cyclones and Climate Change. *Wiley Interdisciplinary Reviews: Climate Change*, **7**, 65-89.

Walsh, K. J. E., S. J. Camargo, G. A. Vecchi, A. S. Daloz, J. Elsner, K. Emanuel, M. Horn, Y.-K. Lim, M. Roberts, C. Patricola, E. Scoccimarro, A. H. Sobel, S. Strazzo, G. Villarini, M. Wehner, M. Zhao, J. P. Kossin, T. LaRow, K. Oouchi, S. Schubert, H. Wang, J. Bacmeister, P. Chang, F. Chauvin, C. Jablonowski, A. Kumar, H. Murakami, T. Ose, K. A. Reed, R. Saravanan, Y. Yamada, C. M. Zarzycki, P. L. Vidale, J. A. Jonas, and N. Henderson, 2015: Hurricanes and Climate: The U.S. CLIVAR Working Group on Hurricanes. *Bulletin of the American Meteorological Society*, **96**, 997-1017.

Waters, J. J., J. L. Evans, and C. E. Forest, 2012: Large-scale Diagnostics of Tropical Cyclogenesis Potential Using Environment Variability Metrics and Logistic Regression Models. *Journal of Climate*, **25**, 6092-6107.

Webster, P. J., G. J. Holland, J. A. Curry, and H.-R. Chang, 2005: Changes in Tropical Cyclone Number, Duration, and Intensity in a Warming Environment. *Science*, **309**, 1844-1846.

Williams, I. N., R. T. Pierrehumbert, and M. Huber, 2009: Global Warming, Convective Threshold and False Thermostats. *Geophysical Research Letters*, **36**, L21805.

Wing, A. A., K. Emanuel, and S. Solomon, 2015: On the Factors Affecting Trends and Variability in Tropical Cyclone Potential Intensity. *Geophysical Research Letters*, **42**, 8669-8677.

Woodruff, J. D., J. P. Donnelly, K. Emanuel, and P. Lane, 2008: Assessing Sedimentary Records of Paleohurricane Activity Using Modeled Hurricane Climatology. *Geochemistry, Geophysics, Geosystems*, **9**, Q09V10, doi:10.1029/2008GC002043.

Xu, K.-m., and K. A. Emanuel, 1989: Is the Tropical Atmosphere Conditionally Unstable? *Monthly Weather Review*, **117**, 1471-1479.

Yan, Q., T. Wei, R. Korty, J. Kossin, Z. Zhang, and H. Wang, 2016: Enhanced Intensity of Global Tropical Cyclones during the Mid-Pliocene Warm Period. *Proceedings of the National Academy of Science,* **in press**.

Yoo, J., J. Galewsky, S. J. Camargo, R. Korty, and R. Zamora, 2016: Dynamical Downscaling of Tropical Cyclones from CCSM4 Simulations of the Last Glacial Maximum. *Journal of Advances in Modeling Earth Systems*, **8**, doi:10.1002/2016MS000685.

Yukimoto, S., A. Noda, A. Kitoh, M. Hosaka, H. Yoshimura, T. Uchiyama, K. Shibata, O. Arakawa, and S. Kusunoki, 2006: Present-day Climate and Climate Sensitivity in the Meteorological Research Institute Coupled GCM Version 2.3 (MRI-CGCM2. 3). *気象集誌. 第 2 輯*, **84**, 333-363.

Yukimoto, S., A. Yukimasa, M. Hosaka, T. Sakami, H. Yoshimura, M. Hirabara, T. Y. Tanaka, E. Shindo, H. Tsujino, and M. Deushi, 2012: A New Global Climate Model of the Meteorological Research Institute: MRI-CGCM3—Model Description and Basic Performance—. *気象集誌. 第 2 輯*, **90**, 23-64.

Zamora, R. A., R. L. Korty, and M. Huber, 2016: Thermal Stratification in Simulations of Warm Climates: A Climatology Using Saturation Potential Vorticity. *Journal of Climate*, **29**, 5083-5102.